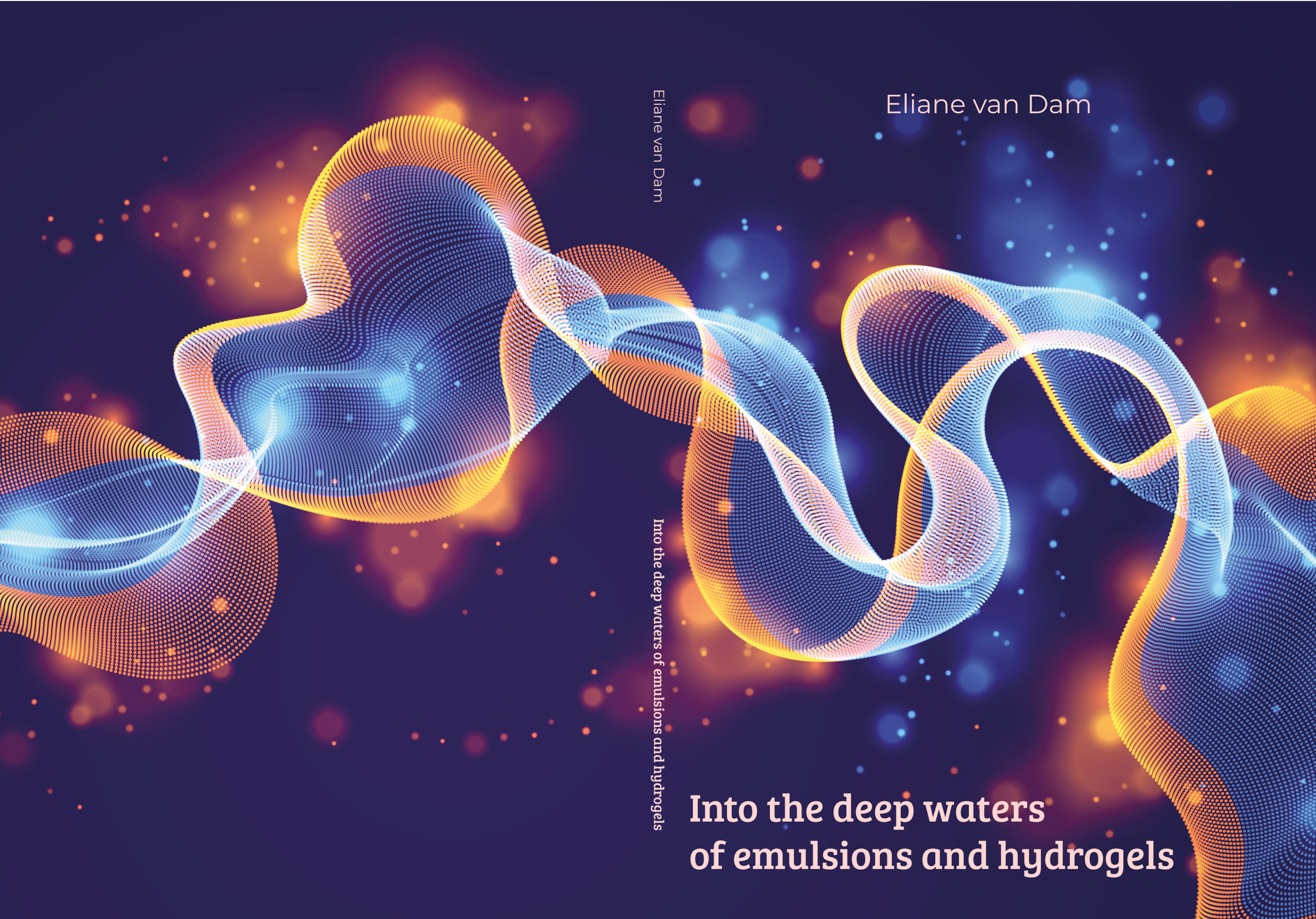

Eliane van Dam

Into the deep waters of emulsions and hydrogels

Eliane van Dam

Into the deep waters of emulsions and hydrogels

Into the deep waters of emulsions and hydrogels

ISBN 978-94-92323-42-2

Cover design: iStock.com/Sylverarts
Cover layout: E.P. van Dam
Print: Ridderprint | www.ridderprint.nl

Into the deep waters of emulsions and hydrogels

ACADEMISCH PROEFSCHRIFT

ter verkrijging van de graad van doctor
aan de Universiteit van Amsterdam
op gezag van de Rector Magnificus
prof. dr. ir. K. I. J. Maex
ten overstaan van een door het College voor Promoties
ingestelde commissie,
in het openbaar te verdedigen in de Agnietenkapel
op vrijdag 13 november 2020, te 16:00 uur

door

Eliane Petra van Dam

geboren te Gouda

Promotiecommissie

promotor:	prof. dr. H. J. Bakker	Universiteit van Amsterdam
overige leden:	prof. dr. W. J. Buma	Universiteit van Amsterdam
	prof. dr. M. Havenith	Ruhr Universität Bochum
	dr. P. H. J. Kouwer	Radboud universiteit
	prof. dr. J. Oomens	Radboud universiteit
	dr. ir. A. Petrignani	Universiteit van Amsterdam
	prof. dr. ir. P. J. Schoenmakers	Universiteit van Amsterdam
	prof. dr. K. P. Velikov	Universiteit van Amsterdam

Faculteit der Natuurwetenschappen, Wiskunde en Informatica

This work is part of the Industrial Partnership Programme Hybrid Soft Materials that is carried out under an agreement between Unilever Research and Development B.V. and the Dutch Research Council (NWO).
The work described in this thesis was performed at AMOLF, Science Park 104, 1098 XG Amsterdam, The Netherlands. This work is part of the Dutch Research Council (NWO).

Publications covered in this thesis

H. Yuan, J. Xu, E. P. van Dam, G. Giubertoni, Y. L. A. Rezus, R. Hammink, H. J. Bakker Y. Zhan, A. Rowen, C. Xing and P. Kouwer. Strategies to Increase the Thermal Stability of Truly Biomi-metic Hydrogels: Combining Hydrophobicity and Directed Hydrogen Bonding. *Macromolecules. 50(22)*, 9058-9065, 2017.
- *chapter 7*

E. P. van Dam and H. J. Bakker. Structure of micelles and micro-emulsions probed through the molecular reorientation of water. *Chem. Phys. 512*, 111-115, 2018.
- *chapter 4*

E. P. van Dam, G. Giubertoni, F. Burla, G. H. Koenderink and H. J. Bakker. Hyaluronan biopolymers release water upon pH-induced gelation. *Phys. Chem. Chem. Phys. 22*, 8667-8671, 2020.
- *chapter 6*

E. P. van Dam, R. Gouzy, E. Pelan, K. P. Velikov and H. J. Bakker. Water reorientation dynamics in nano-emulsions. *In preparation.*
- *chapter 5*

E. P. van Dam, H. Yuan, P. Kouwer and H. J. Bakker. Stucture and dynamics of a temperature sensitive hydrogel. *In preparation.*
- *chapter 7*

Other publications

E. P. van Dam, K. J. van den Berg, A. N. Proaño Gaibor and M. van Bommel. Analysis of triglyceride degradation products in drying oils and oil paints using LC-ESI-MS. *Int. J. Mass Spectrom. 413*, 33-42 (2017).

W. J. Smit, E. P. van Dam, R. Cota and H. J. Bakker. Caffeine and taurine slow down water molecules. *J. Phys. Commun. 3*, 025010 (2019).

R. Cota, E. P. van Dam, S. Woutersen and H. J. Bakker. Slowing down of the molecular reorientation of water in alkaline solutions. *Submitted.*

Contents

1 Introduction

1.1 The challenge of water

Water, one of the most abundant molecules, is essential to all life on earth. Its omnipresence and - at first glance - simple appearance (colorless, odorless, tasteless) may lead us to believe that we know everything there is to know about water. However, this is far from true.[1,2] Nowadays, theoretical scientists are able to simulate complex reactions and systems,[3–8] nonetheless, predicting the behaviour of water remains a great challenge.[9–11] The main reason why it is so difficult to compute the behaviour of water is because water forms a hydrogen bond network.

A hydrogen bond is an interaction between the lone pair of an electronegative atom, and a hydrogen atom bound to an electronegative atom. This results in an interaction that is weaker than a covalent bond, but stronger than van der Waals interactions. In water, this means that the oxygen atom, which has two lone pairs, is acting as a hydrogen bond acceptor, and the hydrogen is the hydrogen bond donor. Each water molecule can form four hydrogen bonds

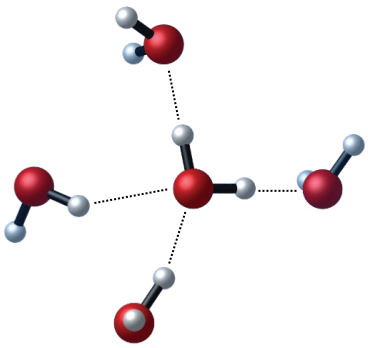

Figure 1.1. Tetrahedral structure of hydrogen bonded water. The hydrogen bonds are depicted as dotted lines.

in total: two donating hydrogen bonds with its two hydrogen atoms, and two accepted hydrogen bonds with its oxygen lone pairs. This leads to a three-dimensional hydrogen bond network (Figure1.1). In its ideal configuration, these four hydrogen bonds have a tetrahedral configuration, as is the case in ice. In liquid water however, the hydrogen bond network is disordered because it is dynamic: water molecules are rotating and constantly breaking and forming new hydrogen bonds on a picosecond timescale.[12–14] This thesis presents an experimental study of the dynamics of water, in of one of the many forms in which water occurs: in nanostructured aqueous systems.

1.2 Nanostructured aqueous systems

There are many aqueous systems which have structures in the nanometer length-scale, in which water plays an important role. These systems range from natural materials, such as lipid bilayers[15,16], hydrogels[17,18] and even cells[2,19], to synthetic materials, including (but not limited to) nanotubes[20–22], metal organic frameworks[23–25], reverse micelles and emulsions[26–29]. A lot of studies on water in nanostructured systems are focused on studying water in confinement, so looking at water molecules that are trapped in nanoconfined spaces. In this work however, we look at systems where water forms the continuous phase of nanostructured systems. We focus on two different aqueous nanostructures. We study water surrounding oil droplets, in the form of oil-in-water emulsions, and we study the role of water in hydrogels.

1.2.1 Emulsions

Emulsions are either oil droplets dispersed in water, or water droplets dispersed in a continuous oil phase. Here, we focus on oil-in-water emulsions. Under normal circumstances, oil and water don not mix, and if one tries to make a mixture of oil droplets in water, these two components will quickly phase separate and form two layers of oil and water. When a surfactant is added to this mixture the oil droplets get stabilized, which makes it possible to have a mixture of oil droplets in water. Surfactants (schematically shown in Figure 1.2) are amphiphilic molecules composed of a hydrophilic headgroup and a hydrophobic tail. When surfactants are dissolved in water, they adsorb at the liquid-water interface, thereby lowering the surface tension. When surfactants are dissolved at a concentration above the critical micelle concentration (cmc), the surfactant molecules aggregate into micelles: spherical structures with a hydrophobic core. Although this core is hydrophobic, it is possible for the surrounding water molecules to penetrate into this core.[30] These micellar structures can be swollen with oil - which will accumulate inside the hydrophobic core of the aggregate. Swelling these micelles with oil (often aided by a short chain alcohol as cosurfactant), leads to the spontaneous formation of micro-emulsions, with droplet sizes from 10-100 nm. Micro-emulsions are thermodynamically stable emulsions, which are formed at very specific compositions involving high surfactant

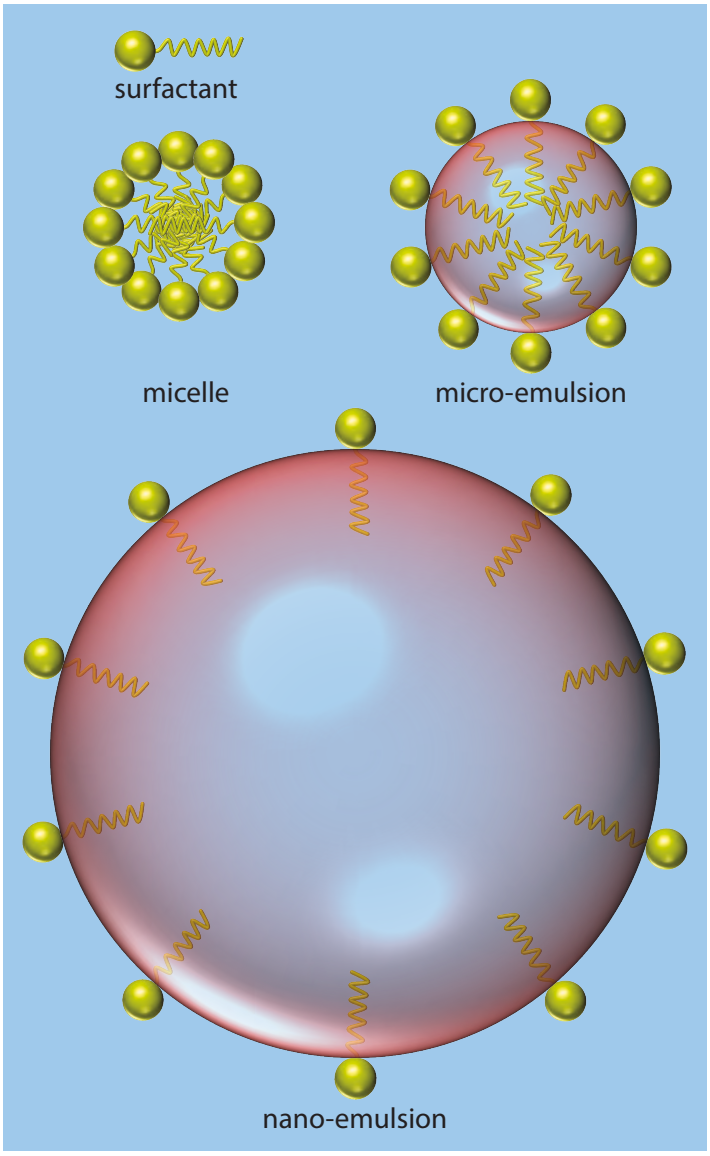

FIGURE 1.2. Overview of studied emulsion systems.

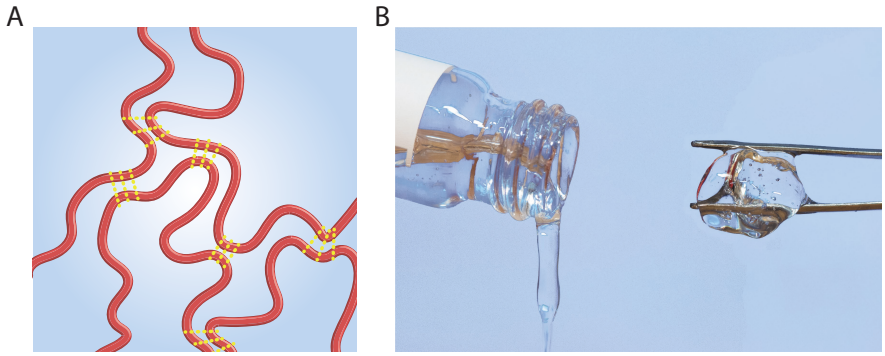

FIGURE 1.3. (A) Schematic representation of a hydrogel with interactions. (B) An example of a responsive hydrogel: hyaluronic acid at pH 1.9 (left) and pH 2.5 (right)

concentrations. Another special class of emulsions are nano-emulsions: these are not thermodynamically stable, but kinetically stable emulsions. They have the benefit that they can be prepared with lower surfactant concentration, and can be prepared with a wide range of compositions. We study the properties of water in micelles, micro-emulsions and nano-emulsions.

1.2.2 HYDROGELS

A hydrogel is a gel, composed of a three-dimensional polymer network, that is capable to hold over 90% of water. The polymer network is created by crosslinks between the polymer molecules (see Figure 1.3A). These crosslinks can either be chemical (in the form of covalent bonds), or physical (through hydrogen bonding, hydrophobic interactions, etc). In this thesis, we study hydrogels that are responsive to their environment, which is only possible for hydrogels with physical crosslinks. The first hydrogel that we study is a biomolecular hydrogel of hyaluronic acid. Hyaluronic acid is a glycosaminoglycan, composed of repeating disaccharide units, consisting of D-glucuronic acid and N-acetyl-D-glucosamine. Hyaluronic acid is found in many biological systems as an important part of the extracellular matrix. The responsive behaviour of hyaluronic acid can take dramatic forms: it forms a gel in a narrow pH range around pH 2.5, denoted as putty state (Figure 1.3B). The second hydrogel that we study is a synthetic, biomimetic hydrogel: polyisocyanotripeptide (TriPIC). These molecules form a β-helical backbone, containing side chains of polyethylene glycol. TriPIC polymer solutions are thermoresponsive and form a gel at temperatures above 50°. For both hydrogels, we investigate the influence of gel formation on the molecular-scale dynamics of the water molecules.

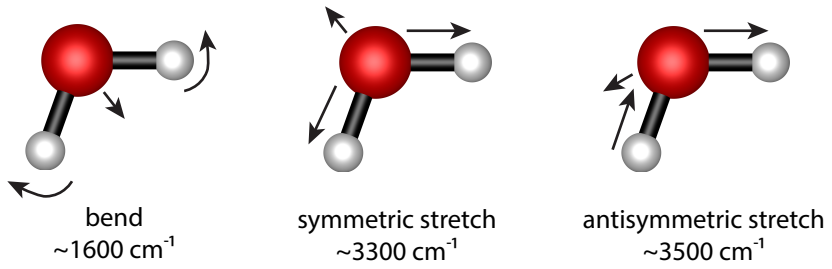

FIGURE 1.4. The vibrational modes of a water molecule.

1.3 SPECTROSCOPY

We study water in these various nanostructured aqueous materials using vibrational infrared spectroscopy. As said, water is a colorless liquid in visible light. However, water is not transparent to infrared light. Water strongly absorbs infrared light that is resonant with the vibrations of the water molecule. The vibrations of the water molecule are depicted in Figure 1.4. The vibrational modes of water, and in particular the stretching modes, are sensitive to the hydrogen bond strength.[12,31,32] This property makes these vibrations good reporters of their environment. For instance, the OH stretch vibration of ice absorbs at a lower frequency than the OH stretch vibration liquid water, because in ice the hydrogen bonds are stronger than in water. The presence of the hydrogen bond makes the covalent bond between the hydrogen and oxygen atom slightly weaker, resulting in a lower resonance frequency. Linear vibrational spectroscopy gives us information about the average hydrogen-bond strength and the width of the distribution of hydrogen-bond strengths. Here we want to study the fluctuations in the hydrogen-bond interactions, in particular in the orientation of the water molecules in different nanostructured materials. To this end, we use polarization-resolved pump-probe infrared spectroscopy. In this technique we employ ultrashort laser pulses to look at ultrafast processes. We obtain information about the vibrational relaxation dynamics and the reorientation dynamics of the water molecules.

1.4 OUTLINE OF THIS THESIS

In chapter 2, we describe how we performed our measurements. To give a good understanding of our polarization-resolved infrared pump-probe experiments, we start by briefly outlining the theory of linear vibrational spectroscopy, followed by a description of nonlinear vibrational pump-probe spectroscopy. We also show how we generate the required infrared pulses with use frequency mixing in nonlinear crystals. In the last part of this chapter, we describe the practical details of the pump-probe setup used throughout this thesis, and we

conclude with a description of the method of data analysis. In chapter 3, we show how we developed a setup that can operate at high repetition rates (from 1 kHz, as is conventional for these measurements, to 16.7 kHz). We discuss the benefit of doing measurements at high repetition rates, the practical implementation of a high repetition rate system, and we show the proof of principle. We also discuss the sample heating that occurs during high repetition rate measurements. In chapters 4 and 5, results on water dynamics surrounding oil-in-water emulsions are shown. Chapter 4 shows our experimental study of the reorientation dynamics of water surrounding micelles and micro-emulsions. We show that for these thermodynamically stable systems, the oil molecules in the inner core of these systems, are completely shielded from the surrounding water. In chapter 5, we present results for a similar system, nano-emulsions, with much bigger droplets. For this system, water molecules do interact with the oil molecules, however, the amount of interaction does not scale with the amount of total surface area. In chapters 6 and 7, we show the behaviour of water in responsive hydrogels. Chapter 6 presents the biological hydrogel hyaluronic acid. High molecular weight hyaluronic acid shows an interesting pH responsive behaviour: in aqueous solution, it forms a gel in a very narrow pH range around pH 2.5. We see that at this pH, less water molecules are immobilized than at pH values at which the solution is a liquid. We observe the same pH dependence of the water dynamics for low-molecular weight hyaluronic acid, which does not form a hydrogel. In chapter 7, we turn to a synthetic, but biocompatible and biomimetic, hydrogel: polyisocyanotripeptides (TriPIC). Aqueous solutions of TriPIC are temperature responsive: at temperatures below 50°C, they are liquid, above that temperature they form a gel. In contrast to hyaluronic acid hydrogels, we see in this case that that more water molecules are immobilized when the system forms a gel.

In conclusion, in this thesis we show that materials with similar macroscopic properties can have very different molecular-scale interactions with water.

2 Experimental methods

The following chapter describes the experimental methods that were used to obtain the results presented in this thesis. We first describe the principles of the experiment, including linear infrared absorption, polarization-resolved infrared pump-probe spectroscopy and infrared light generation. Second, we describe the practical implementation of these methods, including the description of the experimental setup used to obtain the results of this thesis. Lastly, we describe the data analysis procedure used to model the pump-probe data.

2.1 Experimental principles

2.1.1 Vibrational Spectroscopy

In linear vibrational spectroscopy, we irradiate a sample, with thickness L, with infrared light with intensity I_0 (see Figure 2.1). If the frequency of the light is in resonance with an excitation of the sample, light is absorbed resulting in light with intensity I. We measure the transmission T which is defined given by the Lambert-Beer law:

$$T = \frac{I(\omega)}{I_0(\omega)} = e^{-\sigma(\omega)CL} \tag{2.1}$$

The attenuation of the incoming light is dependent on the concentration C of absorbing molecules, the sample thickness L and the absorption cross section $\sigma(\omega)$. The absorption cross section is an excitation (vibration, electronic excitation) specific parameter, and in chemistry the convention is to use the molar

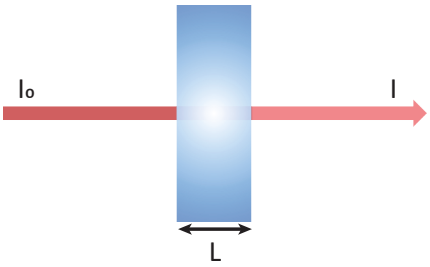

Figure 2.1. Schematic representation of linear spectroscopy: Light with intensity I_0 is attenuated by passing through a sample with thickness L, resulting in light with intensity I.

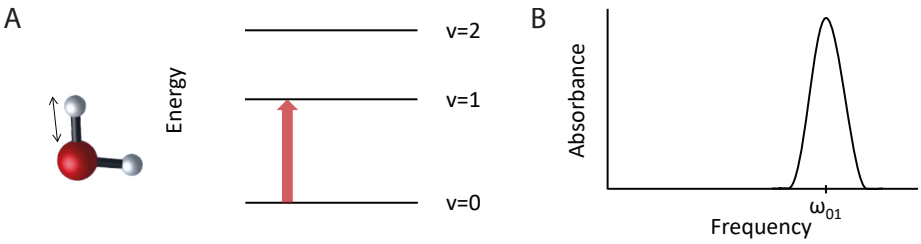

FIGURE 2.2. (A) Schematic representation of vibrational excitation. (B) Spectrum resulting from vibrational excitation.

extinction coefficient ε. The absorption cross section is related to the molar extinction coefficient by

$$\sigma = \ln(10)\frac{10^3}{N_A}\varepsilon \tag{2.2}$$

where N_A is Avogadro's constant. In general, we work with the quantity absorbance $\alpha(\omega)$, which depends linearly on the important parameters

$$\alpha(\omega) = \ln(T) = \sigma(\omega)CL. \tag{2.3}$$

In practice, when we perform a linear vibrational spectroscopy experiment, we measure the absorbance of the sample as a function of frequency, as depicted in Figure 2.2.

MOLECULAR VIBRATIONS A non-linear molecule composed of N atoms has $3N-6$ different vibrations, while a linear molecule has $3N-5$ different vibrations. The water molecule as depicted in Figure 2.2, thus has three different types of vibrations: the symmetric stretch, the antisymmetric stretch and the bending mode. When a molecule absorbs an amount of energy ΔE, related to the frequency of the vibration ω, the vibration is excited:

$$\Delta E = \hbar\omega \tag{2.4}$$

Where $\hbar$ is the reduced Planck constant. We consider a diatomic molecule, which has only one vibrational mode. In a simple model, this vibration can be described classically as a harmonic oscillator.[33] Its motion is described by Newton's second law of motion:

$$F = \mu\frac{d^2x}{dt^2} = -kx \tag{2.5}$$

where μ is the reduced mass of two oscillators with mass m_1 and m_2

$$\mu = \frac{m_1 m_2}{m_1 + m_2}. \tag{2.6}$$

A solution to the differential equation in equation 2.5 is

$$x(t) = A\cos(\omega t) \tag{2.7}$$

where the frequency of the oscillation ω is defined as

$$\omega = \sqrt{k/\mu}. \tag{2.8}$$

The frequency ω thus depends on the reduced mass of the vibration and the spring constant. The total energy of the system is described by the sum of the kinetic energy and the potential energy:

$$E = \frac{p^2}{2\mu} + \frac{1}{2}kx^2, \tag{2.9}$$

where the first term is the kinetic energy, dependent on the momentum p and the reduced mass, and the second term is the potential energy which is quadratic in the vibrational coordinate x in the case of a harmonic oscillator. For molecular vibrations we need to consider the fact that the energy levels are quantized, which we cannot describe with our classical model. To take this quantization into account, we use a quantum mechanical description of system. The system has the following Hamiltonian:

$$\hat{H}_0 = \frac{\hat{p}^2}{2\mu} + \frac{1}{2}k\hat{x}^2 \tag{2.10}$$

with $\hat{p}$ and $\hat{x}$ as the momentum and position operators. It can be seen that the energy is still the sum of the kinetic and the potential energy as in the classical case. The energy levels of the oscillator can be calculated by solving the time-independent Schrödinger equation

$$\hat{H}_0\psi = E\psi \tag{2.11}$$

Leading to the energy of the different levels:

$$E_v = \left(v + \frac{1}{2}\right)\hbar\omega_0 \tag{2.12}$$

where v is the quantum number and ω_0 the resonance frequency. This describes the system without an external perturbation. When irradiating the system with light, as we do in our spectroscopic experiment, we perturb the molecular system. This allows the system to go from one vibrational state to another vibrational state. The Hamiltonian of the perturbed system is[34]

$$\hat{H}(t) = \hat{H}_0 + \hat{V}(t) \tag{2.13}$$

where $\hat{V}(t)$ is a time-dependent perturbation. The transitions between the levels can be described by solving the time-dependent Schrödinger equation[34]

$$\hat{H}(t)\Psi = i\hbar\frac{\partial\Psi}{\partial t}. \tag{2.14}$$

For a small perturbation, the transition rate R_{ab} (for a transition from state $|a\rangle$ to state $|b\rangle$ is given by Fermi's golden rule:

$$R_{ab} = \frac{\pi}{2\hbar^2}|\langle b|\hat{V}(t)|a\rangle|^2(\delta(\omega_{ab} - \omega) + \delta(\omega_{ab} + \omega)) \tag{2.15}$$

The time-dependent perturbation is defined as

$$\hat{V}(t) = -\vec{\hat{\mu}} \cdot \vec{E}(t) = -\vec{\hat{\mu}} \cdot \vec{E}_0 \cos(\omega t) \tag{2.16}$$

where $\vec{\hat{\mu}}$ is the dipole moment operator. Substituting $\hat{V}(t)$ in equation 2.15 with equation 2.16 results in

$$R_{ab} = \frac{\pi}{2\hbar^2}|E_0|^2 \cos^2(\theta)(\delta(\omega_{ab} - \omega) + \delta(\omega_{ab} + \omega))|\langle b|\hat{\mu}|a\rangle|^2, \tag{2.17}$$

Where θ is the angle between the electric field $\vec{E}(t)$ and the transition dipole moment $\langle b|\hat{\mu}|a\rangle$. From this equation, it follows that the rate of transition is highest when the polarization of the light is polarized in the same direction of the dipole moment, since the transition rate is proportional to $\cos^2\theta$. This phenomenon forms the background to polarization-resolved pump-probe spectroscopy, which is explained in the next section. The states $\langle b|$ and $|a\rangle$ represent wavefunctions in all degrees of freedom, including the electronic degrees of freedom. For a vibrational transtion, both $\langle b|$ and $|a\rangle$ represent the same electronic state, usually the electronic ground state. Integrating out all coordinates, except the wavefunctions in the vibrational coordinate x, the dipole operator $\vec{\hat{\mu}}$ can be written as:

$$\vec{\hat{\mu}} = \vec{\mu_0} + \hat{x}\frac{\partial \vec{\mu}}{\partial x}, \tag{2.18}$$

where $\vec{\mu_0}$ is the expectation value of the dipole operator. Substituting equation 2.18 into 2.17 results in

$$R_{ab} = \frac{\pi}{2\hbar^2}|E_0|^2 \cos^2(\theta) \left(\frac{\partial \vec{\mu}}{\partial x}\right)^2 (\delta(\omega_{ab} - \omega) + \delta(\omega_{ab} + \omega))|\langle b|\hat{x}|a\rangle|^2, \tag{2.19}$$

where the states $\langle b|$ and $|a\rangle$ now only represent the vibrational wavefunctions in the vibrational coordinate x. From the term $\left(\frac{\partial \vec{\mu}}{\partial x}\right)^2$ it follows that the vibration can only be excited by the light if the transition dipole changes during the vibration, only in that case the vibration is infrared active. The transition can only take place when the frequency of the interacting light matches the transition frequency because of the delta function $(\delta(\omega_{ab} - \omega) + \delta(\omega_{ab} + \omega))$.

Molecular vibrations are coupled to each other, leading to a nonlinear relation between the displacement and the restoring force. This means that in reality vibrations are anharmonic. The description of the quantum anharmonic oscillator is out of the scope of this short introduction, and can be found elsewhere[33–36]. The most important outcome of the description of the anharmonic oscillator is that the different energy levels are not equidistant.

2.1.2 PUMP-PROBE SPECTROSCOPY

Linear vibrational spectroscopy provides us with information about the properties of molecules in equilibrium. With pump-probe spectroscopy, we can measure the dynamics of vibrational relaxation, by putting the system out of

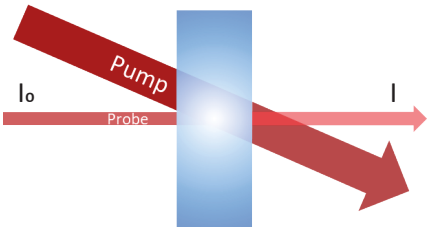

FIGURE 2.3. Schematic representation of pump-probe spectroscopy: Intense laser light is used as a pump to excite molecules in the sample, and the resulting absorption changes are measured using a second, weaker laser pulse, denoted as the probe.

equilibrium. In addition, pump-probe spectroscopy can be used to probe the molecular reorientation. In pump-probe spectroscopy, we first excite our sample with an intense pump pulse, and then we probe the resulting absorption changes with a weaker probe pulse (see Figure 2.3). The measured quantity is $\Delta\alpha$, the difference between the absorbance with and without pump:

$$\Delta\alpha(\omega, t) = \alpha(\omega, t) - \alpha_0(\omega) \tag{2.20}$$

Figure 2.4B shows an example of absorbance spectra without ($\alpha_0(\omega)$) and with ($\alpha(\omega, t)$) pump excitation, and Figure 2.4C shows the resulting difference spectrum. The absorbance spectrum without pump gives us a similar result as the linear infrared experiment discussed in the previous section. However, if we first excite part of the molecules with a pump pulse, the resulting absorbance spectrum looks different: we observe a decrease in absorbance of the original peak at ω_{01}, and a new peak at lower frequency ω_{12}. In the difference spectrum we will thus observe a negative signal at ω_{01}, which we call the bleaching signal, and a positive signal at ω_{12}, an induced absorption. The absorbance without pump pulse is given by equation 2.3

$$\alpha_0(\omega) = \sigma_{01}(\omega)N_0 \tag{2.21}$$

where $N_0 = CL$. With pump excitation, multiple processes take place. The pump pulse excites a part of the molecules from the ground state to the first vibrationally excited state. When we probe the pumped system, there will be less molecules in the ground state, resulting in a smaller absorption. This process is called ground-state depletion. A second process leading to decreased absorption is stimulated emission from the excited state. The molecules that are excited by the pump to the first vibrationally excited state can be further excited to the second vibrationally excited state, leading to an increased absorption at the frequency of the 1 to 2 transition, which is called the excited state absorption. The absorbance in the presence of the pump pulse can thus be described as:

$$\alpha(\omega, t) = \sigma_{01}(\omega)(N_0 - 2N_1(t)) + \sigma_{12}(\omega)N_1(t). \tag{2.22}$$

Combining equations 2.21 and 2.22 leads to

$$\Delta\alpha(\omega, t) = -2\sigma_{01}(\omega)N_1(t) + \sigma_{12}(\omega)N_1(t). \tag{2.23}$$

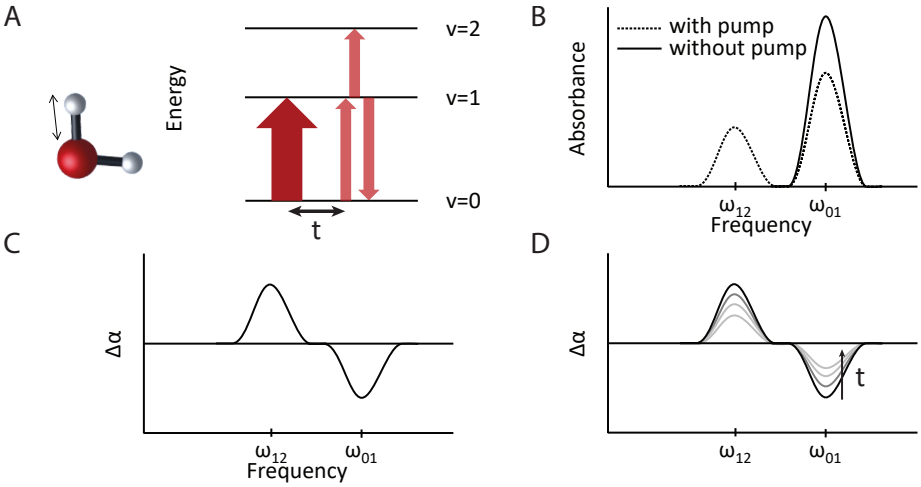

FIGURE 2.4. Pump-probe process. (A) Energy diagram of the pump-probe experiment. (B) Absorbance spectrum with and without pump excitation. (C) Pump-probe differential absorption spectrum at t=0. (D) Pump-probe differential absorption spectrum at different delay times.

The excitation by the pump pulse is short living, and the excited molecules will relax back to the ground state. We can measure the rate of the vibrational relaxation by varying the time delay between pump and probe. As shown in Figure 2.4D, when we measure the difference absorption difference at different delay times, $\Delta\alpha(\omega, t)$ decays with increasing time delay. In the simplest case, where a molecule relaxes exponentially from the excited state to the ground state, the vibrational relaxation takes place according to

$$N_1(t) = N_1(0)e^{-t/T_1} \tag{2.24}$$

where T_1 is the vibrational relaxation time.

POLARIZATION-RESOLVED INFRARED PUMP-PROBE SPECTROSCOPY We showed in equation 2.17 that the excitation of the molecule is most efficient when the transition dipole moment of the molecule is parallel to the polarization direction of the excitating light, following a $cos^2(\theta)$ dependence. In polarization-resolved pump-probe spectroscopy we use this polarization dependence of the excitation efficiency to follow the reorientation of molecules. The principle of the polarization-resolved pump-probe experiment is illustrated in Figure 2.5. Figure 2.5A shows the sample (in this example HDO molecules in water) in equilibrium. The molecules are randomly oriented. Figure 2.5B shows the excitation with the linearly polarized pump pulse and the preferential excitation of the molecules that have their transition dipole moment parallel to the polarization of the light. Subsequently, we measure the induced absorption changes with probing pulses with polarization directions that are parallel and

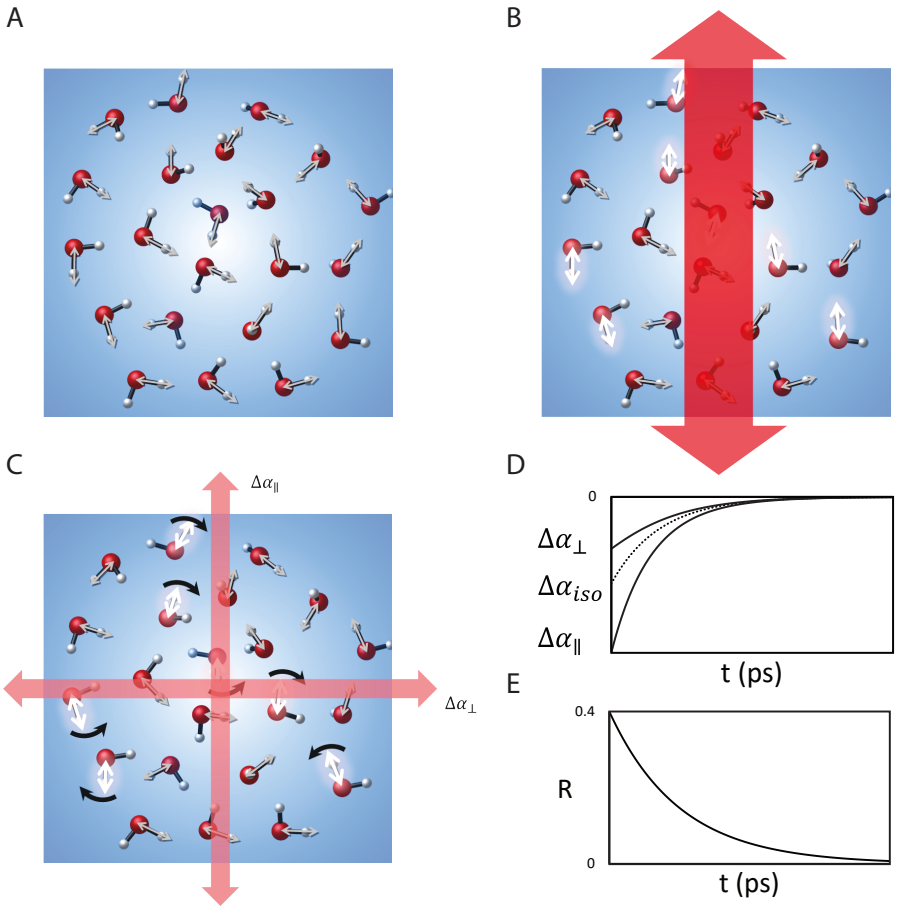

FIGURE 2.5. Illustration of the polarization-resolved infrared pump-probe experiment. The displayed molecules represent HDO molecules. (A) In equilibrium molecules are randomly oriented, their transition dipole moment is depicted with a grey arrow. (B) A linearly polarized pump pulse that is in resonance with the OD stretch vibration, excites the molecules that have their transition dipole moment aligned parallel to the pump polarization direction most efficiently (white arrows). (C) After the pump excitation, the absorption changes are probed with a second laser pulse, polarized either parallel or perpendicular to the pump polarization. (D) the absorption differences $\Delta\alpha_{\parallel}$ and $\Delta\alpha_{\perp}$ as a function of delay time between pump and probe. From these two signals, the isotropic absorption change $\Delta\alpha_{iso}$ is calculated. (E) The anisotropy parameter R as a function of delay time between pump and probe.

perpendicular to the polarization direction of the pump pulse. Directly after the pump excitation, the measured absorption change will be larger for the parallel probe ($\Delta\alpha_{\parallel}(\omega,t)$), than for the perpendicular probe ($\Delta\alpha_{\perp}(\omega,t)$). When the delay time between pump and probe is increased, $\Delta\alpha_{\parallel}(\omega,t)$ and $\Delta\alpha_{\perp}(\omega,t)$ change because of two processes: the signal decreases due to vibrational relaxation, as explained in the previous section, and the difference between the two signals decreases because of molecular reorientation. Using $\Delta\alpha_{\parallel}(\omega,t)$ and $\Delta\alpha_{\perp}(\omega,t)$, we are able to construct the isotropic transient absorption $\Delta\alpha_{iso}$, which is independent of the reorientation of the molecules (Figure 2.5D) [37]

$$\Delta\alpha_{iso} = \frac{1}{3}(\Delta\alpha_{\parallel}(\omega,t) + 2\Delta\alpha_{\perp}(\omega,t)) \tag{2.25}$$

where the factor of 2 for $\Delta\alpha_{\perp}$ results from the fact that in three-dimensional space, there are two directions perpendicular to the pump polarization. We can also construct the anisotropy parameter R, which is independent of the vibrational relaxation (Figure 2.5E) [37,38]. The anisotropy is the difference between the absorption signal in parallel direction and the signal in perpendicular direction, normalized by the isotropic signal:

$$R = \frac{\Delta\alpha_{\parallel}(\omega,t) - \Delta\alpha_{\perp}(\omega,t)}{\Delta\alpha_{\parallel}(\omega,t) + 2\Delta\alpha_{\perp}(\omega,t)}. \tag{2.26}$$

The dynamics of the anisotropy represents the reorientation dynamics of the studied molecule. [39,40] In this thesis, we use the anisotropy to investigate the reorientation of HDO molecules in different environments.

2.1.3 INFRARED PULSE GENERATION

In our pump-probe experiments, we use intense ultrashort infrared light pulses. As such pulses are not directly available from a laser, we make use of optical frequency-conversion processes to create these pulses from a near-infrared laser. At low light intensities, the polarization P induced by light depends linearly on the electric field E:

$$P^{(1)}(t) = \epsilon_0 \chi^{(1)} E(t) \tag{2.27}$$

where ϵ_0 is the vacuum permittivity and the constant $\chi^{(1)}$ is the linear susceptibility. However, in the case of nonlinear light-matter interactions, the induced polarization can be described with a power series of the electric field:

$$\begin{aligned} P(t) &= \epsilon_0(\chi^{(1)}E(t) + \chi^{(2)}E^2(t) + \chi^{(3)}E^3(t) + ...) \\ &= P^{(1)}(t) + P^{(2)}(t) + P^{(3)}(t) + ... \end{aligned} \tag{2.28}$$

where $\chi^{(2)}$ is the second order nonlinear susceptibility, and $\chi^{(3)}$ the third order nonlinear susceptibility. In equations 2.27 and 2.28 we assume the light to be far from resonances of the medium, contrary to the resonant interactions described in the previous section. We consider the interaction of two electric fields, E_1

and E_2, with frequencies ω_1 and ω_2, interacting with a material with non-zero $\chi^{(2)}$. The total electric field can be described as:

$$E(t) = E_1 e^{-i\omega_1 t} + E_2 e^{-i\omega_2 t} + c.c. \tag{2.29}$$

The resulting second-order nonlinear polarization response is:

$$P^{(2)}(t) = \epsilon_0 \chi^{(2)} E^2(t) \tag{2.30}$$

When we substitute the electric field, we obtain the various components of the nonlinear polarization, each representing a specific frequency-conversion process[41]:

$$\begin{aligned} P^{(2)}(t) = \epsilon_0 \chi^{(2)} (& E_1^2 (e^{-i2\omega_1 t} + e^{i2\omega_1 t}) && (SHG) \\ & + E_2^2 (e^{-i2\omega_2 t} + e^{i2\omega_2 t}) && (SHG) \\ & + 2E_1 \cdot E_2 (e^{-i(\omega_1+\omega_2)t} + e^{i(\omega_1+\omega_2)t}) && (SFG) \\ & + 2E_1 \cdot E_2 (e^{-i(\omega_1-\omega_2)t} + e^{i(\omega_1-\omega_2)t}) && (DFG) \\ & + 2(E_1^2 + E_2^2)) && (OR) \end{aligned} \tag{2.31}$$

The nonlinear processes are displayed visually in Figure 2.6. The terms included in the second-order nonlinear response are second harmonic generation (frequency doubling, SHG), sum frequency generation (SFG), difference frequency generation (DFG) and optical rectification (OR).

PHASE MATCHING As shown in equation 2.31, the nonlinear response contains multiple conversion processes. However, usually the nonlinear susceptibility of a material is low. To increase the efficiency of a particular nonlinear process, we need the conversion to be constructive over a long interaction length. The spatial variation of the propagating fields in equation 2.29 is given by $e^{ik_1 x}$ and $e^{ik_2 x}$, where k_i is the wavevector $k_i(\omega) = \frac{n_i(\omega_i)\omega_i}{c}$, where n_i is the refractive index at frequency ω_i and c the speed of light. For the DFG process:

$$\omega_3 = \omega_1 - \omega_2 \tag{2.32}$$

phase matching is achieved when:

$$n_3\omega_3 = n_1\omega_1 - n_2\omega_2 \tag{2.33}$$

To fulfill the phase matching condition, we use a nonlinear birefringent material for frequency mixing. In birefringent materials, the refractive index is dependent on the polarization direction. By choosing the polarizations of the interacting beams and the orientation of the birefringent medium, phase matching can be achieved. We achieve phase matching using angle tuning of the birefringent crystal. For light that is polarized perpendicular to the optical axis of the crystal the refractive index is the ordinary refractive index n_0. Light polarized in the direction of the optical axis, the generated field in the frequency mixing process, experiences the extraordinary refractive index $n_0(\theta)$

$$\frac{1}{n_e^2(\theta)} = \frac{\cos^2\theta}{n_o^2} + \frac{\sin^2\theta}{n_e^2}, \tag{2.34}$$

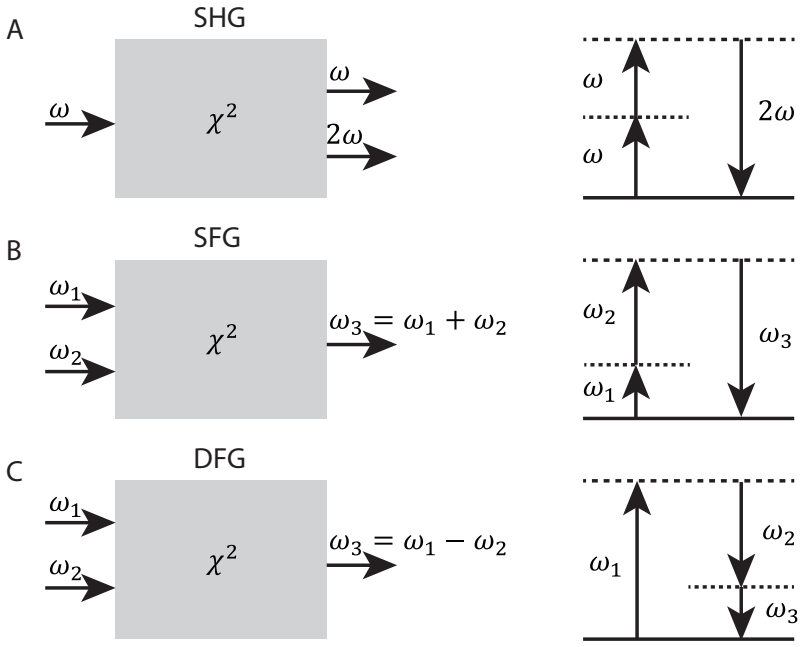

FIGURE 2.6. Second-order frequency conversion processes described by equation 2.31 for (A) second harmonic generation (SHG), (B) sum frequency generation (SFG) and (C) difference frequency generation (DFG). The left side shows the geometry of the interaction, the right side an energy-level description of the interaction.

in which θ is the angle of the incoming beam with respect to the optical axis. The dependence of n_e on the crystal angle allows us to fulfill the phase matching by turning the crystal angle.

OPTICAL PARAMETRIC AMPLIFICATION For the generation of intense infrared laser pulses, we use optical parametric amplification (OPA), which is a frequency conversion process that is highly similar to difference frequency generation. In optical parametric amplification, a weak pulse which we call the seed, with frequency ω_s is amplified by an intense light beam with frequency ω_p. This pump beam amplifies the seed, and a new beam with frequency ω_i is created, under the condition $\omega_i = \omega_p - \omega_s$. The amplified seed is called the signal, and the newly created beam is called the idler.

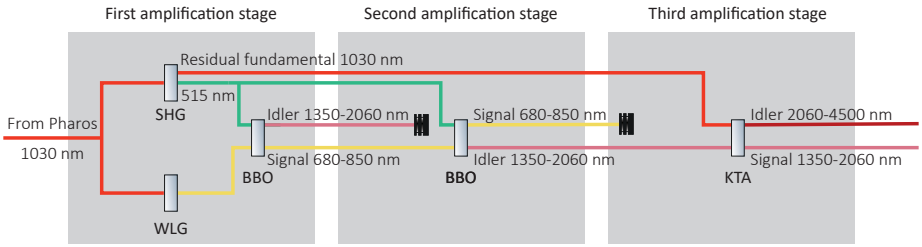

FIGURE 2.7. Schematic overview of generation of mid-infrared pulses. SHG: second harmonic generation. WLG: white light generation. BBO: β-barium borate crystal. KTA: potassium titanyle arsenate crystal.

2.2 PRACTICAL IMPLEMENTATION

2.2.1 PULSE GENERATION

In our experiments, we use pump and probe pulses centered at 2500 cm^{-1}. These pulses are created by frequency conversion of the output of a Yb:KGW (ytterbium doped potassium gadolinium tungstate) based laser system (Pharos, Light Conversion) using a tunable OPA (Orpheus-ONE-HP, Light Conversion). A schematic overview of the pulse generation scheme is depicted in Figure 2.7. The laser produces 400 μJ pulses, with a wavelength of 1030 nm and a pulse duration of ~400 femtoseconds, at a maximum repetition rate of 50 kHz. Using a pulse picker we select the desired repetition rate. Part of the light is used to generate white light in a white light generation medium (WLG), and part of the light is used for second harmonic generation (SHG). In the first frequency conversion step, white light is parametrically amplified in a BBO crystal, being pumped by the second harmonic light (515 nm), resulting in tunable signal (680-850 nm) and idler pulses (1350-2060 nm). In the second frequency conversion step, the signal and idler pulses are amplified in a second BBO crystal, using again second harmonic light (515 nm) as the pump. Subsequently the idler pulses are used as an input seed (please note: now the idler is used as a seed and will become the signal) in a third OPA process in a KTA crystal that is pumped with part of the fundamental output of the pump laser at 1030 nm. This OPA process results in a strong signal pulse (1350-2060 nm) and a new idler (2060-4500 nm) pulse. By using a wavelength separator, we select the idler pulse for our pump-probe experiment. With this method we generated idler pulses at 4000 nm (2500 cm^{-1}) with an energy of 12 μJ, a bandwidth of 100 cm^{-1}, and a pulse duration of 200 fs.

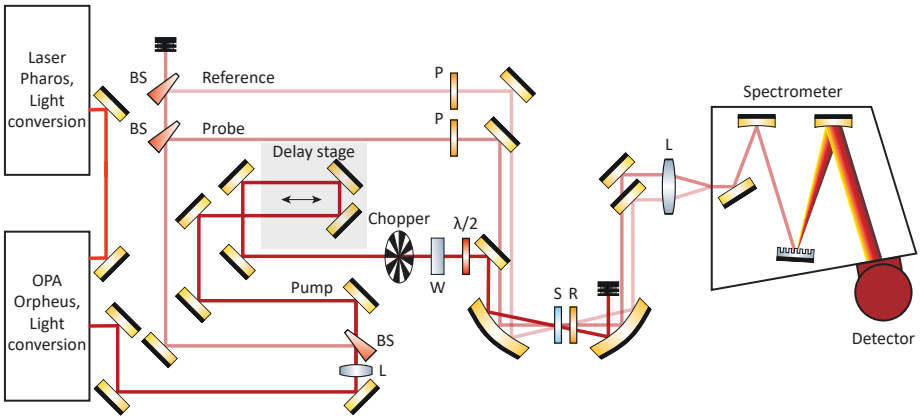

FIGURE 2.8. Pump-probe setup. L: lens. BS: ZnSe wedge beamsplitter. P: Polarizer. W: Wobbler. $\lambda/2$: Half wave plate. S: Sample. R: Rotating polarizer.

2.2.2 ONE-COLOR POLARIZATION-RESOLVED INFRARED PUMP-PROBE SETUP

Figure 2.8 shows the overview of the pump-probe setup. After the generation, the 2500 cm^{-1} pulses are sent through a CaF_2 lens to collimate the beam, before splitting the pulses using a ZnSe wedge beamsplitter. The transmitted beam is the pump pulse, and the reflected beam is split into a probe and reference beam. In the reference path, an extra beamsplitter is placed to enable an independent measurement of the power of the light for calibration purposes. The polarizations of the probe and reference beam are cleaned up using a wire grid polarizer. The pump beam passes over a motorized delay stage, which enables the time delay between pump and probe pulses, and is then passed through a chopper that blocks every other pulse. After the chopper, the beam is guided through a wobbler, which allows us to suppress the effects of interference of scattered pump light with the probe light. A $\lambda/2$ plate was used to rotate the pump polarization 45° with respect to the polarization of the probe and the reference pulse. All three beams, pump probe and reference are then directed on a gold-coated parabolic mirror (90°C f=150 mm), which focuses the beams in the sample. The pump and probe are spatially overlapped in the sample, and the reference has a small spatial offset with respect to these beams. After the sample, the pump beam is blocked and a rotating polarizer selects probe and reference pulses that are either polarized parallel or perpendicular with respect to the pump polarization. The probe and reference beam are subsequently collimated using a second parabolic mirror, and focused into a spectrograph that disperses the beams, after which the two beams are detected with two rows of a 3x32 pixel mercury-cadmium-telluride array detector (MCT, Infrared associates). The details of the detection of the signals and the electronics of the pump-probe setup are presented in chapter 3.

2.2.3 SAMPLES

In the pump-probe measurements presented in this thesis, we pump and probe the OD stretch vibration of HDO molecules in H_2O. We prepare isotopically diluted water by mixing 4% D_2O with 96% H_2O, resulting in an 8% HDO in water mixture. Studying the OD stretch vibration of isotopically diluted water has several advantages compared to studying the OH stretch vibrations in pure water.

- In H_2O, the OH stretch vibrations are strongly mixed which results in symmetric and antisymmetric stretching modes with a small frequency difference. In HDO, the OD and OH stretch modes are isolated vibrations that absorb at quite different frequencies.

- In pure H_2O, the excitation of the OH stretch vibration is delocalized because of intermolecular dipole-dipole coupling. This interaction strongly depends on the distance between the interacting oscillators. By keeping the concentration of OD oscillators low, the effects of dipole-dipole coupling of OD vibrations can be minimized, so that an excited OD stretch vibration stays quite well localized.[42]

- OH and OD stretch vibration absorb strongly. By isotopical dilution, we keep the concentration of the studied oscillators low, allowing us to use a practical sample thickness (10-100 μm). The low concentration of OD stretch vibrations also strongly reduces the heating of the sample following the vibrational relaxation.

- The measurement of the reorientation of the water molecules via the anisotropy of the excitation is only possible over the time that the vibrations remain excited to a certain minimal degree. The OD stretch vibration has a longer vibrational lifetime than the OH stretch vibration, thus allowing us to study reorientation processes over much longer timescales. By using isotopically diluted water, the majority of the sample is still H_2O, so our results are reflecting the molecular dynamics of water.[43–46]

The samples are measured within a circular stainless-steel sample cell. In this sample cell, the sample is applied between two CaF_2 windows (25 mm ⌀, 2 mm thickness, Crystran Ltd), and separated by a Teflon spacer (10 to 100 μm). To perform temperature-dependent measurements, we mounted the sample cell into a temperature-controlled sample holder. A control unit (TE Technology) controls the temperature using a Peltier element and a thermocouple attached to the sample cell for active feedback. In some of the experiments, the temperature-controlled sample holder was mounted on a rotating sample holder, which prevents local heating of the sample.

EMULSIONS In this thesis we describe different types of emulsion systems: micelles (technically not an emulsion), micro-emulsions and nano-emulsions. Micelles and micro-emulsions are thermodynamically stable systems, and form

spontaneously. We prepare micelles by dissolving surfactants into isotopically diluted water. When dissolved at a concentration above the critical micelle concentration (CMC), micelles form spontaneously. Micro-emulsions contain not only surfactants and water but also a hydrophobic liquid (oil). Micro-emulsions can be formed by first dissolving the surfactants in (isotopically diluted) water, followed by the addition of oil to the solution. Most micro-emulsions require a co-surfactant (usually an alcohol) to form, but by carefully choosing the surfactant we were able to prepare micro-emulsions without cosurfactant. Whether oil-in-water or water-in-oil droplets are formed, can be checked by diluting the micro-emulsion with oil or water. The emulsion can easily be diluted with the continuous phase of the emulsion, but will phase separate when diluted with the dispersed phase.

Nano-emulsions are not thermodynamically stable, and are thus prepared in a different way. For the preparation of nano-emulsions, we first prepare a macro-emulsion by mixing surfactant, oil and water. After macroemulsion formation, the solution is processed through an impinging jet mixer. By processing the emulsion at different pressures, different droplet sizes are obtained. For the nano-emulsions, the isotopic dilution is created after nano-emulsion formation, by adding the desired amount of D_2O to the nano-emulsion.

HYDROGELS We study two different hydrogels: hydrogels from hyaluronic acid and hydrogels from polyisocyanotripeptides (TriPIC). Both of these hydrogels are highly responsive to their environment: aqueous hyaluronic acid solutions form a hydrogel around a pH of 2.5, aqueous TriPIC solutions form a hydrogel at temperatures above 50°C. Both hydrogels are prepared by dissolving the polymer in the form of a powder into isotopically diluted water. For hyaluronic acid, the pH was adjusted after dissolving the powder completely. The solutions were stored at 4°C. For TriPIC solutions, the solution was prepared at 4°C. It was possible to recycle the TriPIC solutions by freeze-drying the solutions, and dissolving the remaining powder again. TriPIC solutions were stored at -20°C.

2.3 DATA ANALYSIS

As stated in section 2.1.2, the isotropic transient absorption spectrum, $\Delta\alpha_{iso}$, reflects the vibrational relaxation dynamics of the excited oscillators. In the most simple case, all oscillators are excited to the same state and relax directly back to the ground state, as depicted in Figure 2.4. However, relaxation dynamics are often more complicated than this simple case: relaxation can occur via different intermediate states, multiple vibrational species can be excited, and the excitation energy can be converted into a long living heating signal. For instance, if we look at the isotropic spectrum of 4% D_2O in H_2O in Figure 2.9, we observe that at long time delays, the spectrum does not decay to zero, but shows the spectral signature of a heated ground state.[39] The total observed anisotropy R_{total} is the average of the anisotropies of the individual components

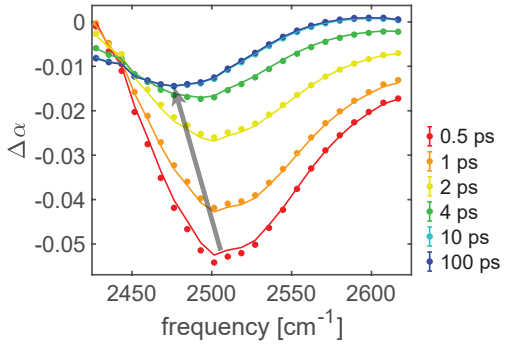

FIGURE 2.9. Isotropic transient absorption change of the OD stretch vibration of HDO molecules in isotopically diluted water, at different delay times. The grey arrow indicates the shift of the spectrum resulting from sample heating.

R_i, weighed by their amplitude $\Delta\alpha_i$:

$$R_{total} = \frac{\sum_i \Delta\alpha_i \cdot R_i}{\sum_i \Delta\alpha_i} \tag{2.35}$$

To distinguish the anisotropy dynamics of the different oscillators, without the influence of other contributions, we perform a kinetic modeling of the transient isotropic spectrum.[47] After this, we are able to fit the anisotropy decay distinguishing the different contributions.

2.3.1 KINETIC MODELLING

The transient absorption spectrum can be decomposed in spectral components. Each component has its own spectral signature σ_i, and a time dependent population $N_i(t)$. The transient absorption is described as:

$$\Delta\alpha_{mdl}(t,\omega) = \sum_i N_i(t) \cdot \sigma_i(\omega) \tag{2.36}$$

For the vibrational relaxation of the OD stretch vibration, we find that this can be best described by a cascade relaxation model, depicted in Figure 2.10. In this model, the excited vibration relaxes from the first vibrationally excited state (1) via an intermediate state (0*) to a heated ground state (0'). The populations of these states, N_1, N_0^* and N_0' can be described by:

$$\frac{d}{dt}\begin{pmatrix} N_1(t) \\ N_0^*(t) \\ N_0'(t) \end{pmatrix} = \begin{pmatrix} -k_1 & 0 & 0 \\ +k_1 & -k^* & 0 \\ 0 & +k^* & 0 \end{pmatrix} \begin{pmatrix} N_1(t) \\ N_0^*(t) \\ N_0'(t) \end{pmatrix} \tag{2.37}$$

Where k_1 is the vibrational relaxation rate of the OD stretch vibration, and k^* the thermalization rate. Solving these differential equations yields the following

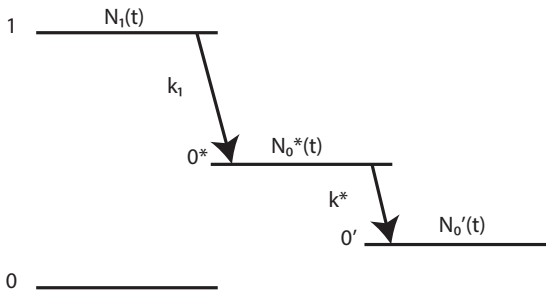

FIGURE 2.10. Kinetic model used to describe a relaxation process with delayed ingrowing heating. The excitation of a population N_1 and spectral signature σ_1 decays from the excited state 1 with a relaxation rate of k_1 to an intermediate state 0^*. Subsequently, the population N_0^* decays to the heated ground state $0'$ with relaxation rate k^*, resulting in a population N_0'.

solutions for the populations:

$$\begin{aligned} N_1(t) &= N_1(0)e^{-k_1 t} \\ N_0^*(t) &= N_1(0)\frac{k_1}{k^* - k_1}(e^{-k_1 t} - e^{-k^* t}) \\ N_0'(t) &= N_1(0)\left(\frac{k_1}{k^* - k_1}e^{-k^* t} - \frac{k^*}{k^* - k_1}e^{-k_1 t}\right) \end{aligned} \tag{2.38}$$

Combining equations 2.36 and 2.38, we obtain the description of the transient signal:

$$\begin{aligned} \Delta\alpha_{mdl}(t,\omega) =& \sigma_1(\omega)N_1(0)e^{-k_1 t} \\ &+ \sigma^*(\omega)N_1(0)\frac{k_1}{k^* - k_1}(e^{-k_1 t} - e^{-k^* t}) \\ &+ \sigma'(\omega)N_1(0)\left(\frac{k_1}{k^* - k_1}e^{-k^* t} - \frac{k^*}{k^* - k_1}e^{-k_1 t}\right) \end{aligned} \tag{2.39}$$

In the case of vibrational relaxation of the OD stretch vibration in isotopically diluted water, the intermediate state has no spectral signature, which implies that the absorption spectrum from this state is the same as from the ground state. In the case of the relaxation of the OD vibration in isotopically diluted water, the intermediate state thus primarily serves to delay the rise of the response of the heated ground state. The spectral signature of the heated ground state, σ', is equal to the transient spectrum at long delay times (t>15 ps).

In our fitting routine, we find the best fit to the model by minimizing the error-weighted square error, which is the difference between the measured transient spectrum $\Delta\alpha(t,\omega)$ and the model $\Delta\alpha_{mdl}(t,\omega)$, divided by the standard

deviation $\varepsilon(t,\omega)$ of the measured spectrum.

$$\chi^2 = \iint \left(\frac{\Delta\alpha(t,\omega) - \Delta\alpha_{mdl}(t,\omega)}{\varepsilon(t,\omega)} \right)^2 dt d\omega \tag{2.40}$$

We minimize χ^2 numerically by varying the relaxation rates k:

$$\chi^2(k) = \iint \left(\frac{\Delta\alpha(t,\omega) - \sum_i N_i(k,t)\cdot\sigma_i(\omega)}{\varepsilon(t,\omega)} \right)^2 dt d\omega \tag{2.41}$$

The best fitting spectra are obtained by finding the minimum of χ^2 with respect to the spectral signatures σ_i at the measured frequency ω_j:

$$\frac{d}{d\forall\sigma_i(\omega_j)} \int \left(\frac{\Delta\alpha(t,\omega_j) - \sum_i N_i(k,t)\cdot\sigma_i(\omega_j)}{\varepsilon(t,\omega_j)} \right)^2 dt = 0 \tag{2.42}$$

Using the calculated spectra, and the guessed k values, χ^2 is calculated. The k values are varied (followed by the calculation of the spectra), until a minimum χ^2 is found.

2.3.2 ANISOTROPY DYNAMICS

The kinetic modeling yields the spectral signatures and time dependent populations of the different spectral components contributing to the transient spectrum. Using these results, the anisotropy dynamics of the excited vibrations can be distinguished, i.e. the total anisotropy can be corrected for the heating contribution to the transient absorption. The transient absorption signal due to sample heating is usually isotropic, meaning that it is equal in the parallel and perpendicular probed signal. If the heating contribution is not subtracted, the anisotropy dynamics do not reflect the reorientation of the excited oscillators. We subtract the heating signal from both the parallel and perpendicular probing signal to obtaining the pure signal of the excited oscillator only:

$$\Delta\alpha_{\parallel,pure}(t,\omega) = \Delta\alpha_{\parallel}(t,\omega) - N_0'(t)\sigma'(\omega) \tag{2.43}$$

$$\Delta\alpha_{\perp,pure}(t,\omega) = \Delta\alpha_{\perp}(t,\omega) - N_0'(t)\sigma'(\omega) \tag{2.44}$$

From these signals, the anisotropy is calculated:

$$R(\omega,t) = \frac{\Delta\alpha_{\parallel,pure}(\omega,t) - \Delta\alpha_{\perp,pure}(\omega,t)}{\Delta\alpha_{\parallel,pure}(\omega,t) + 2\Delta\alpha_{\perp,pure}(\omega,t)} \tag{2.45}$$

The resulting anisotropy dynamics is usually fitted to an exponential function. In the case of neat isotopically diluted water, the anisotropy decay can be described with a single exponential function, where the time constant reflects the reorientation time of the reorientation of the water hydroxyl groups. However, in this thesis, we study the reorientation dynamics of water in nanostructured systems, and we find that in that case the anisotropy decay can best be described with an exponential decay with an offset:

$$R = R_0 e^{-t/\tau_r} + R_{slow} \tag{2.46}$$

Where the time constant τ_r is the reorientation time of neat water, which is attributed to the reorientation of bulk water molecules. The offset R_{slow} is attributed to the water molecules that are strongly slowed down in their reorientation due to their interaction with the solute.

3 Towards pump-probe measurements at high repetition rate

Within the work of this thesis, the experimental pump-probe setup as described in 2.2 was adapted to go from a 1 kHz repetition rate system to a 16.7 kHz repetition rate system. Increasing the repetition rate will allow for more measurements in shorter time, this will lead to an improvement in the signal to noise ratio (SNR), since the number of measurements and the signal to noise are related to each other:

$$SNR \propto \sqrt{n} \tag{3.1}$$

where n is the number of measurements. This chapter explains the practical implementation of pump-probe measurements at high repetition rate.

3.1 Error calculation

To evaluate the improvement in the pump-probe measurements upon increasing the repetition rate, we need to compare the errors of measurements at low and high repetition rate. The following section discusses how the error is defined. In the pump-probe experiments the intensity of the probe spectrum $I_{probe}(\nu)$ is divided by the intensity of the reference spectrum $I_{ref}(\nu)$ to obtain the transmission spectrum $T(\nu)$:

$$T(\nu) = \frac{I_{probe}(\nu)}{I_{ref}(\nu)} \tag{3.2}$$

In the pump-probe measurement, we measure the change in absorption upon pump excitation. The absorption change $\Delta\alpha(\nu)$ is related to the relative change in transmission:

$$\Delta\alpha(\nu) = -ln\left(\frac{T(\nu)}{T_0(\nu)}\right) \tag{3.3}$$

Where $T(\nu)$ is the pumped transmission spectrum and $T_0(\nu)$ is the unpumped transmission spectrum. $T(\nu)$ and $T_0(\nu)$ are measured on a shot-to-shot basis. After measuring i shots (with pump), we determine T by performing a linear least squares fit, which results in:

$$T(\nu) = \frac{\sum_i I_{probe,i}(\nu) I_{ref,i}(\nu)}{\sum_i I_{ref,i}(\nu)^2} \tag{3.4}$$

Where the standard deviation $\sigma_{I_{probe}}$ is:

$$\sigma_{I_{probe}} = \sqrt{\frac{\sum_i (I_{probe,i} - TI_{ref,i})^2}{N-1}} \tag{3.5}$$

And the standard deviation of the transmission is:

$$\sigma_T = \frac{\sigma_{I_{probe}}}{\sqrt{\sum_i I_{ref,i}^2}} \tag{3.6}$$

In the pump-probe experiment we are interested in the standard deviation of T/T_0, which we find by propagating the standard deviation of T and T_0:

$$\sigma_{T/T_0} = \sqrt{\left(\frac{\sigma_T}{T_0}\right)^2 + \left(\frac{\sigma_{T_0} T}{T_0^2}\right)^2} \tag{3.7}$$

In the following sections, we will use σ_T as a measure for the quality of the experiment, and study the effect of different measurement settings on this parameter.

3.2 OPTIMIZATION OF TRIGGERING TIMING

To perform pump-probe infrared measurements at high repetition rate, some practical issues have to be considered. First of all, one needs a laser that operates at high repetition rates. In our case, we use a Pharos system from Light Conversion, which produces pulses with a repetition rate of 50 kHz. Using a built-in pulse picker, we divide the number of pulses by an integer. In the current setup, we can measure up to 16.7 kHz by setting the pulse picker to divide the 50 kHz with 3. Secondly, one must be able to detect the infrared pulses with the same repetition rate, as we wish to measure the signals on a shot-to-shot basis to obtain an optimal correction for fluctuations in the probe pulse intensity and spectrum. The infrared pulses are detected with a mercury cadmium telluride (MCT) detector. The signal is then amplified and integrated by a boxcar amplifier. The analog signal from the boxcar amplifiers is converted to a digital signal by the ADC-cards. These ADC-cards must be able to convert the signal fast and frequent enough to work at high repetition rates.

For the electronics to work optimal, the triggering of the complete pump-probe setup is vital. Figure 3.1 shows the electronic triggering scheme. The master trigger pulse from the laser is delayed with time t_{gate} and broadened with time $t_{gatewidth}$ using pulse generators. This trigger signal controls the time that the gate of the boxcar amplifiers is open. Another trigger is delayed with time t_{ADC} and starts the readout of the boxcar amplifiers by the ADC-cards. This readout should start after the integration by the boxcar amplifiers, thus $t_{ADC} = t_{gate} + t_{gatewidth}$. The boxcar amplifiers are reset using a reset trigger signal that is given at time t_{reset}. The reset signal should be given after the ADC-cards finished the readout of the boxcar amplifiers, and before the

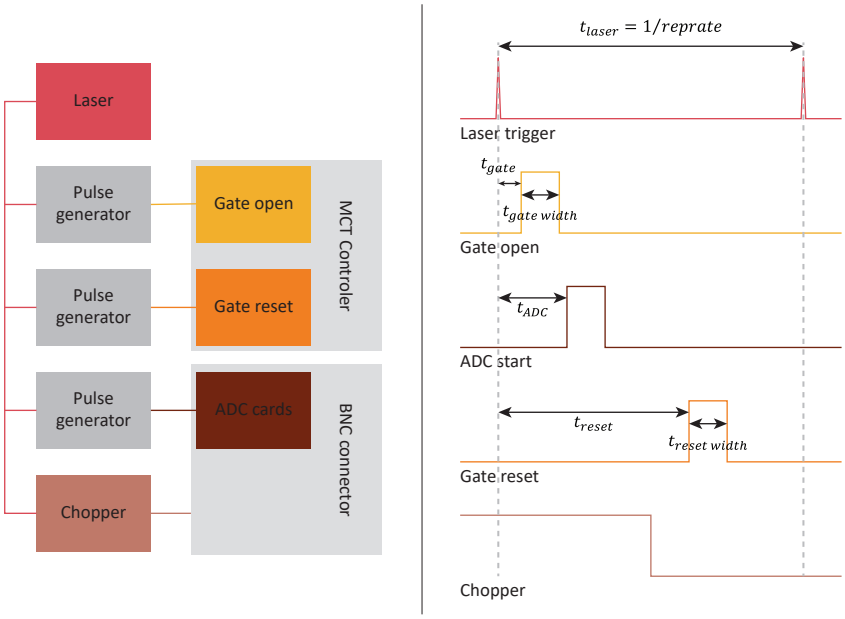

Figure 3.1. Left: schematic representation of the electronic setup for our pump-probe experiment. Right: Timing of the triggering signals.

next master trigger pulse. To be able to increase the repetition rate, the reset pulse should be timed as far as possible before the next master trigger pulse. The maximum repetition rate of the set-up is limited by $1/(t_{reset} + t_{resetwidth})$.

Of all these trigger timings, σ_T and the intensity on the detector are influenced most by the settings of t_{gate} and $t_{gatewidth}$. Figure 3.2 shows the intensity and σ_T as a function of the gate width and gate start position. As shown in Figure 3.2C and D, We observe that the intensity on the detector increases with increasing $t_{gatewidth}$, until a maximum at 1.5 μs, and decreases after that. However, when the width is increased too much, this also yields more noise, resulting in a higher σ_T. The optimal setting for $t_{gatewidth}$ was found to be 1 μs. Figure 3.2A and B show the effect of changing the starting time of the gate t_{gate} (where 0 is the time of the master trigger from the laser, and the time refers to the start of the rising edge of the trigger pulse). We find that the intensity is highest with a start time -100 ns, however, σ_T is lowest when the start time is chosen shortly after the master trigger, at 200 ns.

3.3 Proof of principle

In Figure 3.3, we compare a measurement at 1 kHz repetition rate with a measurement at 16.7 kHz. In Figure 3.3A, we plot the intensity at the probe array versus the intensity at the reference array, for each shot. In these measurements, we have kept the overall measurement time the same, with 200 shots at 1 kHz

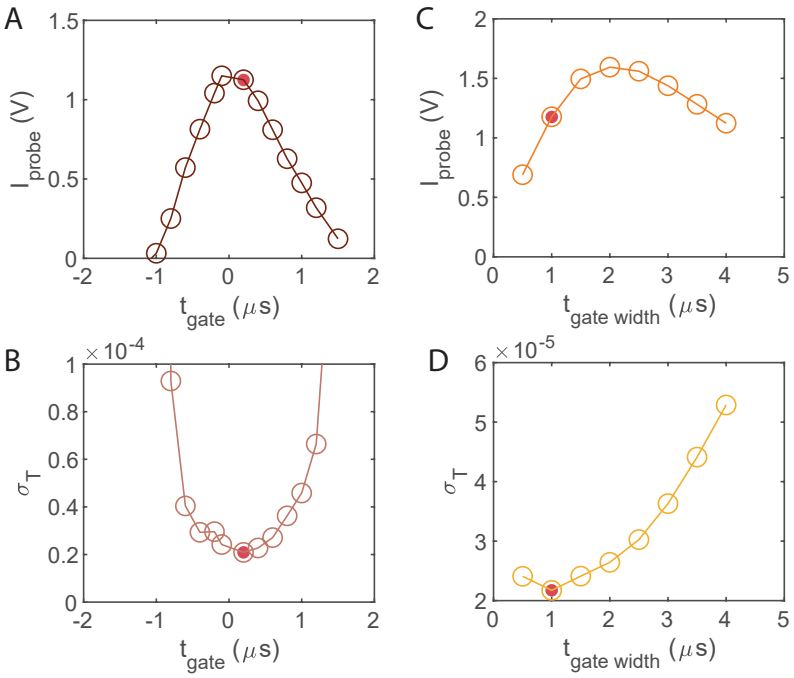

FIGURE 3.2. Optimization of the gate timing. (A) Probe intensity as a function of the gate open starting time. (B) Standard deviation of the transmission as a function of the gate open starting time. (C) Probe intensity as a function of the gate width timing. (D) Standard deviation of the transmission as a function of the gate width timing. In each figure, the red dot resembles the setting that was chosen as optimal.

and 3340 shots at 16.7 kHz. The increase in the number of shots leads to an improvement of σ_T and the signal to noise ratio, which we calculate as:

$$SNR = \frac{T}{\sigma_T} \tag{3.8}$$

The improvement in the SNR is ∼3.3, which is a little bit lower than the theoretical improvement of $\sqrt{16.7} = 4.1$.

To asses the influence of the improved signal to noise ratio on pump-probe experiments, we performed a transient absorption measurement for a solution of 4% D_2O in H_2O, where we pump and probe the OD stretch vibration at 2500 cm^{-1}, and measure the anisotropy as described in chapter 2. The results of this measurement, performed at 1 kHz and 16.7 kHz, are shown in Figure 3.3B. Again, we kept the measurement time equal for both measurements, with 200 shots for each delay point for 1 kHz, and 3340 shots for each delay point at 16.7 kHz. From these data, the advantage of measuring at a higher repetition rate is evident. The improvement of signal to noise ratio enables us to measure the anisotropy accurately over longer delay times. However, we also observe a

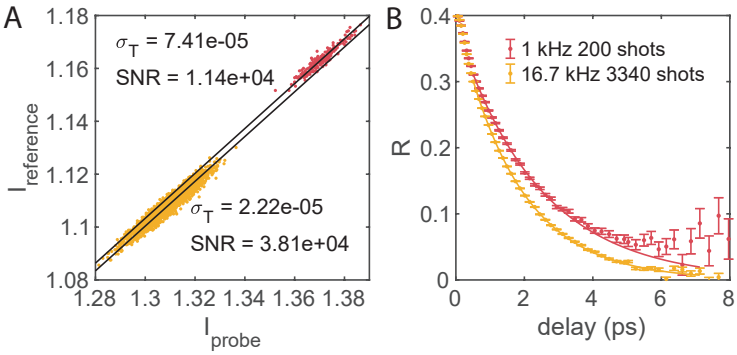

Figure 3.3. Effect of the repetition rate on the signal to noise ratio. (A) Intensity of the probe versus intensity of the reference for individual shots in a low (red) and high (yellow) repetition rate experiment, with equal measurement times. The black lines represent T, the linear fit to these points. (B) Anisotropy decay as a function of delay time for a solution of 4% D_2O in H_2O at low (red) and high (orange) repetition rate.

change in the decay rate of the anisotropy. This change will be discussed in the following section.

3.4 Sample heating

As shown in Figure 3.3B, the time constant of the anisotropy decay decreases upon increasing the repetition rate. To examine the origin of this decreased time constant, we study the isotropic and anisotropic signals as a function of the repetition rate. Figure 3.4A shows the spectrum of the ground state bleach signal at different repetition rates. We observe a clear blueshift of the spectrum upon increasing the repetition rate. In Figure 3.4B, we show the vibrational relaxation time and the thermalization time as a function of the repetition rate. These time constants are obtained from a fit of the data to the kinetic model described in section 2.2. The thermalization time does not depend on the repetition rate, while the vibrational relaxation time increases with increasing repetition. In Figure 3.4C, we show the anisotropy decay time constant as a function of repetition rate. We extract these time constants from exponential fits of the measured anisotropy decays. The time constant decreases from 2.4 ps at 1 kHz to 1.8 ps at 16.7 kHz. These three observations all indicate that the laser pulses induce a long-living heating effect that increases with increasing repetition rate. As the heating of water leads to a weaker hydrogen-bonded network, the OD stretch vibration will shift to a higher frequency. The weakening of the hydrogen-bonded water network also leads to longer vibrational relaxation times and allows water molecules to rotate faster,[48,49] thus explaining the faster decay of the anisotropy with increasing repetition rate. There are several ways to tackle this problem of laser-induced sample heating. One way would be to rotate the sample in such a way that each new pump laser shot

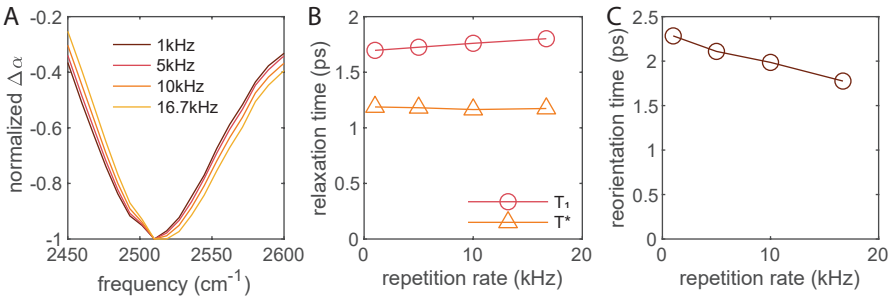

FIGURE 3.4. (A) Spectral shape of the ground state bleaching signal of the OD stretch vibration measured for a solution of 4% D_2O in H_2O at different repetition rates. (B) Vibrational lifetime (T_1) and thermalization time (T*) as a function of the repetition rate. (C) Anisotropy decay time constant as a function of the repetition rate.

is hitting a new (still cold) part of the sample. Making a sample holder that rotates fast enough for high repetition rate measurements is not impossible but certainly a technical challenge. Another, more pragmatic approach, is to cool the complete sample in such a way that the temperature during the experiment becomes equal to room temperature. We show the results of this approach in Figure 3.5, where we show a pump-probe measurement of a solution of 4% D_2O in H_2O at 16.7 kHz, cooled down to 9°C, in comparision to room temperature measurements at 1 and 16.7 kHz. In Figure 3.5A we show the influence of cooling the sample on the spectral shape of the OD stretch vibration. We see that the spectral shape of a sample at 9°C measured at high repetition rate is similar to the spectral shape of a sample at room temperature measured at 1 kHz. In Figure 3.5B we show the influence of cooling the sample on the anisotropy decay. When cooling the sample to 9°C, the decay time constant is the same as for 1 kHz room temperature measurements. This shows that cooling down the sample to compensate the heating resulting from high repetition laser shots is an effective way to perform high repetition rate pump-probe measurements.

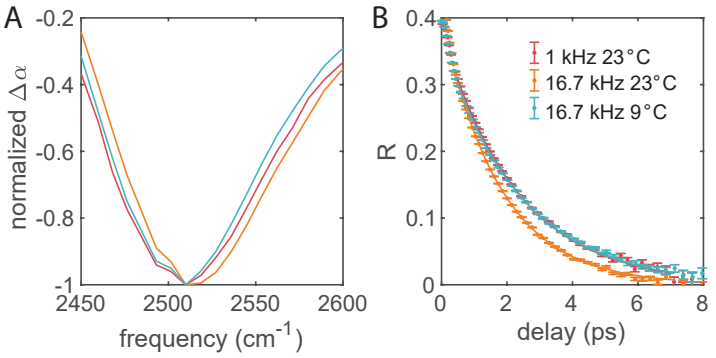

Figure 3.5. (A) Spectral shape of the ground state bleaching signal of the OD stretch vibration of a solution of 4% D_2O in H_2O measured at 1 kHz and 23°C (red), 16.7 kHz and 23°C (orange) and at 16.7 kHz and 9°C (blue). (B) Anisotropy decay as a function of the delay time at the same conditions.

4 Structure of micelles and micro-emulsions

We study the structural properties of dodecyltrimethylammonium bromide (DTAB) micelles and micro-emulsions by probing the molecular reorientation of water with polarization-resolved infrared pump-probe spectroscopy. For all systems studied, we observe that a fraction of water reorients on a much slower timescale than bulk water. This slow water fraction increases sublinear with increasing DTAB concentration, indicating an increase of the micelle size and enhanced micelle aggregation with concentration. We observe that the addition of oil to the micelle solutions, leading to the formation of a micro-emulsion, does not lead to a significant change of the fraction of slow water, showing that the added oil molecules are well solvated within the core of the micelles, and thus completely shielded from water.

4.1 INTRODUCTION

Emulsions are mixtures of water and oil, stabilized by surfactants. These can either be a mixture of oil droplets in water (oil-in-water) or water droplets in oil (water-in-oil). The surfactant molecules that stabilize emulsions are amphiphilic molecules (consisting of a hydrophilic moiety and a hydrophobic moiety). Without oil, the surfactant molecules tend to form spherical aggregates denoted as micelles. When aqueous solutions of surfactants are mixed with oil, different types (macro-, nano- and micro-emulsions) of emulsions can be formed. A special type of emulsion is the micro-emulsion. They consist of very small oil droplets from 10-100 nm. Micro-emulsions are prepared by swelling micelles with oil and form spontaneously. They are the only type of emulsions that is thermodynamically stable, which makes micro-emulsions an interesting model system of emulsions. The use of emulsions is widespread: in food industry, as carriers of pharmaceuticals and in oil recovery [50–53]. Macro- and nano-emulsions emulsions degrade over time, [54] and phase separate, a process known as syneresis. Syneresis is thus an important issue in the long term stability of macro- and nano-emulsions.

Micelles and micro-emulsions have been intensely studied with a variety of techniques such as Dynamic Light Scattering, rheology, titrations and conductivity measurements [55–58]. These techniques give insight in the overall properties and structure of these systems, but they do not provide information about their molecular properties. The molecular-scale properties of micelles and micro-emulsions can be studied with methods like pump-probe infrared spectroscopy, optical Kerr effect spectroscopy and Raman spectroscopy, [27,28,30,59–61]. Up to now, these techniques have been mostly applied to the study of reverse micelles: small water droplets surrounded by surfactants dispersed in oil [27,28,59,60]. These reverse micelles are considered to be a good model for water in confinement [27,28,59,60].

Recently, the hydration of normal micelles was studied using multivariate-curve-resolution (MCR) Raman spectroscopy [30]. Evidence was found that water molecules penetrate deeply into the micelle. Using the same method, it was found that alkane molecules added to the micelles, thus forming a micro-emulsion, are largely adsorbed in the dry core of the micelles.

In this chapter, we study the reorientation dynamics of water molecules interacting with dodecyltrimethylammonium bromide (DTAB) micelles, and of water molecules in a micro-emulsion system of toluene droplets stabilized by DTAB in water. We measure the reorientation dynamics with polarization-resolved infrared pump-probe spectroscopy (fs-IR). With this technique we can determine the fraction of water molecules that reorients like bulk water molecules, and the fraction of water molecules for which the dynamics are changed by the micelles and surfactant-covered oil droplets.

4.2 EXPERIMENTAL METHODS

SAMPLE PREPARATION We measure the reorientation dynamics of water in micelle solutions and micro-emulsions using polarization-resolved femtosecond infrared spectroscopy. The micelle solutions are prepared by dissolving different concentrations of dodecyltrimethylammonium bromide (DTAB, 99%, Sigma-Aldrich) or sodium dodecyl sulfate (SDS, 99%, Sigma-Aldrich) in 4% D_2O (99.9%D, Cambridge Isotope Laboratories) in H_2O (ultrapure milli-Q grade). Micro-emulsions are prepared by first dissolving different concentrations of DTAB in 4% D_2O in H_2O, and then adding a certain amount of toluene (99.8%, anhydrous, Sigma-Aldrich), benzene (99.9%, Sigma-Aldrich), *p*-xylene (99%, anhydrous) or hexane (95%, anhydrous, Sigma-Aldrich). The solutions were mixed with a vortex mixer and the micro-emulsions formed spontaneously, forming a transparent solution.

SPECTROSCOPY The pump-probe measurements described in this chapter are performed with the setup described in section 2.2. The FT-IR spectra are measured with a Bruker Vertex 80v FT-IR spectrometer.

4.3 RESULTS AND DISCUSSION

4.3.1 MICELLES

Figure 4.1 shows isotropic transient absorption spectra measured at different pump-probe delay times for a solution of 2.2 molal (=moles added to 1 kilogram of solvent) DTAB in isotopically diluted water. At short delay times (0.5

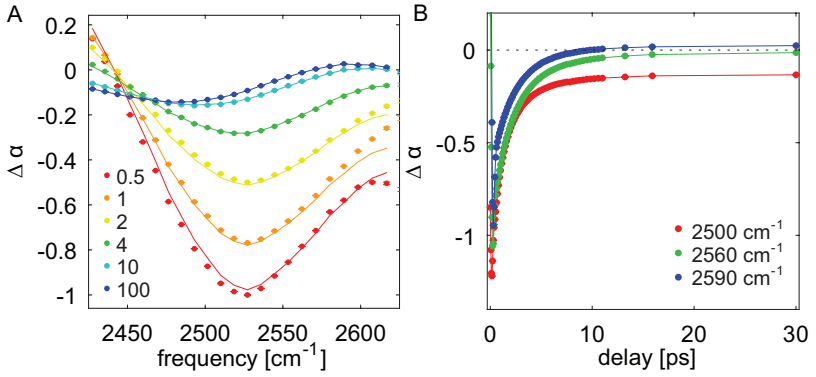

FIGURE 4.1. (A) Isotropic transient absorption change of the OD stretch vibration of HDO molecules for a solution of 2.2 molal DTAB in isotopically diluted water for six different delay times. The solid lines results from a fit to the model described in the text. (B) Isotropic transient absorption change as a function of delay time, measured for a solution of 2.2 molal DTAB in isotopically diluted water, for three different probe frequencies.

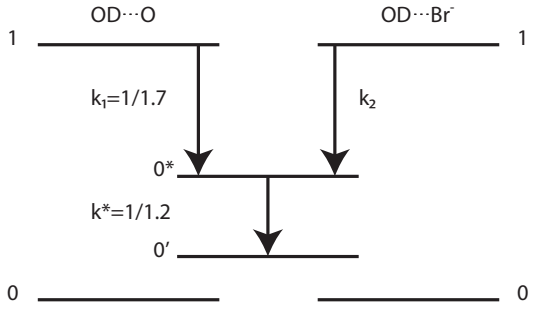

FIGURE 4.2. Schematic overview of the kinetic model that describes the relaxation dynamics of the excited OD stretch vibrations. The excited OD stretch vibrations of the OD hydrogen bonded to water, and the OD hydrogen bonded to Br^-, decay from their excited state with relaxation rates k_1 and k_2, respectively, to an intermediate state. From the intermediate state, the oscillators decay to the hot ground state with relaxation rate $k*$.

ps) we observe a ground-state bleach, and at long delay times (<10 ps) we observe a thermal-difference spectrum, indicating that the vibrational relaxation is complete and that the energy of the pump pulse has become thermal over the focus of the pump pulse. In Figure 4.1B we show pump-probe transients at three different probe frequencies. At all three frequencies we observe a bleaching that decays on a picosecond time scale. Depending on the probe frequency, the decay ends in a residual bleaching or in an induced absorption, reflecting the frequency dependence of the eventual heating effect on the absorption spectrum of the OD stretch vibration.

In order to determine the anisotropy of the transient absorption signal associated with the excitation of the OD stretch vibration, the ingrowing heating contribution to the transient absorption signal has to be subtracted. To this end, the spectra are fitted to a kinetic model describing the vibrational relaxation and the resulting rise of the heating contribution, as presented in Figure 4.2. Previous studies showed that the vibrational relaxation of the OH and OD stretch vibrations of HDO molecules strongly depends on the nature of the donated hydrogen bond of the OH/OD group[16,62,63]. For OD/OH groups donating a hydrogen bond to large halide anions like Br^- and I^- the vibrational lifetime is substantially longer than for OH/OD groups donating a hydrogen bond to the oxygen atom of a D_2O or H_2O molecule. The micelle solution contains water molecules donating hydrogen bonds to other water molecules and to Br^- ions. We thus model the relaxation with a kinetic model in which we consider two populations of excited OD vibrations, OD vibrations hydrogen bonded to H_2O molecule, and OD vibrations hydrogen bonded to Br^- ions. The excited OD vibrations decay to an intermediate state, and the intermediate state to the hot ground state[39]. We use the transient spectrum and the relaxation time constants that have been determined before for neat water (1.7

ps for the vibrational lifetime and 1.2 ps for the relaxation time constant of the intermediate state). The initial populations of the two excited OD vibrations are determined from the concentration of Br^- ions. We find a vibrational lifetime of the excited OD vibration of HDO molecules hydrogen bonded to Br^- ions of 8 ± 2 - 5.2 ± 0.4 ps for 0.36-2.2 molal DTAB.

Figure 4.3A shows the anisotropy of the transient absorption change measured for solutions of different concentrations of DTAB in isotopically diluted water. The anisotropy is constructed from the parallel and the perpendicular probing signal, that are both corrected for the ingrowing heating signal of which the dynamics is determined from the fit to the kinetic model. We compare the anisotropy dynamics of the DTAB solutions with that of neat isotopically diluted water. The anisotropy of neat water decays exponentially with a time constant of τ_r =2.5 ps, in agreement with previous work[39]. For the micelles we observe that the anisotropy transients contain a fast and a slow component. We thus fit these transients with an exponential function with an offset, $R = R_0 e^{-t/\tau_r} + R_{slow}$. For all DTAB solutions (0.36-2.2 molal) we find a reorientation time $\tau_r = 2.1 \pm 0.1$ ps, similar to the time constant of neat isotopically water[39]. This fast component is attributed to the reorientation of water molecules interacting with other water molecules and showing bulk-like behaviour. The offset R_{slow} is attributed to water molecules interacting with DTA^+ and Br^- ions. Previous work showed that the orientation dynamics of water molecules hydrogen bonded to halide ions like Br^- indeed contain a slow component[63]. To determine the number of slow water molecules hydrating DTA^+ we correct the anisotropy offset for the contribution of water that is slowed down by the bromide ions in DTAB solutions. To this purpose we measured the anisotropy dynamics of KBr as a function of concentration. The resulting anisotropy is shown in Figure 4.4A. We find that KBr slows down only a small fraction of OH groups.The normalized offset of the anisotropy is depicted in Figure 4.4B. The datapoints were fitted with a linear function with a slope of 0.027 ± 0.004, meaning that ~ 3 OH groups are slowed down per Br^- ion, i.e. the amplitude of the slow component attributed to water interacting with Br^- ions is 0.011 ± 0.002 per molal Br^-.

Figure 4.3B shows the offset as function of the surfactant concentration. It is seen that the slow water fraction increases sublinearly with the surfactant concentration. After correcting R_{slow} for the Br^- contribution, we can determine the number of slow water hydroxyl N_{slow} groups per surfactant molecule by dividing the fraction of slow water $(R_{slow}/(R_{slow} + R_0))$ by the DTAB concentration c (in mol/kg) and multiplying with the number of moles of water OH groups in 1 kilogram of water:

$$N_{slow} = \frac{R_{slow}/(R_{slow} + R_0)}{c} \cdot 110.514 \tag{4.1}$$

The number of slow OH groups per surfactant molecule is depicted in Figure 4.3C. We see that at low surfactant concentration, 23 ± 1 OH groups per surfactant molecule are slowed down. These slow OH groups are probably located near the three methyl groups of the DTA^+ surfactant head group. Previous

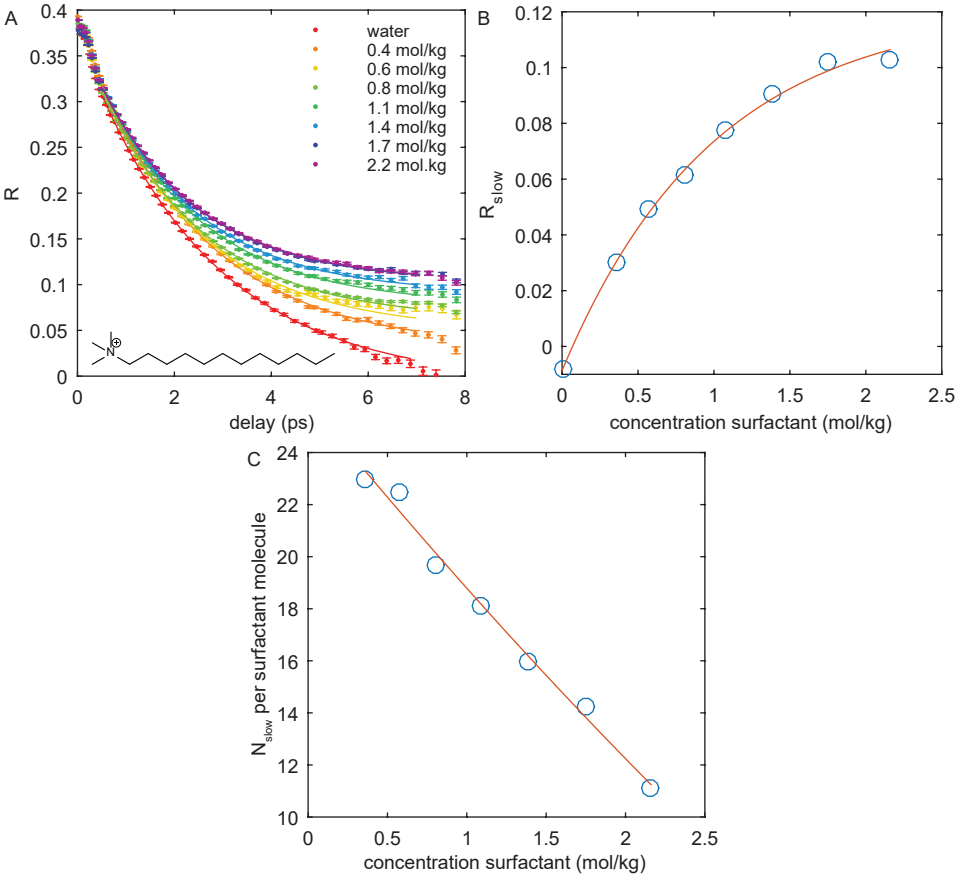

FIGURE 4.3. (A) Anisotropy decay as function of delay time for different solutions of DTAB in isotopically diluted water and neat isotopically diluted water. The solid lines are fits to an exponential function with an offset. (B) Offset of the anisotropic decay as a function of DTAB concentration. (C) Number of slow OH groups per surfactant ion as a function of DTAB concentration. The number of slow OH groups per surfactant ion is obtained after subtraction of the part of R_{slow} that can be attributed to water molecules hydrating Br^- ions. The solid lines in (B) and (C) are a guide to the eye.

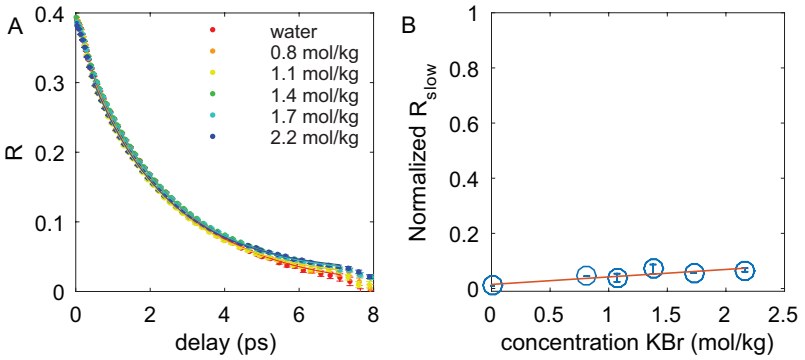

FIGURE 4.4. (A) Anisotropy decay as function of delay time of neat water and different KBr concentrations. The solid lines are a fit to a single exponential decay with an offset. (B) Normalized offset of the anisotropic decay at different KBr concentrations. The solid line is a linear fit with a slope of 0.027.

work on slow water surrounding hydrophobic groups showed that every methyl group slows down ~ 5 water OH groups, meaning that probably ~ 15 of the slow OH groups is slowed down due to their close position to the methyl groups of the DTA^+ head group[64,65]. The remaining ~ 8 OH groups are probably slowed down due their interaction with the hydrophobic tails, which implies that these OH groups belong to water molecules that penetrate into the micelle. With increasing surfactant concentration, we observe a decrease of the number of slowed down water molecules per surfactant molecule, from 23 ± 1 slowed down OH groups per surfactant molecule to 11 ± 1 slowed down OH groups per surfactant molecule.

For comparison, we also measured the anisotropy dynamics of water in SDS solutions, as shown in Figure 4.5A. SDS has a different head group, without methyl groups. In the case of SDS, we find much smaller offsets, as illustrated in Figure 4.5B. For SDS at 0.8-1.4 molal, we find only 4.0 ± 0.5 slowed down water OH groups per surfactant molecule. This finding supports the assignment of the main fraction of slow water molecules in the DTAB solutions to water molecules hydrating the methyl groups of the DTA^+ head group.

For the DTAB micelle solutions the number of slow OH groups per surfactant molecule strongly decreases with increasing surfactant concentration. There are two possible explanations for this observation: at higher concentrations, the micelles become larger, thus reducing the total surface exposed to the water solvent, or the hydration shells of the micelles start to overlap, leading to competition for solvating water molecules. The latter effect will be enhanced if the micelles aggregrate.

It is known that for micelles the aggregation number (number of surfactants per micelle, N_{agg}) and thus the micelle size, increases with increasing concentration[67–71]. This change in size leads to a change in surface area. The increase in N_{agg} of DTAB with concentration has been described with a power law by

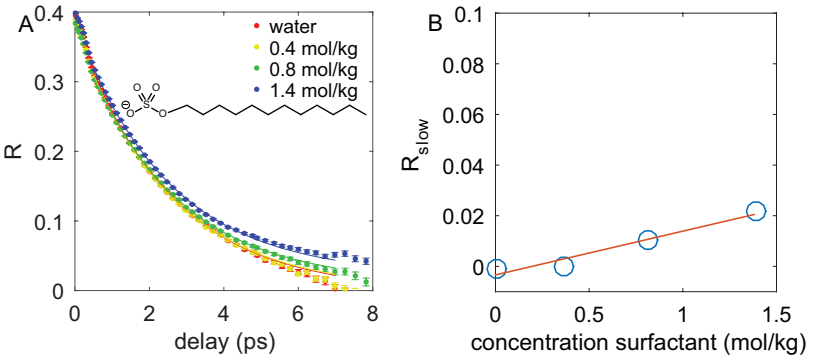

FIGURE 4.5. (A) Anisotropy decay as function of delay time of neat water and different SDS concentrations. The solid lines are fits to an exponential function with an offset. (B) Offset of the anisotropic decay as a function of SDS concentration. The solid line is a guide to the eye.

Bales and Zana, $N_{agg} = N^0(C_{aq}/cmc_0)^\gamma$, where N^0 is the aggregation number at cmc_0, cmc_0 is the critical micelle concentration (which is 14.9 mM) in the absence of salt and C_{aq} is the concentration of the surfactant counterion in the aqueous phase and γ is 0.146[68,71]. From this equation we find that N_{agg} increases from 73 for 0.4 mol/kg to 109 for 2.2 mol/kg. The corresponding change in surface-volume ratio leads to a decrease from 23 to 20 slow OH groups per surfactant molecule (see Figure 4.6). It thus follows that the growing of the micelle size with concentration only partially accounts for the observed decrease of the number of slow OH groups per surfactant molecule: we observe only 11 slowed down OH groups at 2.2 mol/kg DTAB.

The number of slow OH groups per surfactant molecule will further decrease if there is a competition for solvation water molecules at high concentrations, which implies that the hydration shells of the DTA^+ ions start to overlap. To calculate if this effect could explain the further decrease of the number of slow OH groups per surfactant, we followed the approach of Petersen et al.[66], in which the effect of the competition for hydration water is described with a chemical equilibrium, under the assumption that there is no specific interaction between the solutes, i.e. the solutes are statistically distributed over the solution. We find that this effect cannot account for the strong further decrease of the number of slow water molecules, because the competition for solvation water molecules leads to a decrease of only 2.4 slow OH groups at the highest concentration of surfactant (see Figure 4.6). From this we conclude that there must be a much stronger overlap of the micelle hydration shells than would be expected for a statistical distribution of micelles in the solution. This means that the micelles aggregate, and thereby strongly reduce the total micelle surface area that is exposed to water. Micelle aggregation implies that the head groups of the DTA^+ surfactant ions of different micelles aggregate, with the negatively charged Br^- ions as glue in between the positively charged

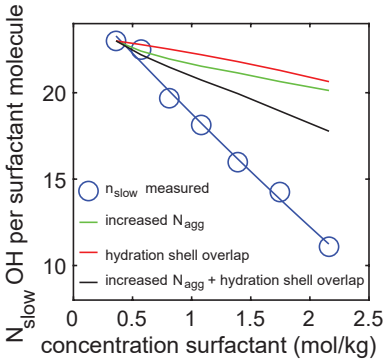

FIGURE 4.6. Number of slowly reorienting OH groups resulting from the pump-probe measurements (blue), calculated from the increase in aggregation number N_{agg} (green), calculated from the overlap of hydration shells which results in a competition for hydration water, based on the model described by Petersen et al.[66] (red), and the combined effect of increased N_{agg} and overlapping hydration shells (black).

head groups. This finding is in line with other studies of aqueous solutions of quaternary ammonium ions (that constitute the head group of DTA^+). Aqueous solutions of tetra-n-alkylammonium salts also show strong aggregation at higher concentrations, leading to a strong decrease of the number of hydrating water molecules per tetra-n-alkylammonium ion[63].

4.3.2 MICRO-EMULSIONS

We prepared micro-emulsions by swelling the DTAB micelles with toluene. To check whether the added oil is taken up by the micelles we measured the infrared absorption spectrum of the emulsions. In Figure 4.7A the IR absorption spectra of emulsions with different concentrations of toluene, and of pure toluene are shown. We subtracted the spectrum of DTAB from all spectra. Figure 4.7B shows the spectral region of the C-H in plane aromatic bending modes that are specific for toluene. Figure 4.7C shows the area under the 1082 cm^{-1} peak as a function of the toluene concentration. We observe a linear increase of the peak area with the concentration of toluene. This result demonstrates that all added toluene is taken up by the micelles.

Figure 4.8A shows the anisotropy decay of a solution of 1.4 mol/kg DTAB and different toluene concentrations in water. Surprisingly, we observe that the offset of the anisotropy decay does not change significantly when changing the oil concentration. This is surprising, because at the highest oil concentration, the volume of oil added to the micelles is 1.8 times the volume of the micelles.Using the offset of the anisotropy decay, we calculated the number of slow OH groups per surfactant molecule, as shown in Figure 4.8B. The number of slow OH groups per surfactant molecule does not change with increasing concentrations of oil. Apparently, the added oil molecules are well embedded within the core

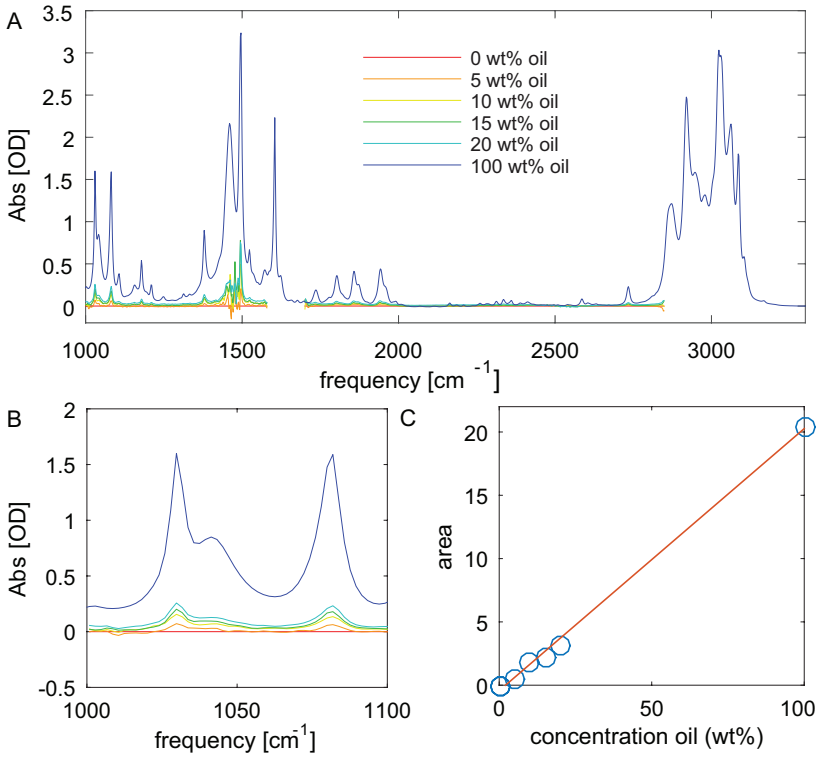

FIGURE 4.7. (A) FTIR spectra of emulsions with a concentration of 1.4 mol/kg DTAB and different toluene concentrations. The spectrum of DTAB is subtracted from the spectra. (B) Zoom-in of the spectral region of the in plane aromatic C-H bending bands. (C) Area of the 1082 cm^{-1} peak as a function of toluene concentration.

of the surfactant covered oil droplets, and thus completely shielded from water.

In Figure 4.9A we show the anisotropy dynamics of solutions containing a constant oil concentration of 10 wt%, and different surfactant concentrations. We observe that at all surfactant concentrations the offset of the anisotropy is similar for the micro-emulsion and the micelle with the same surfactant concentration. Figure 4.9B depicts the number of slow OH groups per surfactant molecule as a function of surfactant concentration for surfactant solutions with 10 wt% oil (micro-emulsions, red) and without oil (micelles, blue). Even at the highest oil to surfactant ratio (10% oil in 0.36 molal DTAB, $V_{oil}/V_{DTAB} = 2.4$), there is no significant difference in number of slowed down OH groups.

The results above show that in toluene-based emulsions with the surfactant DTAB, the oil is completely embedded in the emulsion core, leading to no observable change in the anisotropy and thus in the fraction of slowed-down water molecules. To test the generality of this result, we also measured the anisotropy of emulsions with other oils. To this end we prepared emulsions consisting of 1.4 mol/kg DTAB and 10 wt% xylene, benzene or hexane. The

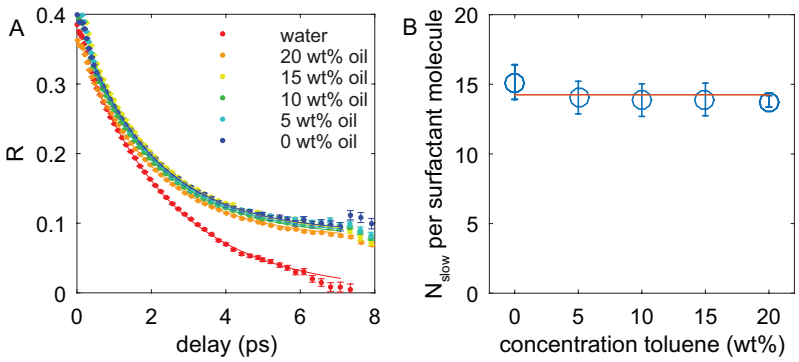

FIGURE 4.8. (A) Anisotropy decay as function of delay time for emulsions with a DTAB surfactant concentration of 1.4 mol/kg and different concentrations of toluene. The solid lines are fits to an exponential function with an offset. (B) Number of slow OH groups per surfactant molecule as a function of toluene concentration. The solid line is a guide to the eye.

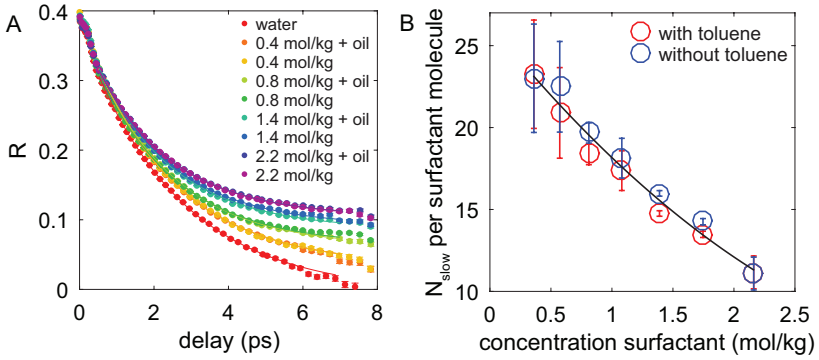

FIGURE 4.9. (A) Anisotropy decay as a function of delay time for micelle solutions and emulsions with 10 wt% oil for four different surfactant concentrations. The solid lines are fits to an exponential function with an offset. (B) Number of slow OH groups per surfactant of emulsions with different surfactant concentrations, with and without oil. The solid lines are a guide to the eye.

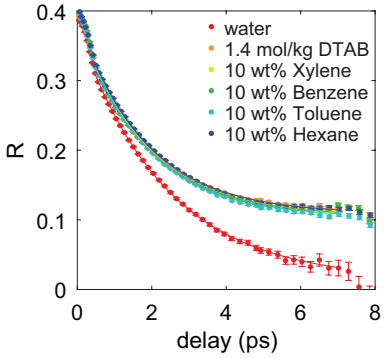

FIGURE 4.10. Anisotropy decay as function of delay time for emulsions with 10 wt% of different oils, at a 1.4 mol/kg surfactant concentration. The solid lines are fits to an exponential function with an offset.

anisotropy of these different emulsions is shown in Figure 4.10. We observe that the anisotropy dynamics of the emulsions with different oils is remarkably similar to each other, and more importantly, similar to the anisotropy dynamics of a 1.4 mol/kg DTAB solution without oil. The observation that the added oil molecules are well embedded in the core of the droplet and completely shielded from the surrounding water is thus a quite general result, independent of the nature of the oil. For all micro-emulsions and the DTAB solution without oil, we find that 17 ± 1 water OH groups are slowed down, consistent with Figure 4.3C.

4.3.3 COMPARISON WITH OTHER WORK

Recently, similar micellar systems were studied using multivariate-curve-resolution (MCR) Raman spectroscopy [30]. The group of Ben-Amotz found that water molecules penetrate into micelles, and over 20% of the surfactant tail methylene groups stay in contact with water. We find similar results for micelles composed of DTAB surfactant molecules. For SDS micelles we observe that only 4 water OH groups are slowed down, which means that not more than ∼10% of the surfactant methylene groups can be in contact with water.

Bales and Zana studied the hydration of DTAB micelles using electron paramagnetic resonance (EPR), and found that the number of hydration water molecules per surfactant molecule decreases with increasing N_{agg} and thus increasing DTAB concentration,[68] which is in agreement with our findings.

The group of Ben-Amotz also studied the uptake of hydrophobic oil molecules by micelles, similar to our approach of creating micro-emulsions by adding oil to the micellar systems. Based on the vibrational frequencies of the CD stretch vibration of the hydrophobic probes, they found that the added hydrophobic probes are well solubilized within the dry oil-like core of the micelle[30]. This finding is in good agreement with our present results, in which

we see no change in slow water fraction upon adding oil to micelles, showing that the added hydrophobic molecules are completely embedded in the micelle and shielded from water. In a previous EPR study it was also found that the number of hydrating water molecules per surfactant molecule does not change upon adding heptane to SDS micelles [72].

4.4 CONCLUSIONS

We studied the reorientation dynamics of water molecules surrounding micelles and micro-emulsions using polarization-resolved femtosecond pump-probe spectroscopy. We observed that a fraction of the water molecules has very slow reorientation dynamics. For micelles, the number of slow OH groups per surfactant molecule decreases with increasing surfactant concentration, from 23 ± 1 slow OH groups per surfactant molecules at low concentrations to 11 ± 1 slow OH groups at high concentrations. This decrease results in part from an increase in size of the micelles with increasing surfactant concentration, and in part from the increase in overlap of the hydration shells of the micelles. The latter contribution is much stronger than would be expected in case the micelles would be statistically distributed over the solution, which indicates that the micelles aggregate at high surfactant concentration. For micro-emulsions we find no significant difference in the number of slow OH groups per surfactant upon the addition of oil, even in case the volume of oil added to the micelles is 1.8 times the volume of the micelles. This indicates that in micro-emulsions, the added oil molecules are completely embedded in the cores of the droplets.

5 Water reorientation dynamics in nano-emulsions

Nano-emulsions are water-oil mixtures consisting of 20-500 nm droplets of one component embedded in a liquid of the other component. Nano-emulsions are usually kinetically stable and can be prepared with low concentrations of surfactants. Even though nano-emulsions are used ubiquitously, their molecular properties are poorly understood. Here we study the orientational dynamics of water molecules in oil-in-water nano-emulsions using polarization resolved pump-probe infrared spectroscopy, for varying surfactant concentrations, droplet sizes, and temperatures. We find that the majority of the water molecules reorients with the same time constant as in bulk water, but that a small fraction of the water molecules reorients on a much longer time scale. These slowly reorienting water molecules are interacting with the surface of the oil droplet. The fraction of slowly orienting water molecules depends on the oil volume fraction, but shows a negligible dependence on the average droplet size. This finding indicates that the total surface area of the oil droplets is quite independent of the average droplet size, which suggests that the oil droplets do not have a smooth spherical shape and probably are quite corrugated showing protrusions into the water phase.

5.1 INTRODUCTION

Emulsions constitute a very interesting type of mixture, since it combines two immiscible liquids into one solution. Emulsions either consist of oil droplets dispersed in water, or of water droplets dispersed in oil. The droplets are often stabilized by surfactant molecules. Emulsions find many applications in the food and the pharmaceutical industry.[73–75] The droplet size of emulsions can range from a few nanometers to tens of micrometers. The emulsions with the biggest droplet size, the macroemulsions, contain droplets with diameters between 1 and 100 μm, and are known to be unstable. The emulsions with the smallest droplets, the so-called micro-emulsions, have droplet diameters on the order of 10 to 100 nm. These emulsions are thermodynamically stable, but usually require a high concentration of surfactant, making them unappealing for practical applications in industry. The emulsions with intermediate droplet sizes, from 20 to 500 nm, are called nano-emulsions (please note that nano-emulsions have bigger droplet sizes than micro-emulsions. These systems were named independent from each other). Nano-emulsions are not thermodynamically stable, but they are kinetically stable (they usually have a long shelf life time) and they can be prepared with a low concentration of surfactants. The combination of these factors make nano-emulsions a very attractive platform for industrial applications.[73,74,76]

There have been a lot of studies exploring how nano-emulsions can best be prepared, in particular on how the droplet size can be predicted and controlled.[75,77–79] In contrast, there have only been a few studies of the properties of nano-emulsions on the molecular level, mainly exploring the role of the surfactant of the oil phase in the droplet stabilization.[80–84] In this Chapter, we report on a study of the reorientation dynamics of water molecules in diglyceride-in-water nano-emulsions using polarization-resolved infrared pump-probe spectroscopy. We performed these measurements for different surfactant concentration, droplet sizes and temperatures.

5.2 EXPERIMENTAL METHODS

SAMPLE PREPARATION The studied nano-emulsions consist of deionized water (ultrapure milli-Q grade, prepared using MILLIPORE Synergy 185 system), econa oil containing 80 wt% of diacylglycerols and 20 wt% triacylglycerols (Kao, Tokyo, Japan), and the surfactant sodium dodecyl sulfate (Sigma Aldrich, Schnelldorf, Germany). The nano-emulsions are prepared according to the recipe presented in Ref.[77]. All chemicals are used as received. To create the nano-emulsions, an aqueous solution of the desired SDS concentration (116 mM, 87 mM and 58 mM) was prepared by adding SDS slowly to the water while stirring using a rotor-stator mixer (Silverson L4RT-A) until full dissolution was reached. Subsequently 53 wt% of oil was added slowly to the aqueous solution, while stirring at 8000 rpm using a stator grating with 2 mm holes. The emulsion was then mixed for 5 minutes to obtain a microscale emulsion.

To create nanoscale emulsions from these microscale emulsions, they were further processed using an ultra high-pressure impinging jet mixer (Microfluidizer M-110S, Microfluidics), with an inlet pressure of 120 MPa. A Y-type ceramic chamber (F20Y) was used with a minimum passage of 75 μm. The microscale emulsion was processed through the interaction chamber at different pressures. The temperature of the emulsion was controlled with a water bath to not exceed room temperature. The thus prepared nanoscale emulsions were stored at 4°C until further use.

DROPLET SIZE CHARACTERIZATION The droplet size of the nano-emulsions was measured using dynamic light scattering, using a Zetasize Nano ZS (Malvern Instr., Malvern, UK) in backscattering geometry. Before the measurement, the nano-emulsions were strongly diluted with demineralized water to minimize multiple scattering and to make the bulk viscosity very similar to that of water. One ml of the diluted nano-emulsion was pipetted into a plastic cuvette and placed into the instrument. In order to compare the main features of the multiple, often bimodal, size distributions, we show data mainly as surface-mediated mean particle size $D[3,2]$ of the dominating peak, in combination with the relative volume fraction of the dominating peak against the whole distribution. The measure is defined as $D[3,2] = \left[\sum_i^M \frac{\phi_i}{d_i}\right]^{-1}$. The size distribution as measured involves the diameter d_i and relative percent-based volume fraction ϕ_i for each size class i. The sum over all relative volume fractions in the distribution is 1.

SPECTROSCOPY The pump-probe measurements described in this chapter are performed with the setup described in section 2.2.

5.3 RESULTS

We prepared several nano-emulsions with different surfactant concentrations and at different processing pressures. All these emulsions were prepared with the same amount (53 wt%) of oil. Figure 5.1 shows the oil droplet diameter of the emulsions, including the droplet sizes of micro-scale emulsions that were not processed using the impinging jet mixer (shown at 0 bar). We see that for the micro-scale emulsions, the droplet size is inversely proportional to the surfactant concentration. After processing the emulsions to form nano-emulsions, the droplet size does not have this surfactant concentration dependence anymore. We observe that at higher processing pressures, smaller droplets are formed. The diameter of the droplets of the nano-emulsions ranges between ∼120 and ∼290 nm. Figure 5.2 shows the droplet size as a function of processing pressure for all surfactant concentrations, at the day of preparation (day 1) and 30 days later. We observe that within this time window, the emulsions prepared using the ultra high-pressure impinging jet mixer, do not change significantly in size.

Figure 5.3A shows isotropic transient absorption spectra at different delay times, resulting from pumping and probing the OD stretch vibration in a nano-emulsion solution of 53% econa oil droplets with a diameter of 145 nm

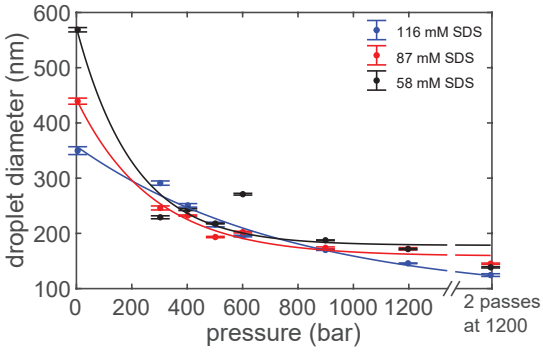

FIGURE 5.1. Droplet diameter as a function of processing pressure of the ultra high-pressure impinging jet mixer, for different surfactant concentrations. The values at 0 bar are the droplet sizes of micro-scale emulsions that were not processed using the ultra high-pressure impinging jet mixer. The values reported at the highest pressure correspond to emulsions that passed through the impinging jet mixer twice at a pressure of 1200 bar. The solid lines are guides to the eye.

(processed at 1200 bar) and 116 mM SDS in isotopically diluted water. At early delay times we observe a decreased absorption due to the bleaching of the ground state and stimulated emission out of the first excited vibrational state back to the ground state. At long delay times, we observe a thermal difference spectrum. Figure 5.3B shows the transient absorption signals at 2520 cm^{-1} measured in parallel and perpendicular polarization configuration as a function of delay time, and the isotropic signal that is constructed from these signals using equation 2.25. The isotropic, parallel and perpendicular signals do not decay completely to zero, because of the long lasting thermal difference signal that is also shown in the transient absorption spectrum of Figure 5.3A. This final thermal difference signal has the same magnitude in the parallel and perpendicular polarization configuration, meaning that the thermal difference signal is isotropic. To distinguish the signal of the OD stretch vibrational excitation from the total transient absorption signal, we fit the isotropic signal to a kinetic model that describes the vibrational relaxation of the OD oscillators and the ingrowing heating signal. The result of this fit is shown as the solid lines in Figure 5.3A. After subtracting the isotropic heating, we obtain the pure OD vibrational excitation signal of which we can determine the delay-time-dependent anisotropy.

Figure 5.4A shows the anisotropy decay of solutions of different concentrations of SDS in isotopically diluted water. For neat water, we fit the anisotropy decay with an exponential function, and we obtain a reorientation time of 2.5 ps. For the solutions containing SDS the anisotropy does not decay to zero. We fit the anisotropy decay of the SDS solutions with an exponential decay with an offset. The extracted reorientation time for the SDS solutions is 2.3 ps, and the offset increases with increasing SDS concentration. This means that

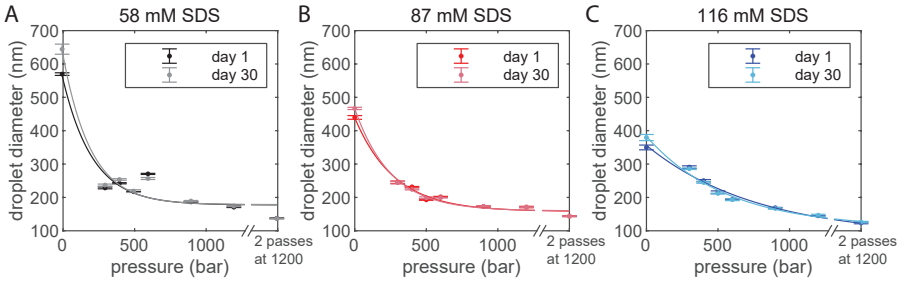

FIGURE 5.2. Droplet diameter as a function of processing pressure of the ultra high-pressure impinging jet mixer, for surfactant concentrations of (A) 58 mM (B) 87 mM and (C) 116 mM SDS. We show the stability of the emulsions by reporting the droplet diameter measured on the day of emulsions preparation (day 1) and 30 days later (day 30). The solid lines are guides to the eye.

a large fraction of the water molecules is reorienting with the same reorientation time as bulk water, while a small fraction is reorienting on a much longer times scale. We assign the slow water molecules to water molecules that are in direct contact with the SDS solute molecules. Figure 5.5 shows the offset of the anisotropy of the SDS solutions, R_{slow}, as a function of concentration. We fit R_{slow} with a linear function with a slope of 0.089±0.009, meaning that each surfactant molecule slows down 25±2 water OH groups. Figure 5.4B shows the anisotropy decay of three nano-emulsion solutions, with the same surfactant concentrations as shown in Figure 5.4A. The oil droplets of three nano-emulsion displayed here are all of similar size, possessing a diameter of 195 nm. For the nano-emulsions, we fit the reorientation time with the same reorientation time that we found for the SDS solutions, of 2.3 ps. We observe a larger offset for the nano-emulsions than for the solutions that only contain SDS, which means that more water is slowed down in the nano-emulsions. This larger fraction of slow water can be explained from water molecules interacting with the oil molecules of the emulsion. The offset of the nano-emulsions increases with increasing surfactant concentration just as in the case of the solutions only containing the surfactant.

To get a better understanding of the influence of the surfactant concentration and droplet size on the amount of slow water, we measured the anisotropy decay for a series of droplet sizes at different surfactant concentrations. The concentration of oil is kept constant throughout the whole experiment. Figure 5.6A shows the anisotropy decay of nano-emulsions with different droplet diameters at 116 mM SDS concentration. As in Figure 5.4, the offset of the emulsion is higher than that of the solution only containing the surfactant. Interestingly, we do not observe a significant difference between the offsets of nano-emulsions with different droplet sizes. At the other surfactant concentrations, shown in Figure 5.6B, we also do not observe a significant effect of droplet size on the offset. We do see that the total offset is increasing with surfactant concentration, similar to what we found for solutions only containing the surfactant. This

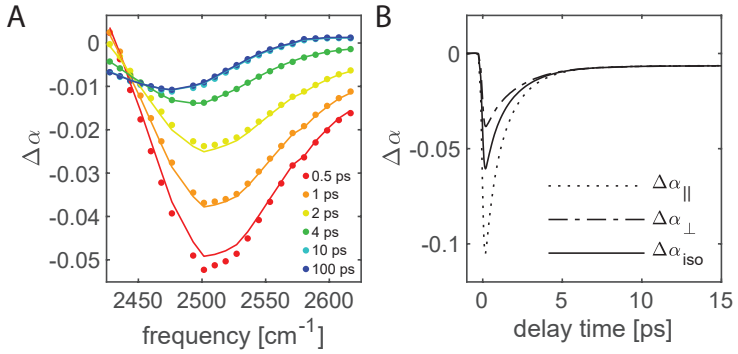

FIGURE 5.3. (A) Isotropic transient absorption spectrum of the OD stretch vibration of HDO molecules for a nano-emulsion composed of 50% econa oil and 116 mM SDS, and a diameter of 145±0.6 nm in isotopically diluted water, for different delay times. (B) Transient absorption change as a function of delay time at 2520 cm^{-1}, for the parallel, perpendicular and isotropic signal, for a nano-emulsion composed of 50% econa oil and 116 mM SDS, and a diameter of 145±0.6 nm in isotopically diluted water.

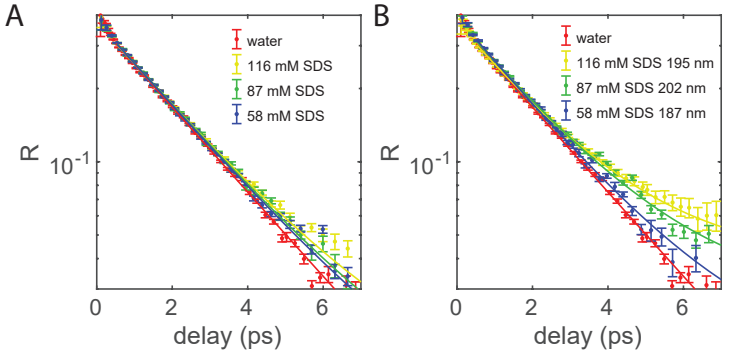

FIGURE 5.4. (A) Anisotropy decay as a function of delay time for solutions of 116, 87 and 58 mM SDS in isotopically diluted water. (B) Anisotropy decay as a function of delay time for nano-emulsions containing 50% econa oil and 116, 87 and 58 mM SDS in isotopically diluted water. All nano-emulsions have a similar droplet diameter of ∼195 nm. The solid lines are fits to an exponential function with an offset.

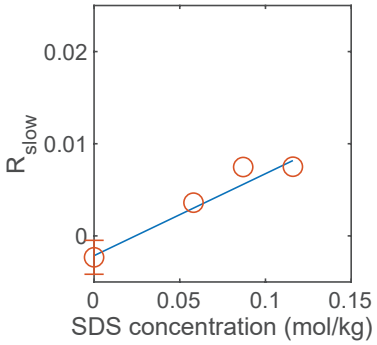

FIGURE 5.5. Offset of the anisotropic decay for as a function of SDS concentration. The solid line is a linear fit with a slope of 0.089.

observation is striking: the slow water molecules are water molecules interacting mainly with the oil and surfactant on the droplet surface. If the droplets would have a smooth spherical surface, the total surface area of the droplets is expected to decrease when the droplet diameter increases and the oil concentration is kept constant. However, from our results we conclude that the amount of water interacting with the droplets stays more or less the same for droplets with average diameters ranging from ∼120 to ∼290 nm, as measured with dynamic light scattering is different. This indicates that the interacting surface area with water stays more or less the same for all these droplet sizes.

Figure 5.7 shows the droplet size of a nano-emulsion composed of 50% econa oil and 116 mM SDS in isotopically diluted water as a function of temperature. The droplet size does not change significantly upon changing the temperature. We measured the influence of temperature on the water reorientation dynamics for a 116 mM 123 nm diameter nano-emulsion, by again measuring the anisotropy of the OD stretch vibrational excitation as a function of delay time. We measured in a range of 20-60°C, at higher temperatures the nano-emulsion could not be measured because it became strongly scattering in the mid-IR. Figure 5.8A shows the anisotropy dynamics of this nano-emulsion at different temperatures. It is clearly seen that the anisotropy decay becomes faster with increasing temperature.

To analyze the anisotropy decay curves of the nano-emulsion, we first determined the reorientation time τ_r of neat isotopically diluted water at different temperatures in an independent set of measurements. Figure 5.9A shows the anisotropy decay of isotopically diluted water as a function of delay time for different temperatures. These anisotropy decays can be fitted well with an exponential function without an offset. The obtained exponential time constants are shown in figure 5.9B, where they are plotted on a logarithmic scale as a function of inverse temperature. The time constant decreases with increasing temperature, and this this temperature dependence can be well described with

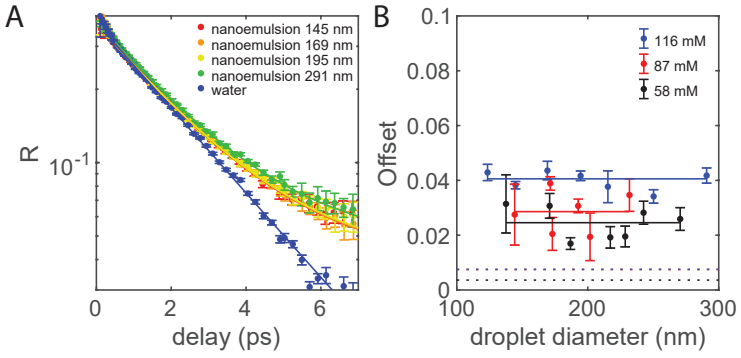

FIGURE 5.6. (A) Anisotropy decay as a function of delay time for nano-emulsions composed of 50% econa oil and 116 mM SDS in isotopically diluted water, with different oil droplet diameters. The solid lines are fits to an exponential function with an offset. (B) Offset of the anisotropic decay for nano-emulsions at different SDS concentrations as a function of droplet diameter. The solid lines are the average of each SDS concentration series. The dashed lines represent the offsets observed for solutions only containing SDS.

the following Arrhenius equation:

$$1/\tau_r = Ae^{-E_{act}/RT} \tag{5.1}$$

Where A is the pre-exponential factor, E_{act} is the activation energy (in J/mol), and R is the gas constant. For isotopically diluted water we find the activation energy to be 14 kJ/mol, in agreement with previous findings [49,65,85].

Subsequently, we fitted the anisotropy decays of the nano-emulsion at different temperatures to an exponential decay with an offset, where we fix the exponential time constant to a value that follows from the Arrhenius fit of the time constants observed for neat water. Figure 5.8B shows the offset that we obtain with this procedure. The resulting offset is constant which means that temperature has little effect on the amount of water molecules that is interacting with the oil droplets.

5.4 DISCUSSION

5.4.1 COMPARISON MICRO- AND NANO-EMULSIONS

Figures 5.4 and 5.6 clearly show that nano-emulsions containing Econa oil plus SDS possess a larger fraction of slow water molecules than solutions that only contain the same amount of SDS. This extra amount of slow water is attributed to water molecules that are interacting with the oil. In this respect, the properties of nano-emulsion are different from those of micro-emulsions that we investigated with the same technique before.[86] In that study, we performed a similar experiment, but instead of nano-emulsions we created micro-emulsions

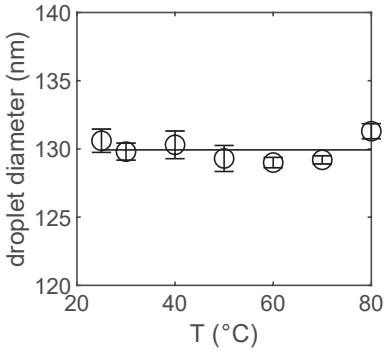

FIGURE 5.7. Droplet diameter as a function of temperature, for a a nano-emulsion composed of 50% econa oil and 116 mM SDS in isotopically diluted water.

for which the droplets are much smaller, possessing diameters <10 nm. For micro-emulsions, we observed that adding oil to the surfactant solutions did not change the anisotropy offset and thus did not change the fraction of slowly reorienting water molecules. This means that for micro-emulsions, the water phase is not in direct contact with the oil phase. There is thus a clear difference between the two types of emulsions, where in the case of micro-emulsions, the surface of the oil droplets is completely covered with surfactant molecules shielding the oil surface, and in the case of nano-emulsions, the surface of the oil droplets is not completely covered with surfactant molecules, thus allowing the water molecules to interact with the oil.

5.4.2 INDEPENDENCE OF SLOW WATER FRACTION ON DROPLET SIZE

Figure 5.6 shows that the fraction of slowly reorienting water is not dependent on the droplet size. This is surprising, because the amount of slow reorienting water is dependent on the amount of droplet surface with which the water interacts. If the oil droplets would possess a smooth spherical shape, their total surface is expected to increase with decreasing droplet size and thus the amount of slowly reorienting water. The total droplet surface exposed to water can be estimated from the fraction of slow water and a reasonable assumption about the thickness of the hydration layer that is affected in its reorientation dynamics by the near presence of the oil droplet surface. The nano-emulsion contains ∼50% of oil and ∼50% of water. From Fig. 5.6 it follows that a fraction of ∼0.03/0.4 = 0.075 of the water is slow for all studied droplet sizes, which corresponds to 0.038 m^3 in 1 m^3 emulsion. Hydrophobic hydration effects have been found to be short range. If we estimate the thickness of the affected water layer to be ∼0.5 nm, the affected water volume corresponds to a total surface of $0.038/5\times10^{-10}=7.5\times10^{7}$ m^2. It is interesting to compare this surface with that of perfect spherical nanodroplets with a diameter of 150 nm. The volume

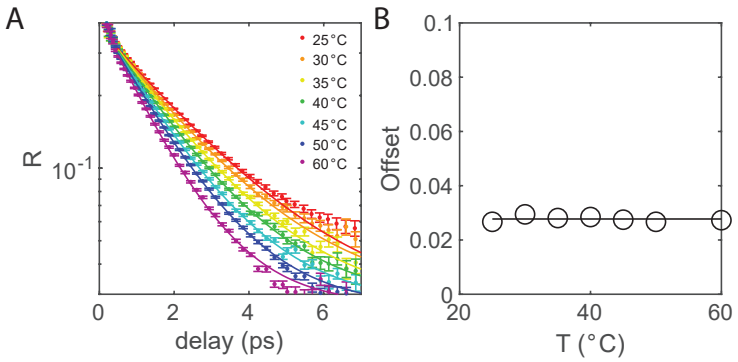

FIGURE 5.8. (A) Anisotropy decay as a function of delay time at different temperatures, for a nano-emulsion composed of 50% econa oil and 116 mM SDS in isotopically diluted water with a diameter of 123 nm at room temperature. The solid lines represent fits of the data to an exponential function with an offset. (B) Offset of the anisotropic decay as a function of temperature, for a nano-emulsion composed of 50% econa oil and 116 mM SDS in isotopically diluted water with a diameter of 123 nm at room temperature. The solid line shows the average of the offsets.

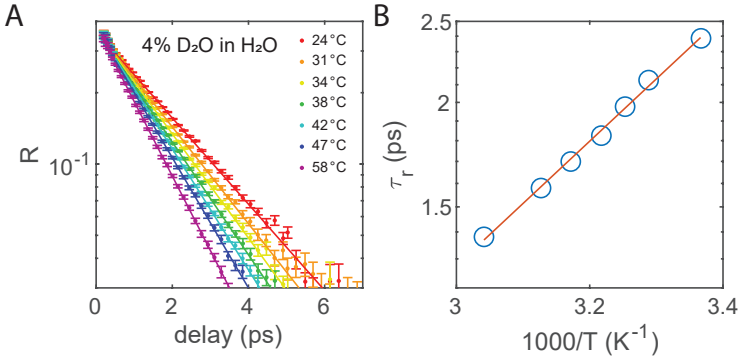

FIGURE 5.9. (A) Anisotropy decay of the OD stretch vibration as a function of delay time for a solution of 4% D_2O in H_2O, at different temperatures. The solid lines are fits to an exponential function. (B) Reorientation time τ_r as a function of inverse temperature, obtained from the fit to the anisotropy decay. The solid line represents an Arrhenius-type fit.

of such a nanodroplet is 1.77×10^{-21} m^3 and its surface is 7.07×10^{-14} m^2. In 1 m^3 nano-emulsion there are $0.5/1.77\times10^{-21} = 2.83\times10^{20}$ droplets with a total surface area of 2×10^7 m^2, which is 3.75 times smaller than the surface area that we derive from the fraction of slowed down water. This comparison indicates that the oil droplets in the nano-emulsion do not have a smooth spherical shape and probably are quite corrugated showing protrusions into the water phase.

The non-spherical, corrugated shape of the oil droplets offers an explanation for the observation that the amount of slow water does not depend on the average droplet size (as shown in Fig. 5.6). The experimentally derived effective surface area of 7.5×10^7 m^2 to a characteristic radius. A volume of 1 m^3 of nano-emulsion contains n=$0.5/((4/3)\pi R^3)$ droplets with a total surface area of $n \times 4\pi R^2$ m^2. It follows that $R = 1.5/7.5 \times 10^7 = 20$ nanometer, which can thus be interpreted as the characteristic curvature of the protrusions of the nanodroplets, that is independent of the overall size of the nanodroplet. This independence of the characteristic radius of the protrusions on the average droplet size, implies that larger nanodroplets will show more protrusions than nanodroplets with a small diameter, with the result that the surface of the nanodroplet increases proportional to its volume, instead of proportional to its volume divided by its diameter. As a consequence, the amount of water that is slowed down by the interaction with the oil droplets is independent of the average droplet size.

5.5 CONCLUSIONS

We studied the reorientation dynamics of water molecules surrounding nano-emulsion droplets using polarization-resolved femtosecond pump-probe spectroscopy. The nano-emulsions contain oil droplets with average diameters ranging from 120 to 290 nm, as determined with dynamic light scattering (DLS). We observe that a fraction of the water molecules in these nano-emulsions shows a much slower reorientation than the water molecules in bulk liquid water. This fraction of slow water is higher for nano-emulsions than for solutions that only contain surfactant molecules at the same concentration. This indicates that, contrary to what we found before for micro-emulsions, water is in contact with oil molecules at the surfaces of the nano-emulsion droplets. For a nano-emulsion consisting of 50% oil and 50% water, we find that the fraction of slow water amount to 7.5% of the total water volume. Assuming an affected water layer thickness at the oil droplet surface of ∼0.5 nanometer, this volume fraction corresponds to a total oil droplet surface of 7.5×10^7 m^2 per m^3 of nano-emulsion. This surface would correspond to perfectly smooth spherical droplets with a diameter of 40 nanometer, which is significantly smaller than the average droplet size of the nanodroplets that we determine with DLS. This finding indicates that the droplets do not have a smooth spherical shape but probably are quite corrugated showing protrusions into the water. We observe that the amount of slowed-down water is independent of the average droplet size. This indicates that nanodroplets with a large average diameter show more protrusions

than nanodroplets with a small diameter, with the result that the surface of the nanodroplets increases more or less proportional to their volume, instead of proportional to their volume divided by their radius, as would have been the case for perfectly spherical nanodroplets.

6 Hyaluronan biopolymers release water upon gelation

We study the relation between the macroscopic viscoelastic properties of aqueous hyaluronan polymer solutions and the molecular-scale dynamics of water using rheology measurements, differential dynamic microscopy, and polarization-resolved infrared pump-probe spectroscopy. We observe that the addition of hyaluronan to water leads to a slowing down of the reorientation of a fraction of the water molecules. Near pH 2.4, the viscosity of the hyaluronan solution reaches a maximum, while the number of slowed down water molecules reaches a minimum. This implies that the water molecules become on average more mobile while the solution becomes more viscous. This observation indicates that the increase in viscosity involves the expulsion of hydration water from the surfaces of the hyaluronan polymers, and a bundling of the hyaluronan polymer chains.

6.1 INTRODUCTION

Hyaluronan is a biopolymer that is present in many biological tissues and fluids, including cartilage and synovial fluid.[87,88] Hyaluronan is composed of repeating D-glucuronic acid and N-acetyl-D-glucosamine disaccharide units (see Figure 6.1), and is found in nature in a large range of sizes (from oligosaccharides to millions of Daltons). Hyaluronan is involved in a wide range of biological functions, including skin hydration and joint lubrication,[89–91] cancer progression and metastasis[92,93] and regulation of cell behaviour.[93,94] Its unique properties are to a large extent thought to be linked to its high water-binding capacity (the ability to hold water during centrifugation[95,96]). This water-binding capacity was found to be the largest in a quite narrow pH range around pH 2.4, where solutions of hyaluronan turn into an elastic gel referred to as a putty state.[97]

The origin of the sol-gel transition at pH=2.4 was extensively studied by measuring the rheology.[97–101] It was hypothesized that near pH 2.5, interchain hydrogen bonds are formed between the carboxylic acid and acetamide groups, thereby forming a high density of crosslinks leading to the formation of a putty state.[98,99] This hypothesis, was recently confirmed by two-dimensional femtosecond infrared spectroscopy.[102] In this paper, we study the fate of the water molecules in aqueous hyaluronan solutions during pH-induced changes in macroscopic viscoelastic properties, using a combination of rheology measurements, differential dynamic microscopy, and polarization resolved femtosecond infrared pump-probe spectroscopy.

6.2 EXPERIMENTAL METHODS

SAMPLE PREPARATION FOR THE SPECTROSCOPY EXPERIMENTS We prepare hyaluronic acid solutions by dissolving 20 mg high- or low-molecular weight hyaluronan (hyaluronic acid sodium salt from Streptococcus equi, ∼1.5-1.8 MDa, Sigma Aldrich, or sodium hyaluronate, Research grade, 100-150 kDa, Lifecore Biomedical, respectively) in 1 ml solution containing 150 mM sodium

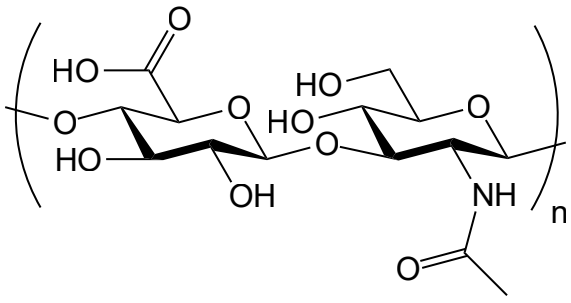

FIGURE 6.1. Molecular structure of hyaluronan.

chloride (NaCl, 99.5%, Sigma Aldrich) and 4% D_2O (99.9%D, Cambridge Isotope laboratories) in H_2O (ultrapure milli-Q grade). We adjust the pH by adding an amount of perchloric acid ($HClO_4$, standard solution 1M, Fluka Sigma Aldrich). Perchloric acid was used because this acid has only a very small contribution to the water signal in the anisotropy experiments. This is due to the fact that the OD groups of HDO molecules hydrogen bonded to the perchlorate anion (ClO_4^-) absorb at a significantly higher frequency ($\sim$2650 cm^{-1}) than the OD groups forming hydrogen bonds to the oxygen atoms of water molecules or hyaluronan ($\sim$2500 cm^{-1}). The samples were mixed using a vortex mixer and left to equilibrate for at least 12 hours, and used for a maximum time of one week, since the samples eventually undergo hydrolytic degradation.

SPECTROSCOPY The pump-probe measurements described in this chapter are performed with the setup described in section 2.2.

SAMPLE PREPARATION FOR THE RHEOLOGY MEASUREMENTS The samples were prepared in a glass vial by first weighing and adding hyaluronic acid sodium salt in powder form (Streptococcus equii, Sigma Aldrich, 1.5-1.8 MDa molecular weight), and subsequently adding water, NaCl (Sigma Aldrich), and HCl (Sigma Aldrich) to achieve different molarities of HCl (ranging from 0-60 mM), 0.15 M NaCl and a final concentration of 10 mg/mL hyaluronic acid. For each sample, the pH was measured using a pH meter (Hanna Instruments). The samples were left to equilibrate at room temperature until they were homogeneous.

RHEOLOGY The rheological properties of the solutions were measured with a stress-controlled rheometer (Anton Paar Physics MCR 501) using a PP40 geometry (parallel plates, 40 mm diameter) at a 100 μm gap and at a temperature of 22°C set by a Peltier system. The elastic and viscous shear moduli were probed by oscillatory shear rheology, with an oscillation frequency of 0.5 Hz and a small strain amplitude of 0.5% to ensure a linear response. At each pH we averaged the results of at least three measurements.

DIFFERENTIAL DYNAMIC MICROSCOPY Differential dynamic microscopy (DDM) measurements were done using probe particles with diameters of 0.6 μm, from Sigma Aldrich (Latex beads, polystyrene). In order to avoid non-specific interactions of the particles with hyaluronan, the particles were passivated with poly(ethylene glycol) chains following an established protocol.[103] The beads were added to the hyaluronan gels in a ratio of 1:100 (v/v) and the samples were vortexed to ensure a homogeneous distribution of the particles. The samples were then placed between two coverslips (Menzel^{TM} Microscope Coverslips 24x60mm, #1, Thermo Scientific) separated by a silicone chamber (Grace Bio-Labs CultureWell^{TM} chambered coverglass, Sigma Aldrich). The samples were imaged in bright field mode on an inverted Ti-Eclipse microscope (Nikon) with a 100x oil immersion objective and a fast camera (Hamamatsu, Orca-Flash 4.0). The samples were imaged at least 10 μm above the surface to avoid non-specific interactions with the glass slides. Videos of 5000 frames were recorded with a frame rate of 100 frames per second

and an exposure time of 10 ms. The measurement was repeated in at least three different portions of the sample.

DIFFERENTIAL DYNAMIC MICROSCOPY ANALYSIS The videos obtained were analysed with a custom written MatLab program. The principle of the techniques were introduced in Ref.[104] The thermal motion of the particles in the viscous medium causes fluctuations of the intensity. The recorded intensity I (x,y,t) is transformed to the Fourier space and the images measured at different lag times Δt can be correlated to obtain the image structure function:

$$D(q, \Delta t) =< |i(q, t + \Delta t) - i(q, t)|^2 > \tag{6.1}$$

where q is the wavevector, which is defined as $q = 2\pi/\lambda$ Next, the intermediate scattering function can be obtained from the image structure function through the formula:

$$D(q, \Delta t) = A(q)[1 - f(q, \Delta t] + B(q) \tag{6.2}$$

Here $A(q)$ is a proportionality factor between the intensity and the correlation fluctuations, while $B(q)$ represents the noise of the camera. By fitting the intermediate scattering function $f(q, \Delta t)$ to a stretched exponential decay $e^{-(\frac{\Delta t}{\tau(q)})^n}$, it is possible to retrieve the diffusion coefficient of the particle $D = 1/(\tau(q)q^2)$. In all of the cases examined, the fit yielded a value of $n = 1$, indicating simple diffusion. We infer the viscosity η of the solution from the generalized Stokes-Einstein relation:

$$D_m = \frac{k_B T}{6\pi\eta a} \tag{6.3}$$

Where a is the particle radius. The viscosities were obtained from correlation functions recorded at a q-value of 7.2 μm^{-1} units, and the values shown are an average over data obtained from three different locations in the sample.

6.3 RESULTS AND DISCUSSION

In Figure 6.2A we show the isotropic transient absorption spectra measured in the frequency region of the O-D stretch vibration of HDO at different pump-probe delay times for a solution of 20 mg/ml high-molecular weight hyaluronic acid and 60 mM $HClO_4$ in isotopically diluted water. The isotropic spectra show a ground-state bleach at short time delays, and a thermal difference spectrum at long time delays. To extract the anisotropy of the excited OD stretch vibration, we subtract the heating contribution by fitting the spectra to a kinetic model which describes the vibrational relaxation and the rise of the heating contribution, as described in chapter 2. The result of this fit is shown as solid lines in Figure 6.2A. Figure 6.2B shows the resulting anisotropy of the OD stretch vibration as function of frequency, for different delay times. These results show that the anisotropy decay is frequency independent.

Figure 6.3 shows the anisotropy decay of solutions of hyaluronan at different $HClO_4$ concentrations in isotopically diluted water. For solutions of

hyaluronan we observe that the anisotropy decay contains an additional slow component. We fit this anisotropy with an exponential decay with an offset, $R = R_0 e^{-t/\tau_r} + R_{slow}$. We find a time constant τ_r of 2.2 ± 0.1 ps for all hyaluronic acid solutions, similar to the reorientation time constant of neat liquid water.[39] This exponentially decaying reorientation component thus represents water molecules for which the reorientation is not influenced by the presence of the hyaluronan polymer chains. The offset R_{slow} is attributed to water molecules for which the reorientation is strongly slowed down due to the interaction with hyaluronan polymer chains or with the other ions present in the solution.[63]

In Figure 6.4 we show the normalized offset, $R_{slow}/(R_{slow}+R_0)$ as a function of $HClO_4$ concentration (red points). We observe a decrease in the normalized offset of hyaluronan solutions with increasing concentration until 44 mM $HClO_4$, followed by an increase in offset until 60 mM $HClO_4$, and then again a decrease in offset. We also measured the anisotropy for a solution only containing ions (no hyaluronan), in order to distinguish between the fraction of slow water molecules resulting from the interaction with hyaluronan and the fraction of slow water molecules resulting from the interaction with the ions. The result of these measurements (solutions of 150 mM NaCl and a varying concentration of $HClO_4$) are also shown in Figure 6.4 (blue). For the solutions that only contain ions, the fraction of slow water molecules increases linearly with the concentration of $HClO_4$. Comparison of the red and blue points shows that at most concentrations the hyaluronan has a much stronger slowing down effect than the ions.

Figure 6.5 shows the anisotropy decay for solutions of low-molecular weight hyaluronan in isotopically diluted water. The data in this figure are analyzed in

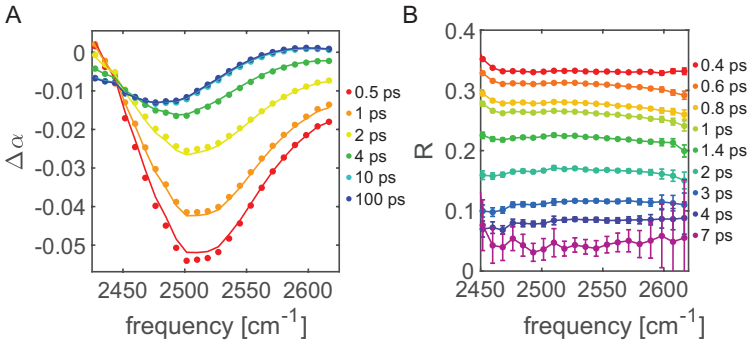

FIGURE 6.2. (A) Isotropic transient absorption change of the OD stretch vibration of HDO molecules for a solution of 20 mg/ml high-molecular weight hyaluronic acid and 60 mM $HClO_4$ in isotopically diluted water, for different picosecond delay times. The solid lines result from a fit to the model described in the text. (B) Anisotropy as a function of frequency for a solution of 20 mg/ml high-molecular weight hyaluronic acid and 60 mM $HClO_4$ in isotopically diluted water, for different picosecond delay times.

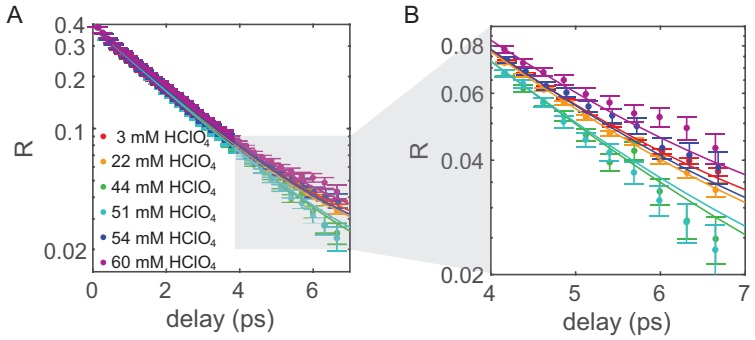

FIGURE 6.3. (A) Anisotropy decay as a function of delay time for solutions with 20 mg/ml high-molecular weight hyaluronan and different $HClO_4$ concentrations in isotopically diluted water, averaged over the frequency range 2450-2550 cm^{-1}. The solid lines are fits to an exponential function with an offset. (B) Zoom-in of the anisotropy decay at delay times >4 ps.

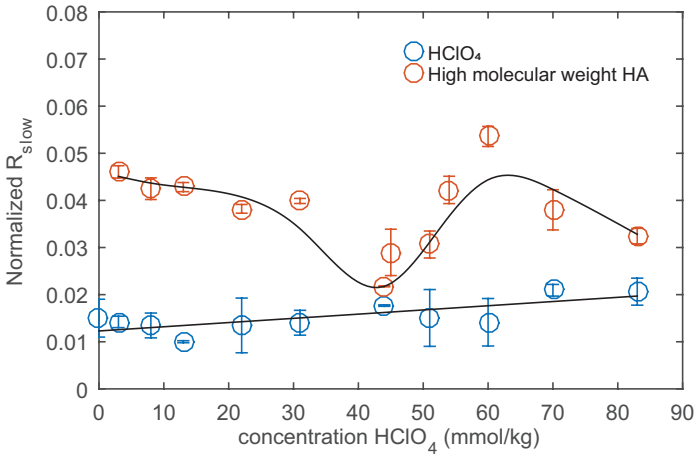

FIGURE 6.4. Normalized offset R_{slow} of the anisotropy decay as a function of $HClO_4$ concentration of solutions containing $HClO_4$, high molecular weight hyaluronan and 150 mM NaCl (red), and only containing $HClO_4$ and 150 mM NaCl (blue). All solutions are in isotopically diluted water. The solid lines are guides to the eye.

the same way as the data in Figure 6.3, i.e. fitted with an exponential decay and an offset. We observe that the offsets behave quite similarly as was observed for high-molecular weight hyaluronan, in spite of the fact that low-molecular weight hyaluronan does not form an elastic putty state near pH 2.4.[105,106] As shown in Figure 6.6, the normalized offset R_{slow} shows a similar dependence on the $HClO_4$ concentration as for high-molecular weight hyaluronan, reaching a minimum at an $HClO_4$ concentration of 54 mM.

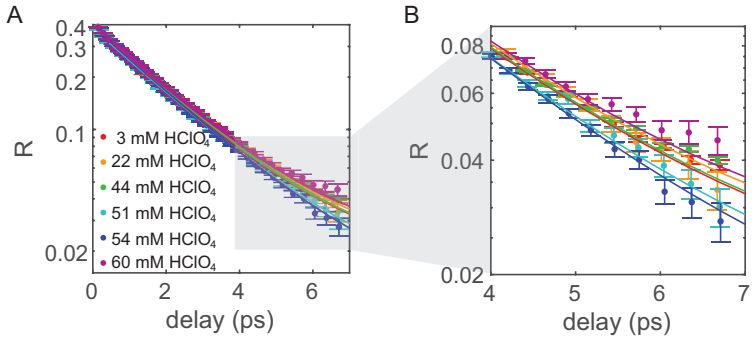

FIGURE 6.5. (A) Anisotropy decay as a function of delay time for solutions of low molecular weight hyaluronan with different $HClO_4$ concentration in isotopically diluted water and neat isotopically diluted water, averaged over the frequency range 2450-2550 cm^{-1}. The solid lines are fits to an exponential function with an offset. (B) Detail of the anisotropy decay.

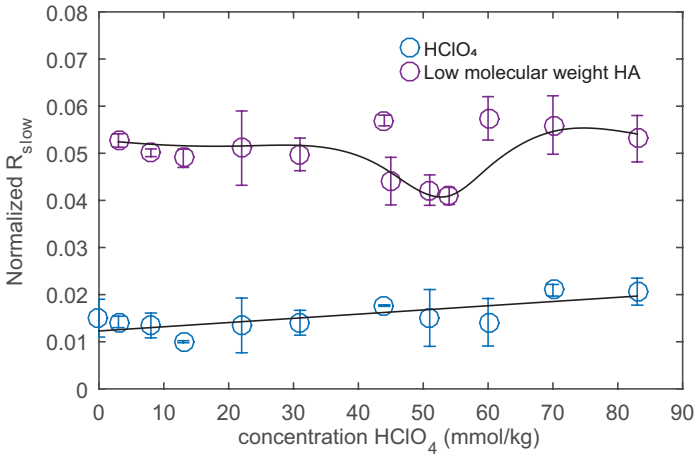

FIGURE 6.6. Normalized offset R_{slow} of the anisotropy decay as a function of $HClO_4$ concentration of solutions containing $HClO_4$, low molecular weight hyaluronan and 150 mM NaCl (red), and only containing $HClO_4$ and 150 mM NaCl (blue). All solutions are in isotopically diluted water. The solid lines are guides to the eye.

The dynamics of the anisotropy of the OD stretch vibration represents the reorientation of the water hydroxyl groups. The value of R_{slow} represents the fraction of water hydroxyl groups that are slowed down due to their interaction with hyaluronan and the ions present in solution. To determine the fraction of water hydroxyl groups that are slowed down because they are bound to hyaluronan, we first corrected the offset R_{slow} for the contribution of water molecules interacting with Na^+, Cl^- , H^+ and ClO_4^- by subtraction. The offset

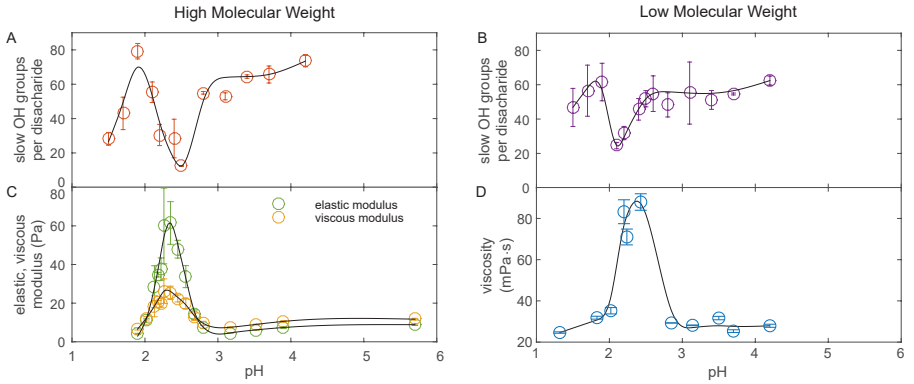

FIGURE 6.7. (A) Number of slow OH groups per disaccharide unit of the high molecular weight hyaluronan polymer as function of pH. (B) Number of slow OH groups per disaccharide unit of the low molecular weight hyaluronan polymer as function of pH. The number of slow OH groups per disaccharide unit is obtained after subtraction of the contribution of water molecules hydrating Na^+, Cl^- and ClO_4^- ions. (C) Elastic (green) and viscous (orange) modulus of 10 mg/ml high molecular weight hyaluronan solutions in water. (D) Viscosity 20 mg/ml of low molecular weight hyaluronan solutions in water. The solid lines are a guide to the eye.

of solutions that do not contain hyaluronic acid, but only NaCl and $HClO_4$, are shown in Figures 6.4 and 6.6. The offset caused by NaCl and $HClO_4$ clearly increases with increasing $HClO_4$ concentration. For a solution without $HClO_4$, the offset is not zero because all solutions contain 150 mM NaCl, contributing to the offset. The data points were fitted with a linear function $y = ax + b$. From the slope of this function we conclude that 10 ± 3 OH groups per ClO_4^- ion are slowed down, and from the offset it follows that 9 ± 1 OH groups are slowed down by an Na^+ ion plus a Cl^- ion. After subtracting these contributions, we calculated the number of slowly reorienting water hydroxyl groups N_{slow} per disaccharide unit of the hyaluronan polymer using the following expression:

$$N_{slow} = \frac{R_{slow}/(R_{slow} + R_0)}{c} \cdot 110.514 \tag{6.4}$$

where c represents the molar concentration of disaccharide units, and 110.5 is the number of moles of water hydroxyl groups contained in 1 liter. The resulting numbers of slowly reorienting hydroxyl groups per disaccharide unit of the hyaluronan chain are reported in Figure 6.7A and B for low and high molecular weight hyaluronan, respectively.

For the low-molecular weight variant, we observe an increase of the number of slow OH groups per disaccharide unit when the pH is increased up to pH 1.9. Then the number of slow OH groups sharply decreases, from 61 ± 10 at pH 1.9 to 25 ± 2 at pH=2.1. When the pH is further increased to 3, the number of slow groups increases again to 55 ± 12, and stays more or less constant when the pH is further increased. For high-molecular weight hyaluronan, we observe

28 ± 4 slow water OH groups per disaccharide unit at pH 1.5. This number increases with increasing pH to 79 ± 5 slow OH groups at pH 1.9. After pH 1.9, the number of slow OH groups sharply decreases, to a minimum of 12 ± 1 OH groups at pH 2.5. When the pH is further increased, the number of slow OH groups increases again.

In Figure 6.7C we show the viscous and elastic shear moduli of the high-molecular weight hyaluronan solution (10 mg/ml) as a function of the pH. At pH 2.4, a sharp increase in the elastic and viscous modulus is observed, reflecting the formation of the putty state. This finding agrees with previously reported rheology measurements.[99] For low-molecular weight hyaluronan, the rheological differences were too small to measure using conventional rheology as the molecular weight is too small for the chains to entangle and to form an elastic putty state. Therefore, we determined the viscosity of solutions of 20 mg/ml low molecular weight hyaluronan with differential dynamic microscopy (DDM) (Figure 6.7D).[107–109] For low-molecular weight hyaluronan we also observe a sharp increase of the viscosity around pH 2.4.

Figure 6.7 shows that there exists a strong correlation of the macroscopic rheology and the changes in water dynamics probed by polarization-resolved pump-probe spectroscopy. The pH values at which we observe minima in the number of slow OH groups differ by less than 0.2 units from the pH values at which we observe the maxima in the viscosity. We thus arrive at the counterintuitive result that the strong increase in viscosity near pH 2.4 of aqueous hyaluronan solutions correlates to a substantial decrease of the fraction of slow water, i.e. an increase of the average orientational mobility of the water molecules. This change in interaction between water and hyaluronan is not visible from the pH dependent FTIR spectra of hyaluronic acid[102], which can be explained from the fact that the hydrogen bonds that are formed by water molecules in the hydration shell of hyaluronic acid are similar in strength and number as the hydrogen bonds that are formed between water molecules in bulk liquid water. The change in local environment from hydration shell to bulk thus has little effect on the vibrational spectrum of the water molecules but obviously a strong effect on the orientational mobility. Femtosecond nonlinear infrared spectroscopy has as a unique capability that it can probe this change in molecular orientational mobility.

The observed reduction in number of slowed-down water implies that $\sim 80\%$ of the water molecules are being expelled from the polymer surfaces near pH 2.4. We ascribe this expulsion to the bundling of the polymer chains into fibres. Other research also suggests that the polymer chains bundle into fibres in the formation of the putty state.[102,110–113] The expulsion of water molecules during the formation of a connected network of fibers accounts both for the macroscopic observation of increased viscosity, and the molecular-scale observation of a decrease in slow water molecules interacting with the hyaluronic acid molecules. Interestingly, we observe the expulsion of water not only for high molecular weight hyaluronan, but also for low molecular weight hyaluronan that does not form a putty state.[105,106] This finding suggests that low-molecular weight hyaluronic polymer chains also form strong interchain connections near pH 2.4.

However, in this case the polymer chains are not long enough to form a macroscopically connected network. As a result, low-molecular weight hyaluronan does not form an elastic putty state.

As shown in Figure 6.7, the number of slowly reorienting water hydroxyl groups also decreases when the pH is decreased from pH 1.9 to pH 1.5, both for high molecular weight and low molecular weight hyaluronan solutions. Lalevée and co-workers showed, using light scattering techniques, that at these very low pH values, the radius of gyration of hyaluronan decreases indicating a chain collapse.[114] Hence, also at these pH values water molecules get expelled, but not because of the formation of interchain connections (chain bundling) but because of the curling up of the individual hyaluronan chains.[102]

In an earlier femtosecond mid-infrared study by Hunger et al. of the properties of the solution state of hyaluronan at pH 7, it was found that 15 ± 3 water molecules per disaccharide are affected in their reorientation dynamics.[115] This number is approximately 2 times smaller than the number of slow water molecules that we observe at pH 7. An important difference with this previous work is that we study solutions with a relatively low concentration of hyaluronan (20 mg/ml), while the measurements of Hunger et al. involved concentrations up to 200 mg/ml. At these high concentrations, saturation effects due to aggregation and sharing of hydration shells will occur, leading to a substantially lower number of slowed-down water molecules per hyaluronan disaccharide unit. In another femtosecond mid-infrared study the hydration numbers of several monomeric sugar molecules were determined. In this study, a hydration number of 46 ± 5 was found for the disaccharide trehalose.[116] This number is higher than the number of slowly reorienting waters of 33 ± 5 (or 67 ± 10 slow OH groups) per disaccharide unit that we find here for high-molecular weight hyaluronan in the solution state. This difference can be well explained from the fact that the disaccharide units of the hyaluronan polymer chains are in close proximity to each other, and that these chains will be somewhat folded, thus reducing the net amount of hydrating water molecules per disaccharide unit.

6.4 Conclusions

We studied the relation between the viscoelastic properties and the reorientation dynamics of water molecules for aqueous solutions of high-molecular weight and low-molecular weight hyaluronan. The viscoelastic properties are determined with rheology and differential dynamic microscopy (DDM), the water reorientation dynamics with polarization-resolved femtosecond mid-infrared pump-probe spectroscopy. We observe that the interaction between water and hyaluronan leads to a slowing down of the reorientation of a significant fraction of the water molecules.

We find both the viscosity and the reorientation dynamics to be strongly dependent on pH. For both low-and high-molecular weight hyaluronan the viscosity reaches a maximum near pH 2.4, while the number of slowed-down water molecules reaches a minimum. This finding implies that the water molecules

show faster average reorientation dynamics when the solution is more viscous. This observation can be explained from the fact that around pH 2.4 hyaluronan the polymer chains bundle to form fibres, accompanied by expulsion of hydration water from the polymer chains.

For high-molecular weight hyaluronan, the expulsion of water and the bundling into fibers results in the formation of an elastic putty state. The reduction in number of slowed-down water shows that ∼80% of the water molecules are being expelled from the polymer surfaces in the formation of this state. For low-molecular weight the putty state is not observed. However, the molecular water reorientation dynamics show that the molecular-scale interactions between low-molecular weight hyaluronan and the water solvent are highly similar to those of high-molecular weight hyaluronan. For low-molecular weight hyaluronan likely no putty state is formed because the fibers formed near pH 2.4 are too short to form a macroscopically connected network. These results illustrate that the molecular-scale water dynamics can provide important additional information on the mechanism of macroscopic gelation in biopolymer solutions.

7 Structure and dynamics of a temperature sensitive hydrogel

Polyisocyanotripeptides (TriPIC) are biomimetic polymers which consist of a β-helical backbone stabilized by hydrogen bonds between amide groups. Their polyethylene glycol side chains give TriPIC aqueous solutions a thermoresponsive behavior: at 50°C the solution becomes a hydrogel. In this chapter we study the molecular structure and water dynamics of TriPIC aqueous solutions while undergoing gelation, using FT-IR spectroscopy and polarization-resolved femtosecond infrared spectroscopy (fs-IR). We find evidence that the polyethylene glycol side chains trap part of the water molecules upon gel formation, and we propose that the interaction between the polyethylene glycol side chains and water plays an essential role in the bundling of the polymers and thus in the formation of a hydrogel. We observe that the helical backbone and the amide groups closest to this backbone form a hydrophobic core that is inaccessible to water, and that stays inaccessible when the solution is heated above the gelation temperature.

7.1 Introduction

Many biological gels consist of polymers which assemble in a helical structure, which give them stiffness and stability.[117,118] These biological hydrogels often show a special mechanical responsiveness that plays an essential role in cellular processes.[119–121] It is interesting to mimic biological hydrogels with gels based on synthetic polymers, as these synthetic gels will find many applications.[122,123] Rowan and coworkers developed a biomimetic hydrogel, based on polyisocyanopeptides (PICs), which not only possesses a similar mechanical responsiveness as many biological gels, but also shows thermoresponsive behaviour.[124] PICs consist of a helical backbone that is responsible for the gel stiffness and that can be chemically modified to add a targeted functionality to the polymer. PICs adopt a 4_1 β-helical conformation (four repeating units per turn). This conformation is stabilized by a β-sheet-like hydrogen-bond network between the amide groups of monomers n and $n+4$.[125,126] When the polyisocyanidepeptides are grafted with ethylene glycol side chains, they exhibit a thermoresponsive behavior that causes the polymer to form a gel at elevated temperatures.[124,127] These synthetic gels have been shown to form a network of semiflexible bundles and to truly mimic biological gels and. These gels have been studied with several microscopy techniques, small-angle X-ray scattering, and rheology measurements. Nevertheless, the molecular mechanism of the gelation process of PICs remains largely unknown.[127,128]

In order to fully understand the gelation process of PICs, and to be able to design other biomimetic hydrogels, it is essential to fully understand their molecular structure and intermolecular interactions. Here we study solutions of the polymer TriPIC that consists of a helical PIC backbone and three adjacent alanine groups (see Figure 7.1). The stiff, helical backbone of the TriPIC polymer chain is stabilized by two parallel hydrogen-bonding arrays between the amide groups, which provide the polymer with thermal stability, while the ethylene glycol tails provide TriPIC with a thermoresponsive functionality, resulting in gelation at 50°C. Using FT-IR, we study the molecular structure of the polymer below and above the gelation temperature. Using polarization-resolved femtosecond infrared spectroscopy, we study the dynamics of the water molecules in TriPIC polymer solutions, and how these dynamics change when the temperature is increased above the gelation temperature.

7.2 Experimental Methods

Sample preparation The samples measured with FT-IR spectroscopy were prepared by dissolving monomer or polymer TriPIC in D_2O and by stirring the solution for 24 hours in a cold room at 4°C under N_2 atmosphere.

The monomer and TriPIC polymer solutions for polarization-resolved femtosecond infrared spectroscopic studies were prepared by dissolving the monomer or polymer in 4% D_2O (99.9%D, Cambridge Isotope Laboratories) in H_2O (ultrapure milli-Q grade) and by stirring the solution for 24 hours at 4°C.

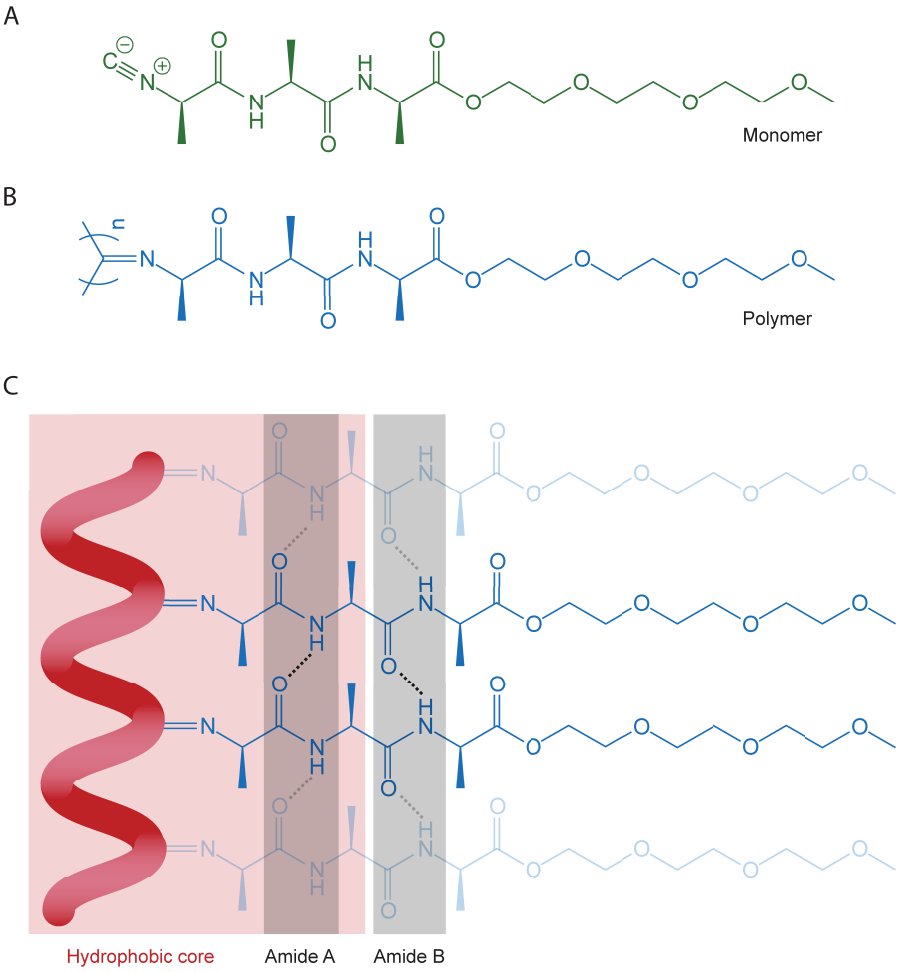

Figure 7.1. (A) Molecular structure of the TriPIC monomer. (B) Molecular structure of the TriPIC polymer. (C) Cartoon of the β-helical structure of TriPIC and the hydrogen-bonded network between the amide groups.

Linear and nonlinear spectroscopic measurements The pump-probe measurements described in this chapter are performed with the setup described in section 2.2. The FT-IR spectra are measured with a Bruker Vertex 80v FT-IR spectrometer.

7.3 Results and Discussion

7.3.1 FT-IR spectroscopy

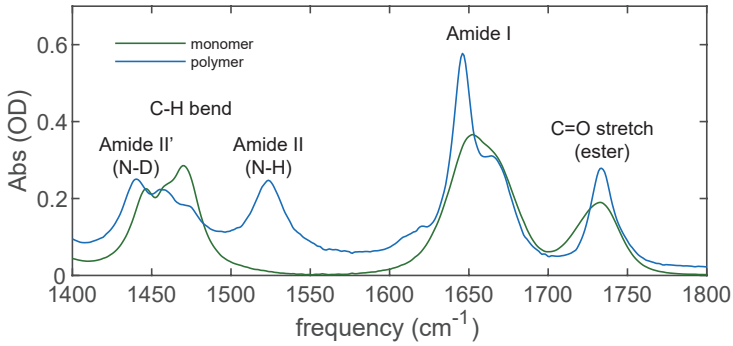

FIGURE 7.2. FT-IR spectra of TriPIC polymer (blue) and the corresponding monomer (green) solutions of 17 mg/ml in D_2O at room temperature. The peak assignments are discussed in the text.

SOLVENT ACCESSIBILITY The helical backbone conformation of TriPIC is stabilized by hydrogen-bonding arrays, and as such, water is expected to have a significant impact on the stability and the rigidity of the helix. We used H/D exchange experiments in conjunction with FT-IR and ATR spectroscopy to study the solvent accessibility of the helical backbone. Figure 7.2 shows the FT-IR spectrum of a TriPIC polymer solution, together with that of a TrPIC monomer solution, both using D_2O as the solvent. The absorption band at 1735 cm^{-1} is due to the ester C=O stretching vibration, and the band at 1645 cm^{-1} corresponds to the amide I modes of the two amide groups. This latter band is much narrower for the polymer than for the monomer solution, while the area under the band is more or less the same. The large width of the absorption band of the amide I mode of the monomer indicates that the amide groups form hydrogen bonds with water molecules, as these hydrogen bonds show a large variation in strength, leading to a broad absorption band. In the polymer the amide A groups form mutual intrachain hydrogen bonds (see Figure 7.1C), with a much smaller distribution in hydrogen-bond strengths, thus leading to a much narrower absorption band. The low-frequency shoulder at 1620 cm^{-1} (which is only observed for the polymer) is attributed to the C=N stretch vibration. Interestingly, we also observe a strong amide II (which has mainly NH-bending character) absorption band at 1523 cm^{-1} for the polymer, which is entirely absent in the monomer spectrum. This band points to the persistent presence of protonated NH groups in the polymer, even though the polymer is dissolved in D_2O. These NH groups are apparently extremely well shielded from the solvent because they show no sign of H/D exchange, even after keeping the polymer for several weeks in D_2O solution.

In order to test whether all NH groups in the polymer are inaccessible to the solvent, we also measured ATR spectra for a 1:1 mixture of D_2O:H_2O (Figure 7.3B). We find that the amide II band (1523 cm^{-1}) increases in intensity when H_2O is added to the solvent, and that the band at 1440 cm^{-1} (due to the

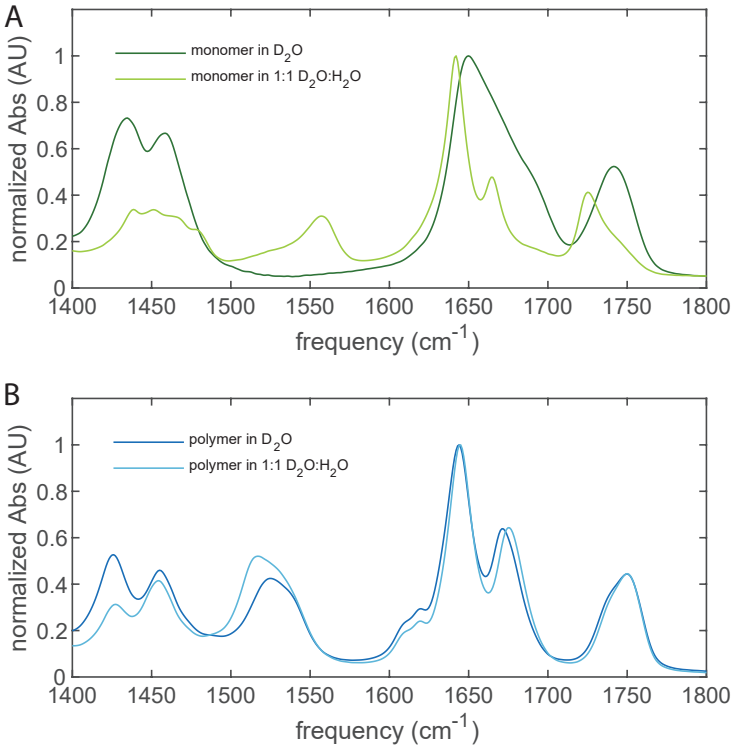

FIGURE 7.3. (A) ATR spectra of monomer solutions in D_2O (dark green) and in a mixture of 1:1 D_2O:H_2O (light green) at room temperature. (B) ATR spectra of TriPIC polymer solutions in D_2O (dark blue) and in a mixture of 1:1 D_2O:H_2O (light blue) at room temperature.

amide II' absorption of deuterated amide groups) decreases in intensity. This indicates that the polymer contains not only solvent-inaccessible NH groups but also solvent-accessible NH groups. The ATR spectra also show two well-resolved bands in the amide I region (at 1645 and 1671 cm^{-1}). The band at 1671 cm^{-1} blue-shifts a few cm^{-1} when H_2O is added to the solvent, whereas the band at 1645 cm^{-1} is unaffected. This leads us to conclude that the two amide I absorption bands correspond to the two types of helical amide groups (A and B): the amide groups closest to the helical backbone (A) absorb at 1645 cm^{-1} and are solvent inaccessible, whereas the amide groups further away from the central helix (B) and close to the poly(ethylene glycol) chain, absorb at 1671 cm^{-1} inD_2O, and are accessible to the solvent, as evidenced by the small blue shift upon the addition of H_2O. For the monomer, we observe complete H/D exchange. When the monomer is dissolved in D_2O, there is no amide II (NH bending) band present, and we only observe the amide II' (ND bending) band at 1434 cm^{-1}. When the solvent is exchanged for a 1:1 D_2O:H_2O mixture, the amide II band is observed at 1558 cm^{-1}, and the amide II' band decreases in

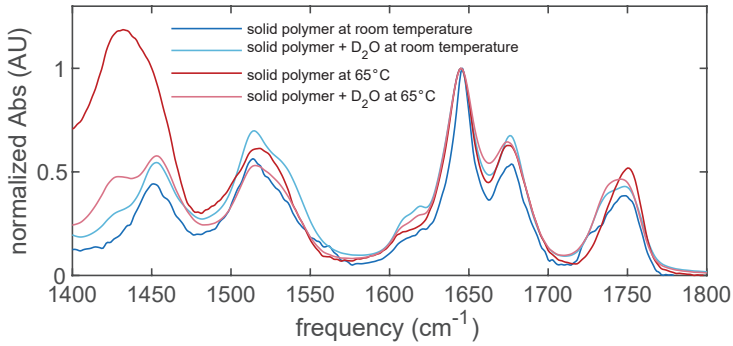

FIGURE 7.4. ATR spectra at room temperature of solid TriPIC polymer (dark blue) and solid TriPIC polymer with a drop of D_2O (light blue), and ATR spectra at 65°C of solid TriPIC polymer (red) and solid TriPIC polymer with a drop of D_2O (pink).

intensity. This shows that for the monomer, all the amide groups are solvent accessible and undergo H/D exchange when H_2O as a solvent is exchanged for D_2O.

To investigate whether the solvent accessibility of the TriPIC polymer is temperature-dependent, we also performed H/D exchange experiments at a temperature above gelation temperature (T_{gel} = 50°C), at 65°C. Figure 7.4 shows the results of this experiment. In this case, we start the experiment with a solid TriPIC polymer sample. The solid sample will be completely protonated since the molecule was synthesized under protonated conditions. In both spectra of the solid sample, at room temperature and at 65°C, we observe the amide II band and no amide II' band. After a drop of D_2O has been added to the solid sample, the spectrum shows a shoulder at 1428 cm^{-1} (the amide II' band) both at room temperature and at 65°C. In addition, the amide II band remains present, meaning that at both temperatures, the amide closest to the helical backbone (amide A) is solvent inaccessible.

TEMPERATURE DEPENDENCE To obtain more insight into the mechanism of the bundling of TriPIC polymers, we performed temperature-dependent FT-IR measurements (Figure 7.5) of the vibrations of the two hydrogen-bond-forming amide groups. It has been suggested that the hydrogen bonds formed by the amide group closest to the isocyanide backbone (amide A) maintain the helical architecture of the polymer,[129] while the hydrogen bonds of the second amide group (amide B) further stabilize and stiffen the TriPIC polymer backbone. This view is consistent with the present results regarding the different solvent accessibilities of these two amide groups. The intensities, peak widths, and peak centers of the C=O stretch vibrations of both amides and the ester (Figure 7.5B) change with temperature, which indicates that the local chemical environment of these groups changes. For the monomer (Figure 7.5A) we observe no changes in the spectrum in this region as a function of temperature.

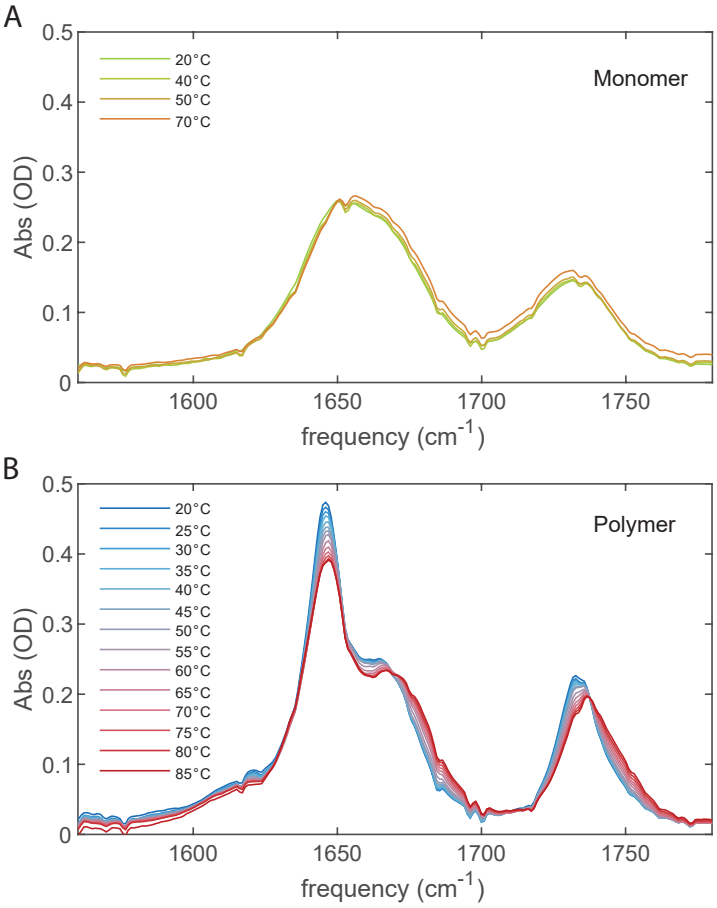

FIGURE 7.5. (A) FT-IR spectra of monomer solutions of 17 mg/ml in D_2O as a function of temperature. (B) FT-IR spectra of TriPIC polymer solutions of 17 mg/ml in D_2O as a function of temperature.

The ester C=O and the amide I,B vibrational bands show a blue-shift with increasing temperature, while the center position of the amide I,A band is independent of temperature. The ester C=O groups and part of the amide I,B groups are hydrogen-bonded to their aqueous solvation shell, and these hydrogen-bonds become weaker with increasing temperature, leading to the observed blue-shift and peak broadening of the amide I,B and ester bands. The amide A hydrogen-bond strength does not change: these groups are already so tightly bound and shielded from the solvent that polymer bundling does not alter their already highly ordered conformation. We note that the spectral changes with the temperature of the aqueous TriPIC polymer solution or gel are fully reversible: on cooling, the original spectrum is obtained again. To analyze the data more quantitatively, the spectra were deconvoluted by globally

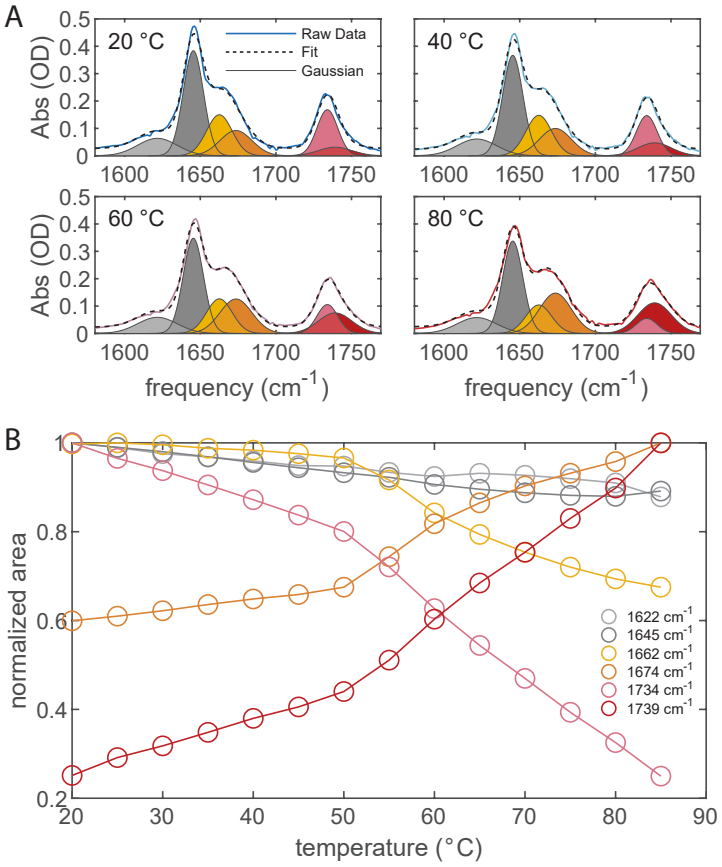

Figure 7.6. (A) Fitted FT-IR spectra of TriPIC polymer solutions of 17 mg/ml in D_2O at different temperatures. The raw spectra (solid line) in the amide I and ester regions were fitted with six Gaussian curves (colored curves) centered at 1622, 1645, 1662, 1674, 1734 and 1739 cm^{-1}. The fit result is show as dashed black line. (B) Normalized area of the fitted Gaussians as a function of temperature. The solid lines are guides to the eye.

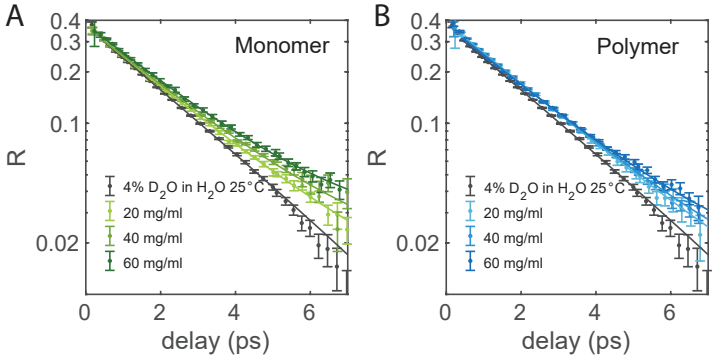

Figure 7.7. (A) Anisotropy decay as a function of delay time of monomer solutions in isotopically diluted water, for different concentrations at room temperature. (B) Anisotropy decay as a function of delay time of TriPIC polymer solutions in isotopically diluted water, for different concentrations at room temperature. The solid lines are fits to an exponential function with an offset.

fitting six Gaussian peaks with peak centers at 1622, 1645, 1662, 1674, 1734, and 1739 cm^{-1}. We fitted the C=N band and the amide I,A band each with one Gaussian, and the amide I,B band and the ester vibrational band each with two Gaussians, as this allows us to model the blue-shift and broadening of these latter two bands with increasing temperature. In Figure 7.6A we show this fit for four different temperatures from 20°C to 80°C. The dashed line shows that the model with six Gaussian curves provides a good fit of the experimental spectrum at all temperatures. The areas of the Gaussians are shown in Figure 7.6B. For the Gaussians fitting C=N stretch mode and the amide I,A mode the area stays constant as a function of temperature. For the Gaussians fitting the amide I,B mode and the C=O stretch mode, we observe that there is an inflection point at $T_{gel} = 50°C$, above which the variation of the intensity of the bands with temperature becomes stronger.

7.3.2 Pump Probe Spectroscopy

Concentration dependence We also studied the dynamics of the solvent of aqueous TriPIC polymer solutions with polarization-resolved femtosecond infrared spectroscopy. In this technique we pump and probe the OD stretch vibration of HDO molecules in isotopically diluted water. By measuring the anisotropy decay of the transient absorption signal of the excited OD stretch vibrations, we obtain information on the orientational mobility of the water hydroxyl groups. In Figure 7.7, we show the anisotropy decay of the OD stretch vibration of HDO measured for pure isotopically diluted water and for TriPIC monomer and polymer solutions at different concentrations. For pure isotopically diluted water, we find that the anisotropy decay can be fitted well with an exponential function with a (reorientation) time constant of 2.3 ps. For so-

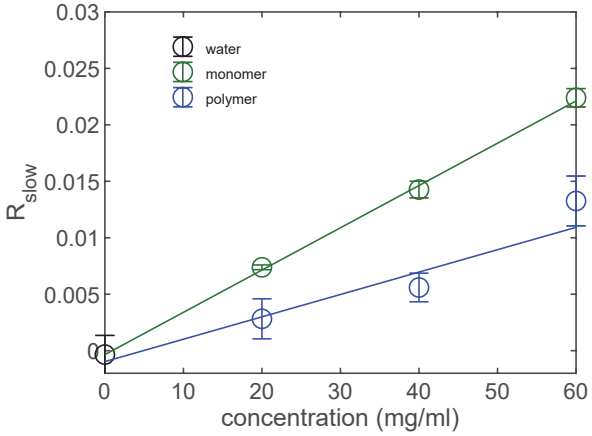

FIGURE 7.8. Offset R_{slow} of the anisotropy decay as a function of concentration for the monomer (green) and TriPIC polymer (blue), and isotopically diluted water (grey) at room temperature. The solid lines are fits to a linear function.

lutions of TriPIC monomer or polymer, we observe a similar exponential decay and an additional much slower component. We thus fit the anisotropy decay of the TriPIC monomer and polymer solutions with an exponential function with an offset, $R = R_0 e^{-t/\tau_r} + R_{slow}$. We find for all TriPIC monomer and polymer solutions a reorientation time τ_r of 2.4 ps, similar to the reorientation time of isotopically diluted water. This finding indicates that a large fraction of the water molecules in TriPIC monomer and polymer solutions is behaving like bulk water, and only a small fraction of the water molecules reorients on a much longer timescale. In Figure 7.8 we plotted the offset R_{slow} as a function of solute concentration (c_{solute}) for both the TriPIC monomer and the polymer and that R_{slow} is bigger for the monomer than for the polymer. The clear linear dependence of R_{slow} indicates that the slowly reorienting water hydroxyl groups are associated with water molecules that are in the direct vicinity of the solute. These water molecules likely interact with the hydrophobic groups or the polyethylene glycol tails of the monomer and TriPIC polymer.[40,130]

From the slope a of the linear fit ($R_{slow} = a \cdot c_{solute} + b$) we calculate the number of slowly reorienting water molecules per monomer molecule (for the monomer solutions) or repeating unit (for the polymer solutions), N_{slow}. We multiply the slope a by the molecular weight M_w of the TriPIC repeating unit (to change the units from mg/ml to molal) and we divide by 0.4 (to normalize the number, because 0.4 is the maximum value of the anisotropy parameter, i.e. the value of R_{slow} if all water hydroxyl groups would be slow), and multiply the result with the number of moles of hydroxyl groups in a kilogram of water (110.514 for 4% D_2O in H_2O):

$$N_{slow} = \frac{a \cdot M_w}{0.4} \cdot 110.514 \tag{7.1}$$

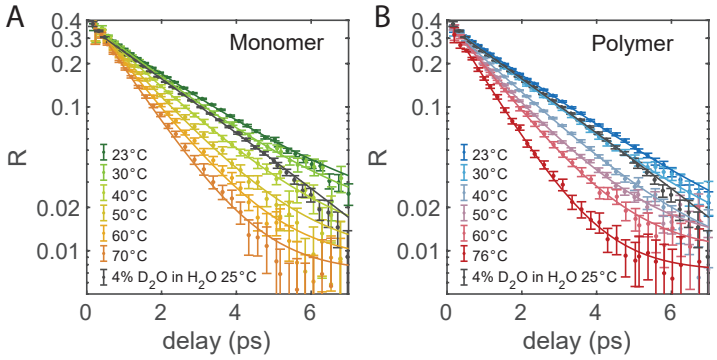

Figure 7.9. (A) Anisotropy decay as a function of delay time of 40 mg/ml monomer solutions in isotopically diluted water, for different temperatures. (B) Anisotropy decay as a function of delay time of 40 mg/ml TriPIC polymer solutions in isotopically diluted water, for different temperatures. The solid lines are fits to an exponential function with an offset.

We find that the monomer slows down 40 ± 2 water hydroxyl groups per molecule while the polymer slows down 21 ± 3 water hydroxyl groups per repeating unit. The difference between the amount of slowly reorienting water hydroxyl groups between the monomer and polymer can be explained by the conformation of the adapts. As we showed with our FT-IR results, for the polymer, the inner amide, amide A, is not accessible for the solvent, meaning that the water molecules are not interacting with the inner core of the polymer. The monomer is completely water accessible, and thus water is interacting with the complete monomer molecule. As more water molecules are interacting with the monomer than with the polymer, the number of affected (slowed-down) water molecules will be larger for the monomer. Interestingly, the difference in solvent-accessibility cannot fully explain the difference of $\sim$20 slowly rotating water OH groups. In previous work it was found that one CH bond slows down the rotation of on average 1.25 water OH groups.[40] Upon polymer formation, 8 CH groups become solvent inaccessible, which is thus expected to lead to a decrease of the number of slowly reorienting water OH groups by $\sim$10. Recently, Ensing et al. showed that polyethylene glycol molecules slow down the reorientation of water molecules not only because of the interaction of water molecules with the hydrophobic groups, but also because of the strong interactions of water with the partially charged polyethylene glycol oxygen atoms. The polyethylene glycol chains are likely much better exposed to the water solvent more solvent for the TriPIC monomers than for the polymer, thus explaining why the difference in number of slow water hydroxyl groups between monomer and polymer is larger than can be explained from the exclusion of water from the core of the polymer.

Temperature dependence To investigate the relationship between the gelation and the water dynamics, we measure the water reorientation dynamics as a function of temperature for both the TriPIC monomer and the polymer

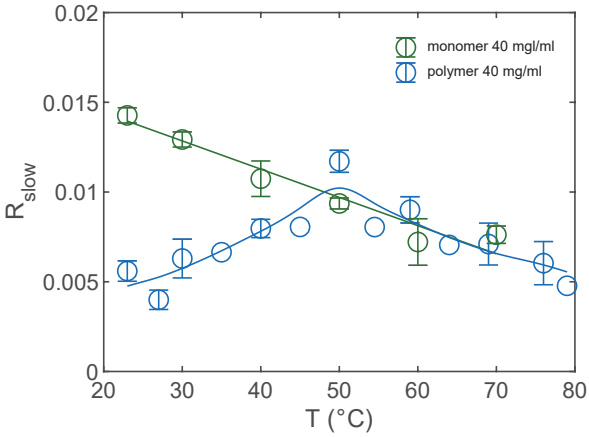

FIGURE 7.10. Offset R_{slow} of the anisotropy decay as a function of temperature for the monomer (green) and TriPIC polymer (blue) at 40 mg/ml. The solid lines are guides to the eye.

solutions. The anisotropic decays are displayed in Figure 7.9. In both cases, the reorientation time becomes faster with increasing temperature. This decrease in reorientation time is also observed for pure isotopically diluted water.[48] To analyze the data, we fitted the reorientation time constants measured for pure isotopically diluted water at different temperatures with an Arrhenius expression. The temperature-dependent reorientation times resulting from this fitted Arrhenius expression were then used as the exponential time constants in fits of the measured anisotropy decays of the TriPIC monomer and polymer solutions. We thus fit these anisotropy decays with an exponential function plus an offset, like we did for the concentration-dependent measurements at room temperature. The results of these fits are presented as the solid lines in Figure 7.9, and the offset R_{slow} that we obtain from this fit is plotted in Figure 7.10.

In Figure 7.10, we show the offset R_{slow} as a function of temperature for both the TriPIC monomer and polymer. For the monomer, we observe a decrease of R_{slow} with increasing temperature. This is in quantitative agreement with previous work, where R_{slow} was measured for proteins at different temperatures[85] within a similar concentration range. Previous dielectric relaxation measurements and NMR experiments on small amphiphilic molecules also showed a similar decrease in slowly reorienting water molecules with increased temperature.[65,131] The amount of slowly reorienting hydroxyl groups decreases with increasing temperature, because of the hydrogen-bond network becomes more dynamic and less coordinated at higher temperatures.[65] For the polymer, we observe a very different behavior. At temperatures below the gelation temperature of 50°C, R_{slow} increases with increasing temperature, until a maximum R_{slow} at 50°C is reached after which the offset decreases. The difference in temperature dependence between the monomer and the polymer is striking, and the

fact that the turning point for the polymer occurs at the gelation temperature, suggests that for the polymer the change in water dynamics with temperature is correlated to the gelation of the TriPIC polymer solution.

It should be noted that the increase in slowly reorienting water molecules below 50°C cannot be attributed to an increase of the solvent accessibility with increasing temperature. Our FT-IR results at different temperatures clearly show that the solvent accessibility does not change significantly upon heating of the solution. More specifically, in Figure 7.4, we see that the amide II band, dominated by the NH bending vibration, stays present in D_2O solvent, at temperatures of 65°C, above the gelation temperature. We thus attribute the increase of the fraction of slowly reorienting water hydroxyl groups from the binding of water molecules between the polyethylene glycol side chains of different polymers. We propose that the trapping of water molecules between the negatively charged oxygen atoms of polyethylene glycol side chains of different polymers plays a crucial role in the bundling of the polymers. In this picture the water molecules act as a glue that binds polymers together to form bundles and a polymer network, which ultimately at 50°C leads to hydrogel formation. For TriPIC monomers, the polyethylene glycol chains are already quite strongly exposed to water at room temperature, and changing the temperature does not lead to a strong change of this interaction.

At temperatures >50°C the fraction of slow water molecules is similar for the TriPIC polymer and the monomer. For TriPIC polymers, water is excluded from the core, leading to a smaller number of water molecules that is slowed down by the central part of the molecule, but apparently at temperatures >50°C, this lower number is fully compensated by the higher number of water molecules that are slowed down as a result of their trapping between the polyethylene glycol chains in the polymer bundles, probably because within these bundles water molecules can easily bind to two ether oxygen atoms simultaneously, which leads to a strong slowing down of their reorientation.[130]

The increase of the slow water fraction upon gelation of TriPIC polymers forms an interesting contrast with the observations in our recent study of the effect of gelation on the slow water fraction in hyaluronic acid hydrogels. For aqueous solutions of hyaluronic acid (which forms a hydrogel at pH 2.5), we showed that the slow fraction is decreasing upon gelation. The disparity between the observations for these two hydrogels can be explained from the different interactions that govern their molecular structure. In the case of hyaluronic acid, the network formation that leads to the formation of the hydrogel is the result of direct hydrogen bonds between the carboxylate groups and the amide groups of the hyaluronic acid molecules.[102] In TriPIC polymers, the polymer molecules are probably crosslinked by hydrogen bonds to bridging water molecules. As these water molecules will show a very slow reorientation, TriPIC gel formation is accompanied by an increase of the slow water fraction.

7.4 Conclusions

In summary, we studied the molecular structure and water reorientation dynamics of TriPIC monomer and polymer solutions with FT-IR H/D isotope exchange experiments, and with temperature-dependent FT-IR and polarization-resolved femtosecond infrared spectroscopy. Our FT-IR H/D exchange experiments show that the NH groups of the inner amide groups of the central helix of TriPIC polymers do not change to ND upon solvation in D_2O. From our femtosecond infrared measurements, we find that the TriPIC polymer is interacting less with water than the monomer. We thus conclude that the TriPIC polymer possesses a hydrophobic core that is partly shielded from water. When the temperature is increased, this hydrophobic core stays shielded from water.

With increasing temperature, the fraction of water molecules that are slowed down by the TriPIC polymers increases, opposite to what is observed for the monomer and for other solute molecules in water. We explain this increase from the enhanced binding of water molecules to the polyethylene glycol side chains. We propose that this binding, in particular the donation of two strong hydrogen bonds by a water molecule to two negatively charged oxygen atoms of polyethylene glycol side chains that belong to different polymers, may play a role in the bundling of the polymers. The water molecules thus may act as a glue that bind the polymers together, leading to an extended polymer network, and eventually to the formation of a hydrogel.

At the gelation temperature of 50°C, the number of trapped water molecules saturates. When the temperature is increased above the gelation temperature, the temperature dependence of the number of slowed-down water molecule becomes normal, i.e. slowly decreases with increasing temperature, as is observed for the monomer.

Bibliography

1. P. Ball, "Water−an enduring mystery," *Nature*, vol. 452, no. 7185, pp. 291–292, 2008.

2. P. Ball, "Water as an active constituent in cell biology," *Chemical reviews*, vol. 108, no. 1, pp. 74–108, 2008.

3. K. N. Houk, M. N. Paddon-Row, N. G. Rondan, Y.-D. Wu, F. K. Brown, D. C. Spellmeyer, J. T. Metz, Y. Li, and R. J. Loncharich, "Theory and modeling of stereoselective organic reactions," *Science*, vol. 231, no. 4742, pp. 1108–1117, 1986.

4. K. N. Houk and P. H.-Y. Cheong, "Computational prediction of small-molecule catalysts," *Nature*, vol. 455, no. 7211, pp. 309–313, 2008.

5. K. Jackson, S. K. Jaffar, and R. S. Paton, "Computational organic chemistry," *Annual Reports Section" B"(Organic Chemistry)*, vol. 109, pp. 235–255, 2013.

6. Q. Peng, F. Duarte, and R. S. Paton, "Computing organic stereoselectivity–from concepts to quantitative calculations and predictions," *Chemical Society Reviews*, vol. 45, no. 22, pp. 6093–6107, 2016.

7. F. M. Bickelhaupt and K. N. Houk, "Analyzing reaction rates with the distortion/interaction-activation strain model," *Angewandte Chemie International Edition*, vol. 56, no. 34, pp. 10070–10086, 2017.

8. T. Hansen, L. Lebedel, W. A. Remmerswaal, S. van Der Vorm, D. P. Wander, M. Somers, H. S. Overkleeft, D. V. Filippov, J. Désiré, A. Mingot, *et al.*, "Defining the sn1 side of glycosylation reactions: stereoselectivity of glycopyranosyl cations," *ACS central science*, vol. 5, no. 5, pp. 781–788, 2019.

9. B. Guillot, "A reappraisal of what we have learnt during three decades of computer simulations on water," *Journal of molecular liquids*, vol. 101, no. 1-3, pp. 219–260, 2002.

10. M. Ceriotti, W. Fang, P. G. Kusalik, R. H. McKenzie, A. Michaelides, M. A. Morales, and T. E. Markland, "Nuclear quantum effects in water and aqueous systems: Experiment, theory, and current challenges," *Chemical reviews*, vol. 116, no. 13, pp. 7529–7550, 2016.

11. G. A. Cisneros, K. T. Wikfeldt, L. Ojamäe, J. Lu, Y. Xu, H. Torabifard, A. P. Bartók, G. Csányi, V. Molinero, and F. Paesani, "Modeling molecular interactions in water: From pairwise to many-body potential energy functions," *Chemical reviews*, vol. 116, no. 13, pp. 7501–7528, 2016.

12. C. Fecko, J. Eaves, J. Loparo, A. Tokmakoff, and P. Geissler, "Ultrafast hydrogen-bond dynamics in the infrared spectroscopy of water," *Science*, vol. 301, no. 5640, pp. 1698–1702, 2003.

13. R. Rey, K. B. Møller, and J. T. Hynes, "Hydrogen bond dynamics in water and ultrafast infrared spectroscopy," *The Journal of Physical Chemistry A*, vol. 106, no. 50, pp. 11993–11996, 2002.

14. R. Kumar, J. Schmidt, and J. Skinner, "Hydrogen bonding definitions and dynamics in liquid water," *The Journal of chemical physics*, vol. 126, no. 20, p. 05B611, 2007.

15. A. G. Lee, "How lipids affect the activities of integral membrane proteins," *Biochimica et Biophysica Acta (BBA)-Biomembranes*, vol. 1666, no. 1-2, pp. 62–87, 2004.

16. L. Piatkowski, J. de Heij, and H. J. Bakker, "Probing the Distribution of Water Molecules Hydrating Lipid Membranes with Ultrafast Forster Vibrational Energy Transfer," *The Journal of Physical Chemistry B*, vol. 117, no. 5, pp. 1367–1377, 2013.

17. M. S. Jhon and J. D. Andrade, "Water and hydrogels," *Journal of biomedical materials research*, vol. 7, no. 6, pp. 509–522, 1973.

18. D. Pasqui, M. De Cagna, and R. Barbucci, "Polysaccharide-based hydrogels: The key role of water in affecting mechanical properties," *Polymers*, vol. 4, no. 3, pp. 1517–1534, 2012.

19. M. Tros, L. Zheng, J. Hunger, M. Bonn, D. Bonn, G. J. Smits, and S. Woutersen, "Picosecond orientational dynamics of water in living cells," *Nature communications*, vol. 8, no. 1, pp. 1–7, 2017.

20. G. Hummer, J. C. Rasaiah, and J. P. Noworyta, "Water conduction through the hydrophobic channel of a carbon nanotube," *Nature*, vol. 414, no. 6860, pp. 188–190, 2001.

21. J. C. Rasaiah, S. Garde, and G. Hummer, "Water in nonpolar confinement: From nanotubes to proteins and beyond," *Annu. Rev. Phys. Chem.*, vol. 59, pp. 713–740, 2008.

22. T. H. van der Loop, N. Ottosson, S. Lotze, E. Kentzinger, T. Vad, W. F. Sager, H. J. Bakker, and S. Woutersen, "Structure and dynamics of water in nanoscopic spheres and tubes," *The Journal of chemical physics*, vol. 141, no. 18, p. 18C535, 2014.

23. K. Tan, N. Nijem, Y. Gao, S. Zuluaga, J. Li, T. Thonhauser, and Y. J. Chabal, "Water interactions in metal organic frameworks," *CrystEngComm*, vol. 17, no. 2, pp. 247–260, 2015.

24. A. J. Rieth, K. M. Hunter, M. Dincă, and F. Paesani, "Hydrogen bonding structure of confined water templated by a metal-organic framework with open metal sites," *Nature communications*, vol. 10, no. 1, pp. 1–7, 2019.

25. X. Liu, X. Wang, and F. Kapteijn, "Water and metal–organic frameworks: From interaction toward utilization," *Chemical Reviews*, 2020.

26. N. E. Levinger, "Water in confinement," *Science*, vol. 298, no. 5599, pp. 1722–1723, 2002.

27. A. M. Dokter, S. Woutersen, and H. J. Bakker, "Inhomogeneous dynamics in confined water nanodroplets," *Proceedings of the National Academy of Sciences*, vol. 103, no. 42, pp. 15355–15358, 2006.

28. E. E. Fenn, D. B. Wong, and M. D. Fayer, "Water dynamics at neutral and ionic interfaces.," *Proceedings of the National Academy of Sciences of the United States of America*, vol. 106, no. 36, pp. 15243–15248, 2009.

29. A. Patra, T. Q. Luong, R. K. Mitra, and M. Havenith, "The influence of charge on the structure and dynamics of water encapsulated in reverse micelles," *Physical Chemistry Chemical Physics*, vol. 16, no. 25, pp. 12875–12883, 2014.

30. J. A. Long, B. M. Rankin, and D. Ben-Amotz, "Micelle Structure and Hydrophobic Hydration," *Journal of the American Chemical Society*, vol. 137, no. 33, pp. 10809–10815, 2015.

31. H. J. Bakker and J. L. Skinner, "Vibrational spectroscopy as a probe of structure and dynamics in liquid water," *Chemical Reviews*, vol. 110, no. 3, pp. 1498–1517, 2010.

32. B. Auer and J. Skinner, "Water: Hydrogen bonding and vibrational spectroscopy, in the bulk liquid and at the liquid/vapor interface," *Chemical physics letters*, vol. 470, no. 1-3, pp. 13–20, 2009.

33. E. B. Wilson, J. C. Decius, and P. C. Cross, *Molecular vibrations: the theory of infrared and Raman vibrational spectra*. Courier Corporation, 1980.

34. J. J. Sakurai, *Modern quantum mechanics; rev. ed.* Reading, MA: Addison-Wesley, 1994.

35. P. Atkins and J. de Paula, *Atkins' Physical Chemistry*. OUP Oxford, 2010.

36. J. McHale, *Molecular Spectroscopy*. CRC Press, 2017.

37. G. Lipari and A. Szabo, "Effect of librational motion on fluorescence depolarization and nuclear magnetic resonance relaxation in macromolecules and membranes.," *Biophysical journal*, vol. 30, no. 3, p. 489, 1980.

38. Y.-S. Lin, P. Pieniazek, M. Yang, and J. Skinner, "On the calculation of rotational anisotropy decay, as measured by ultrafast polarization-resolved vibrational pump-probe experiments," *The Journal of chemical physics*, vol. 132, no. 17, p. 174505, 2010.

39. Y. L. A. Rezus and H. J. Bakker, "On the orientational relaxation of HDO in liquid water," *Journal of Chemical Physics*, vol. 123, no. 11, 2005.

40. Y. L. A. Rezus and H. J. Bakker, "Observation of immobilized water molecules around hydrophobic groups," *Physical Review Letters*, vol. 99, no. 14, pp. 1–4, 2007.

41. R. Boyd and D. Prato, *Nonlinear Optics*. Elsevier Science, 2008.

42. S. Woutersen and H. J. Bakker, "Resonant intermolecular transfer of vibrational energy in liquid water," *Nature*, vol. 402, no. 6761, pp. 507–509, 1999.

43. S. Woutersen, U. Emmerichs, H.-K. Nienhuys, and H. J. Bakker, "Anomalous temperature dependence of vibrational lifetimes in water and ice," *Physical review letters*, vol. 81, no. 5, p. 1106, 1998.

44. M. F. Kropman, H.-K. Nienhuys, S. Woutersen, and H. J. Bakker, "Vibrational relaxation and hydrogen-bond dynamics of hdo: H2o," *The Journal of Physical Chemistry A*, vol. 105, no. 19, pp. 4622–4626, 2001.

45. Y. Rezus and H. Bakker, "Orientational dynamics of isotopically diluted h 2 o and d 2 o," *The Journal of chemical physics*, vol. 125, no. 14, p. 144512, 2006.

46. H.-K. Nienhuys, S. Woutersen, R. A. van Santen, and H. J. Bakker, "Mechanism for vibrational relaxation in water investigated by femtosecond infrared spectroscopy," *The Journal of chemical physics*, vol. 111, no. 4, pp. 1494–1500, 1999.

47. T. Steinel, J. B. Asbury, J. Zheng, and M. Fayer, "Watching hydrogen bonds break: A transient absorption study of water," *The Journal of Physical Chemistry A*, vol. 108, no. 50, pp. 10957–10964, 2004.

48. K. J. Tielrooij, C. Petersen, Y. L. A. Rezus, and H. J. Bakker, "Reorientation of HDO in liquid H2O at different temperatures: Comparison of first and second order correlation functions," *Chemical Physics Letters*, vol. 471, no. 1-3, pp. 71–74, 2009.

49. C. Petersen, K. J. Tielrooij, and H. J. Bakker, "Strong temperature dependence of water reorientation in hydrophobic hydration shells," *Journal of Chemical Physics*, vol. 130, no. 21, 2009.

50. B. K. Paul and S. P. Moulik, "Uses and applications of microemulsions," *Current Science*, vol. 80, no. 8, pp. 990–1001, 2001.

51. R. Saha, S. Rakshit, R. K. Mitra, and S. K. Pal, "Microstructure, morphology, and ultrafast dynamics of a novel edible microemulsion," *Langmuir*, vol. 28, no. 22, pp. 8309–8317, 2012.

52. S. Gupta, S. P. Moulik, B. Hazra, R. Ghosh, S. K. Sanyal, and S. Datta, "New pharmaceutical microemulsion system for encapsulation and delivery of diospyrin, a plant-derived bioactive quinonoid compound.," *Drug delivery*, vol. 13, no. 3, pp. 193–9, 2006.

53. A. Bera and A. Mandal, "Microemulsions: a novel approach to enhanced oil recovery: a review," *Journal of Petroleum Exploration and Production Technology*, vol. 5, no. 3, pp. 255–268, 2015.

54. P. Taylor, "Ostwald ripening in emulsions," *Advances in Colloid and Interface Science*, vol. 75, pp. 107–163, jun 1998.

55. A. M. Cazabat, D. Langevin, and A. Pouchelon, "Light-scattering study of water-oil microemulsions," *Journal of Colloid And Interface Science*, vol. 73, no. 1, pp. 1–12, 1980.

56. S. Bardhan, K. Kundu, G. Chakraborty, S. K. Saha, and B. K. Paul, "The Schulman Method of Cosurfactant Titration of the Oil/Water Interface (Dilution Method): A Review on a Well-Known Powerful Technique in Interfacial Science for Characterization of Water-in-Oil Microemulsions," *Journal of Surfactants and Detergents*, vol. 18, no. 4, pp. 547–567, 2015.

57. D. Langevin, "Micelles and Microemulsions," *Annu. Rev. Phys. Chem.*, vol. 43, no. 1, pp. 341–369, 1992.

58. R. Pons, I. Carrera, J. Caelles, J. Rouch, and P. Panizza, "Formation and properties of miniemulsions formed by microemulsions dilution," *Advances in Colloid and Interface Science*, vol. 106, no. 1-3, pp. 129–146, 2003.

59. D. E. Moilanen, E. E. Fenn, D. Wong, and M. D. Fayer, "Water dynamics in large and small reverse micelles: From two ensembles to collective behavior," *Journal of Chemical Physics*, vol. 131, no. 1, 2009.

60. G. Seifert, T. Patzlaff, and H. Graener, "Size Dependent Ultrafast Cooling of Water Droplets in Microemulsions by Picosecond Infrared Spectroscopy," *Physical Review Letters*, vol. 88, no. 14, p. 147402, 2002.

61. A. A. Jaye, N. T. Hunt, and S. R. Meech, "Ultrafast dynamics in the dispersed phase of oil-in-water microemulsions: Monosubstituted benzenes incorporated into Dodecyltrimethylammonium Bromide (DTAB) aqueous micelles," *Langmuir*, vol. 21, no. 4, pp. 1238–1243, 2005.

62. S. Lotze, C. C. M. Groot, C. Vennehaug, and H. J. Bakker, "Femtosecond mid-infrared study of the dynamics of water molecules in water-acetone and water-dimethyl sulfoxide mixtures," *Journal of Physical Chemistry B*, vol. 119, no. 16, pp. 5228–5239, 2015.

63. S. T. Van Der Post, S. Scheidelaar, and H. J. Bakker, "Water dynamics in aqueous solutions of tetra-n-alkylammonium salts: Hydrophobic and coulomb interactions disentangled," *Journal of Physical Chemistry B*, vol. 117, no. 48, pp. 15101–15110, 2013.

64. Y. L. A. Rezus and H. J. Bakker, "Femtosecond spectroscopic study of the solvation of amphiphilic molecules by water," *Chemical Physics*, vol. 350, no. 1-3, pp. 87–93, 2008.

65. K. J. Tielrooij, J. Hunger, R. Buchner, M. Bonn, and H. J. Bakker, "Influence of concentration and temperature on the dynamics of water in the hydrophobic hydration shell of tetramethylurea," *Journal of the American Chemical Society*, vol. 132, no. 44, pp. 15671–15678, 2010.

66. C. Petersen, A. A. Bakulin, V. G. Pavelyev, M. S. Pshenichnikov, and H. J. Bakker, "Femtosecond midinfrared study of aggregation behavior in aqueous solutions of amphiphilic molecules," *Journal of Chemical Physics*, vol. 133, no. 16, pp. 1–8, 2010.

67. M. Amann, L. Willner, J. Stellbrink, A. Radulescu, and D. Richter, "Studying the concentration dependence of the aggregation number of a micellar model system by SANS," *Soft Matter*, vol. 11, no. 21, pp. 4208–4217, 2015.

68. B. L. Bales and R. Zana, "Characterization of micelles of quaternary ammonium surfactants as reaction media I: Dodeclytrimethylammonium bromide and chloride," *Journal of Physical Chemistry B*, vol. 106, no. 8, pp. 1926–1939, 2002.

69. M. Pisárčik, F. Devínsky, and M. Pupák, "Determination of micelle aggregation numbers of alkyltrimethylammonium bromide and sodium dodecyl sulfate surfactants using time-resolved fluorescence quenching," *Open Chemistry*, vol. 13, no. 1, pp. 922–931, 2015.

70. K. M. Lusvardi, A. P. Full, and E. W. Kaler, "Mixed Micelles of Dodecyltrimethylammonium Bromide and Didodecyldimethylammonium Bromide," *Langmuir*, vol. 11, no. 2, pp. 487–492, 1995.

71. F. H. Quina, P. M. Nassar, J. B. Bonilha, and B. L. Bales, "Growth of sodium dodecyl sulfate micelles with detergent concentration," *Journal of Physical Chemistry*, vol. 99, no. 46, pp. 17028–17031, 1995.

72. R. Ranganathan, M. Peric, R. Medina, U. Garcia, B. L. Bales, and M. Almgren, "Size, hydration, and shape of SDS/heptane micelles investigated by

time-resolved fluorescence quenching and electron spin resonance," *Langmuir*, vol. 17, no. 22, pp. 6765–6770, 2001.

73. A. Gupta, H. B. Eral, T. A. Hatton, and P. S. Doyle, "Nanoemulsions: Formation, properties and applications," *Soft Matter*, vol. 12, no. 11, pp. 2826–2841, 2016.

74. M. M. Fryd and T. G. Mason, "Advanced Nanoemulsions," *Annual Review of Physical Chemistry*, vol. 63, no. 1, pp. 493–518, 2012.

75. T. G. Mason, S. M. Graves, J. N. Wilking, and M. Y. Lin, "Extreme emulsification: Formation and structure of nanoemulsions," *Condensed Matter Physics*, vol. 9, no. 1, pp. 193–199, 2006.

76. D. J. McClements, "Nanoemulsions versus microemulsions: terminology, differences, and similarities," *Soft Matter*, vol. 8, no. 6, p. 1719, 2012.

77. K. Meleson, S. Graves, and T. G. Mason, "Formation of concentrated nanoemulsions by extreme shear," *Soft Materials*, vol. 2, no. 2-3, pp. 109–123, 2004.

78. T. Delmas, H. Piraux, A. C. Couffin, I. Texier, F. Vinet, P. Poulin, M. E. Cates, and J. Bibette, "How to prepare and stabilize very small nanoemulsions," *Langmuir*, vol. 27, no. 5, pp. 1683–1692, 2011.

79. S. Uluata, E. A. Decker, and D. J. McClements, "Optimization of Nanoemulsion Fabrication Using Microfluidization: Role of Surfactant Concentration on Formation and Stability," *Food Biophysics*, vol. 11, no. 1, pp. 52–59, 2016.

80. H. B. De Aguiar, *Vibrational Sum-Frequency Scattering Studies of Oil-in-Water Emulsions*. PhD thesis, École Polytechnique Fédérale de Lausanne, 2011.

81. H. B. De Aguiar, A. G. F. De Beer, M. L. Strader, and S. Roke, "The interfacial tension of nanoscopic oil droplets in water is hardly affected by SDS surfactant," *Journal of the American Chemical Society*, vol. 132, no. 7, pp. 2122–2123, 2010.

82. J. K. Hensel, A. P. Carpenter, R. K. Ciszewski, B. K. Schabes, C. T. Kittredge, F. G. Moore, and G. L. Richmond, "Molecular characterization of water and surfactant AOT at nanoemulsion surfaces," *Proceedings of the National Academy of Sciences*, vol. 114, pp. 13351–13356, dec 2017.

83. A. P. Carpenter, E. Tran, R. M. Altman, and G. L. Richmond, "Formation and surface-stabilizing contributions to bare nanoemulsions created with negligible surface charge," *Proceedings of the National Academy of Sciences of the United States of America*, vol. 116, no. 19, pp. 9214–9219, 2019.

84. Y. Sang, F. Yang, S. Chen, H. Xu, S. Zhang, Q. Yuan, and W. Gan, "Molecular interactions at the hexadecane/water interface in the presence of surfactants studied with second harmonic generation," *Journal of Chemical Physics*, vol. 142, no. 22, 2015.

85. C. C. M. Groot, *Dynamics of water interacting with biomolecules*. PhD thesis, Universiteit van Amsterdam, 2017.

86. E. van Dam and H. Bakker, "Structure of micelles and micro-emulsions probed through the molecular reorientation of water," *Chemical Physics*, vol. 512, 2018.

87. G. Kogan, L. Šoltés, R. Stern, and P. Gemeiner, "Hyaluronic acid: A natural biopolymer with a broad range of biomedical and industrial applications," *Biotechnology Letters*, vol. 29, no. 1, pp. 17–25, 2007.

88. K. T. Dicker, L. A. Gurski, S. Pradhan-Bhatt, R. L. Witt, M. C. Farach-Carson, and X. Jia, "Hyaluronan: A simple polysaccharide with diverse biological functions," *Acta Biomaterialia*, vol. 10, no. 4, pp. 1558–1570, 2014.

89. A. Singh, M. Corvelli, S. A. Unterman, K. A. Wepasnick, P. McDonnell, and J. H. Elisseeff, "Enhanced lubrication on tissue and biomaterial surfaces through peptide-mediated binding of hyaluronic acid," *Nature Materials*, vol. 13, no. 10, pp. 988–995, 2014.

90. A. G. OGSTON and J. E. STANIER, "The physiological function of hyaluronic acid in synovial fluid; viscous, elastic and lubricant properties.," *The Journal of physiology*, vol. 119, pp. 244–52, feb 1953.

91. D. A. Swann, E. L. Radin, M. Nazimiec, P. A. Weisser, N. Curran, and G. Lewinnek, "Role of hyaluronic acid in joint lubrication," *Annals of the Rheumatic Diseases*, vol. 33, no. 4, pp. 318–326, 1974.

92. X. Tian, J. Azpurua, C. Hine, A. Vaidya, M. Myakishev-Rempel, J. Ablaeva, Z. Mao, E. Nevo, V. Gorbunova, and A. Seluanov, "High-molecular-mass hyaluronan mediates the cancer resistance of the naked mole rat," *Nature*, vol. 499, no. 7458, pp. 346–349, 2013.

93. B. P. Toole, "Hyaluronan: From extracellular glue to pericellular cue," *Nature Reviews Cancer*, vol. 4, no. 7, pp. 528–539, 2004.

94. B. P. Toole, "Hyaluronan in morphogenesis," *Seminars in Cell and Developmental Biology*, vol. 12, no. 2, pp. 79–87, 2001.

95. M. F. Chaplin, "Fibre and water binding," *Proceedings of the Nutrition Society*, vol. 62, no. 01, pp. 223–227, 2003.

96. R. Gyawali and S. A. Ibrahim, "Effects of hydrocolloids and processing conditions on acid whey production with reference to Greek yogurt," *Trends in Food Science and Technology*, vol. 56, pp. 61–76, 2016.

97. E. A. Balazs and J. Cui, "The story of hyaluronan putty," *Bioactive Carbohydrates and Dietary Fibre*, vol. 2, no. 2, pp. 143–151, 2013.

98. I. Gatej, M. Popa, and M. Rinaudo, "Role of the pH on hyaluronan behavior in aqueous solution," *Biomacromolecules*, vol. 6, no. 1, pp. 61–67, 2005.

99. S. Wu, L. Ai, J. Chen, J. Kang, and S. W. Cui, "Study of the mechanism of formation of hyaluronan putty at pH 2.5: Part I. Experimental measurements," *Carbohydrate Polymers*, vol. 98, pp. 1677–1682, nov 2013.

100. A. B. Kayitmazer, A. F. Koksal, and E. Kilic Iyilik, "Complex coacervation of hyaluronic acid and chitosan: effects of pH, ionic strength, charge density, chain length and the charge ratio," *Soft Matter*, vol. 11, no. 44, pp. 8605–8612, 2015.

101. D. A. Gibbs, E. W. Merrill, K. A. Smith, and E. A. Balazs, "Rheology of hyaluronic acid," *Biopolymers*, vol. 6, no. 6, pp. 777–791, 1968.

102. G. Giubertoni, F. Burla, C. Martinez-Torres, B. Dutta, G. Pletikapic, E. Pelan, Y. L. Rezus, G. H. Koenderink, and H. J. Bakker, "Molecular Origin of the Elastic State of Aqueous Hyaluronic Acid," *Journal of Physical Chemistry B*, vol. 123, no. 14, pp. 3043–3049, 2019.

103. A. J. Kim, V. N. Manoharan, and J. C. Crocker, "Swelling-based method for preparing stable, functionalized polymer colloids," *Journal of the American Chemical Society*, vol. 127, no. 6, pp. 1592–1593, 2005.

104. R. Cerbino and V. Trappe, "Differential dynamic microscopy: Probing wave vector dependent dynamics with a microscope," *Physical Review Letters*, vol. 100, no. 18, pp. 1–4, 2008.

105. E. A. Balazs, "Sediment volume and viscoelastic behavior of hyaluronic acid solutions," *Fed Proc*, vol. 25, no. 6, pp. 1817–1822, 1966.

106. O. Schmut and H. Hofmann, "Preparation of gels from hyaluronate solutions," *Graefe's Archive for Clinical and Experimental Ophthalmology*, vol. 218, pp. 311–314, jun 1982.

107. M. A. Escobedo-Sánchez, J. P. Segovia-Gutiérrez, A. B. Zuccolotto-Bernez, J. Hansen, C. C. Marciniak, K. Sachowsky, F. Platten, and S. U. Egelhaaf, "Microliter viscometry using a bright-field microscope:: η -DDM," *Soft Matter*, vol. 14, no. 34, pp. 7016–7025, 2018.

108. P. Edera, D. Bergamini, V. Trappe, F. Giavazzi, and R. Cerbino, "Differential dynamic microscopy microrheology of soft materials: A tracking-free determination of the frequency-dependent loss and storage moduli," *Physical Review Materials*, vol. 1, p. 073804, dec 2017.

109. A. V. Bayles, T. M. Squires, and M. E. Helgeson, "Probe microrheology without particle tracking by differential dynamic microscopy," *Rheologica Acta*, vol. 56, no. 11, pp. 863–869, 2017.

110. B. Chakrabarti and E. A. Balazs, "Optical properties of hyaluronic acid. Ultraviolet circular dichroism and optical rotatory dispersion," *Journal of Molecular Biology*, vol. 78, no. 1, pp. 135–141, 1973.

111. J. K. Sheehan, K. H. Gardner, and E. D. T. Atkins, "Hyaluronic acid: a double-helical structure in the presence of potassium at low pH and found also with the cations ammonium, rubidium and caesium," *Journal of Molecular Biology*, vol. 117, no. 1, pp. 113–135, 1977.

112. C. Blundell, P. Deangelis, and A. Almond, "Hyaluronan: the absence of amide–carboxylate hydrogen bonds and the chain conformation in aqueous solution are incompatible with stable secondary and tertiary structure models," *Biochemical Journal*, vol. 396, no. 3, pp. 487–498, 2006.

113. P. GRIBBON, B. C. HENG, and T. E. HARDINGHAM, "The analysis of intermolecular interactions in concentrated hyaluronan solutions suggest no evidence for chain–chain association," *Biochemical Journal*, vol. 350, no. 1, p. 329, 2000.

114. G. Lalevée, L. David, A. Montembault, K. Blanchard, J. Meadows, S. Malaise, A. Crépet, I. Grillo, I. Morfin, T. Delair, and G. Sudre, "Highly stretchable hydrogels from complex coacervation of natural polyelectrolytes," *Soft Matter*, pp. 6594–6605, 2017.

115. J. Hunger, A. Bernecker, H. J. Bakker, M. Bonn, and R. P. Richter, "Hydration dynamics of hyaluronan and dextran," *Biophysical Journal*, vol. 103, no. 1, pp. L10–L12, 2012.

116. C. C. M. Groot and H. J. Bakker, "A femtosecond mid-infrared study of the dynamics of water in aqueous sugar solutions," *Phys. Chem. Chem. Phys.*, vol. 17, no. 0, pp. 8449–8458, 2015.

117. M. I. Giannotti and G. J. Vancso, "Interrogation of single synthetic polymer chains and polysaccharides by AFM-based force spectroscopy," *ChemPhysChem*, vol. 8, no. 16, pp. 2290–2307, 2007.

118. A. M. Van Buul, E. Schwartz, P. Brocorens, M. Koepf, D. Beljonne, J. C. Maan, P. C. Christianen, P. H. Kouwer, R. J. Nolte, H. Engelkamp, K. Blank, and A. E. Rowan, "Stiffness versus architecture of single helical polyisocyanopeptides," *Chemical Science*, vol. 4, no. 6, pp. 2357–2363, 2013.

119. D. E. Discher, P. Janmey, and Y. L. Wang, "Tissue cells feel and respond to the stiffness of their substrate," *Science*, vol. 310, no. 5751, pp. 1139–1143, 2005.

120. A. J. Engler, S. Sen, H. L. Sweeney, and D. E. Discher, "Matrix Elasticity Directs Stem Cell Lineage Specification," *Cell*, vol. 126, no. 4, pp. 677–689, 2006.

121. R. K. Das, V. Gocheva, R. Hammink, O. F. Zouani, and A. E. Rowan, "Stress-stiffening-mediated stem-cell commitment switch in soft responsive hydrogels," *Nature Materials*, vol. 15, no. 3, pp. 318–325, 2016.

122. C. Zhang, D. A. Mcadams, and J. C. Grunlan, "Nano/Micro-Manufacturing of Bioinspired Materials: a Review of Methods to Mimic Natural Structures," *Advanced materials (Deerfield Beach, Fla.)*, vol. 28, no. 30, pp. 6292–6321, 2016.

123. Q. Li, D. G. Barrett, P. B. Messersmith, and N. Holten-Andersen, "Controlling hydrogel mechanics via bio-inspired polymer-nanoparticle bond dynamics," *ACS Nano*, vol. 10, no. 1, pp. 1317–1324, 2016.

124. P. H. J. Kouwer, M. Koepf, V. a. a. Le Sage, M. Jaspers, A. M. van Buul, Z. H. Eksteen-Akeroyd, T. Woltinge, E. Schwartz, H. J. Kitto, R. Hoogenboom, S. J. Picken, R. J. M. Nolte, E. Mendes, and A. E. Rowan, "Responsive biomimetic networks from polyisocyanopeptide hydrogels.," *Nature*, vol. 493, no. 7434, pp. 651–655, 2013.

125. F. Millich and G. K. Baker, "Polyisonitriles. III. Synthesis and Racemization of Optically Active Poly (α-phenylethylisonitrile)," *Macromolecules*, vol. 2, no. 2, pp. 122–128, 1969.

126. J. J. Cornelissen, J. J. Donners, R. De Gelder, W. S. Graswinckel, G. A. Metselaar, A. E. Rowan, N. A. Sommerdijk, and R. J. Nolte, "β-Helical polymers from isocyanopeptides," *Science*, vol. 293, no. 5530, pp. 676–680, 2001.

127. M. Jaspers, M. Dennison, M. F. Mabesoone, F. C. MacKintosh, A. E. Rowan, and P. H. Kouwer, "Ultra-responsive soft matter from strain-stiffening hydrogels," *Nature Communications*, vol. 5, 2014.

128. M. Jaspers, A. C. Pape, I. K. Voets, A. E. Rowan, G. Portale, and P. H. Kouwer, "Bundle Formation in Biomimetic Hydrogels," *Biomacromolecules*, vol. 17, no. 8, pp. 2642–2649, 2016.

129. G. A. Metselaar, P. J. H. M. Adams, R. J. M. Nolte, J. J. L. M. Cornelissen, and A. E. Rowan, "Polyisocyanides derived from tripeptides of alanine," *Chemistry - A European Journal*, vol. 13, no. 3, pp. 950–960, 2007.

130. B. Ensing, A. Tiwari, M. Tros, J. Hunger, S. R. Domingos, C. Pérez, G. Smits, M. Bonn, D. Bonn, and S. Woutersen, "On the origin of the extremely different solubilities of polyethers in water," *Nature Communications*, vol. 10, no. 1, pp. 1–8, 2019.

131. J. Qvist and B. Halle, "Thermal signature of hydrophobic hydration dynamics," *Journal of the American Chemical Society*, vol. 130, no. 31, pp. 10345–10353, 2008.

Summary

Water is essential to all life on earth. Even though water is ubiquitous, understanding and predicting the behaviour of water on a molecular level remains a great challenge. The main reason for the complexity of water lies in the fact that water molecules are able to form a three-dimensional network, facilitated by their ability to form hydrogen bonds. A hydrogen bond is a relatively strong intermolecular connection between the lone pair of an electronegative atom, e.g. oxygen, and a hydrogen atom. In liquid water, hydrogen bonds are constantly broken and formed and water molecules are rotating on a picosecond timescale. In this study we investigate the properties of water experimentally using polarization-resolved pump-probe infrared spectroscopy: a technique that can be used to measure the dynamics of water with ultrashort laser pulses. In particular, we use this technique to investigate the water reorientation dynamics in nanostructured aqueous systems.

Towards pump-probe measurements at high repetition rate
Currently, most infrared pump-probe measurements are performed at a repetition rate of 1 kHz. To improve the signal-to-noise ratio in these experiments, we have developed a pump-probe setup that can operate at higher repetition rates, up to 16.7 kHz. Using this high repetition rate, we are able to perform more measurements in a shorter time, and since the signal-to-noise ratio scales with the square root of the number of measurements, the quality of the obtained data significantly improves. We demonstrate the practical implementation, optimization and proof of principle of high repetition rate measurements. We also observe that the use of a higher repetition rate leads to a stronger heating of the sample during the measurements. This sample heating can be compensated effectively by cooling.

Structure of micelles and micro-emulsions
One of the types of nanostructured aqueous materials that we study are emulsions. We start by studying the structural properties of dodecyltrimethylammonium bromide (DTAB) micelles and micro-emulsions. In these systems, water is surrounding DTAB micelles and oil droplets coated with DTAB surfactant molecules. Using polarization-resolved pump-probe spectroscopy, we observe that a fraction of the water molecules is reorienting on a much slower timescale than bulk water. These slow water molecules are interacting with the micelles and micro-emulsion droplets. For micelles, we observe a sublinear increase of slow water with increasing DTAB concentration, which indicates an increase in micelle size and enhanced aggregation. For micro-emulsions, we measure the slow water fraction as function of increasing oil concentration. We observe that

the fraction of slow water does not change as a function of oil content. This result shows that in micro-emulsions, the added oil molecules are absorbed in the core of the droplets and completely shielded from the surrounding water.

Water reorientation dynamics in nano-emulsions

The second type of emulsions that we study are nano-emulsions. Nano-emulsion droplets are in fact bigger than micro-emulsion droplets, contrary to what their name suggests. Nano-emulsions differ from micro-emulsions in size, surfactant content and stability. Nano-emulsion oil-in-water droplets are not thermodynamically stable like micro-emulsion droplets, but yet are kinetically stable, allowing us to study them at different compositions with femtosecond pump-probe spectroscopy. Similar as for the micro-emulsions, we observe for nano-emulsions a fraction of water molecules to be reorienting on much longer timescales than for bulk water. In contrast to the micro-emulsions, the fraction of slow water is now dependent on the oil content. The indicates that in nano-emulsions, the water molecules are interacting with the oil molecules. Interestingly, the fraction of slowly reorienting water is not dependent on the size of the droplets. This independence of the slow water fraction on the droplet size implies that the total surface area of the droplets is quite independent of the droplet size, which indicates that the surfaces of the oil droplets are quite strongly corrugated, with an increasing degree of corrugation with droplet size.

Hyaluronan biopolymers release water upon gelation

Next to our studies on emulsions, we investigated the dynamics of water molecules in hyaluronan hydrogels. Hyaluronan is a biopolymer found in many biological tissues and fluids, where it is involved in a wide range of biological functions. Aqueous solutions of high molecular weight hyaluronan are responsive to their environment, they form a gel at a narrow pH range around pH 2.4. By studying these solutions using polarization-resolved pump-probe infrared spectroscopy, we find that hyaluronan slows down a fraction of the water molecules. At pH 2.4, this fraction reaches a minimum while the viscosity reaches a maximum. This implies that water molecules become on average more mobile when the solution becomes more viscous. This counterintuitive result can be explained from the gelation mechanism of the polymer. The hyaluronan polymer chains bundle to form a network, leading to an increased viscosity. The bundle formation involves the expulsion of hydration water from the surfaces of the hyaluronan polymers, leading to more bulk water molecules with a higher mobility.

Structure and dynamics of a temperature sensitive hydrogel

We investigated another responsive hydrogel, based on polyisocyanotripeptides (TriPIC). This is a biomimetic polymer with a β-helical backbone stabilized by hydrogen bonds between amide groups. When the polyisocyanidepeptides are grafted with ethylene glycol side chains, they exhibit a thermoresponsive behavior that causes the polymer to form a gel at temperatures above 50°C. We studied the gelation process using FTIR spectroscopy and pump-probe spectroscopy. From isotope exchange experiments, we observe that the helical backbone and

the amide groups closest to the backbone form a hydrophobic core that is inaccessible to water, which stays inaccessible even at temperatures above gelation temperature. Contrary to the hyaluronan hydrogels, for TriPIC we observe an increase in the fraction of slow water molecules upon gelation. We explain this increase from the enhanced binding of water molecules to the polyethylene glycol side chains. We propose that this binding, in particular the donation of two strong hydrogen bonds by a water molecule to two negatively charged oxygen atoms of polyethylene glycol side chains that belong to different polymers, may play a role in the bundling of the polymers. The water molecules thus may act as a glue that bind the polymers together, leading to an extended polymer network, and eventually to the formation of a hydrogel.

Samenvatting

Water is essentieel voor al het leven op aarde. Ondanks dat water alomtegenwoordig is, is het begrijpen en voorspellen van het gedrag van water op moleculair niveau een grote uitdaging. De voornaamste reden voor de complexiteit van water is dat watermoleculen in staat zijn om een driedimensionaal netwerk te vormen, doordat elk watermolecuul maar liefst vier waterstofbruggen met andere watermoleculen kan vormen. Een waterstofbrug is een relatief sterke intermoleculaire verbinding tussen een vrij elektronenpaar van een elektronegatief atoom, bijvoorbeeld zuurstof, en een waterstofatoom. In vloeibaar water worden waterstofbruggen constant verbroken en gevormd, en watermoleculen roteren op een tijdschaal van picoseconden. In deze studie onderzoeken we experimenteel de eigenschappen van water met behulp van polarisatie-opgeloste pomp-probe infraroodspectroscopie: een techniek die in staat is de dynamica van water te meten door middel van ultrasnelle laser pulsen. We gebruiken deze techniek om de water reoriëntatie dynamica te onderzoeken in nanogestructureerde waterige systemen.

Metingen met hoge herhalingssnelheid

Momenteel worden meeste infrarood pomp-probe metingen uitgevoerd met een herhalingsfrequentie van 1 kHz. Om de signaal-ruis verhouding te verbeteren, hebben we een pomp-probe opstelling ontwikkeld die functioneert met hogere herhalingssnelheden, tot 16.7 kHz. Met deze verbetering zijn we in staat om meer metingen te doen in kortere tijd, en aangezien de signaal-ruis verhouding schaalt met de wortel van het aantal metingen, verbetert de kwaliteit van de data aanzienlijk. We demonstreren de praktische uitvoering, optimalisatie en bewijs van het principe van hoge herhalingssnelheid metingen. We zien echter ook dat het gebruik van een hogere herhalingssnelheid leidt tot een sterkere opwarming van het sample tijdens de meting. Deze sample opwarming kan effectief worden gecompenseerd door het sample te koelen.

Structuur van micellen en micro-emulsies

Emulsies zijn nanogestructureerde waterige systemen die worden gevormd door oliedruppels in water of waterdruppels in olie. We bestuderen de structurele eigenschappen van dodecyltrimethylammonium bromide (DTAB) micellen en micro-emulsies. In deze systemen zijn de DTAB micellen en oliedruppels gecoat met DTAB surfactant moleculen, omringd door water. Door middel van polarisatie-opgeloste pomp-probe spectroscopie observeren we dat een fractie van de watermoleculen op een veel langere tijdschaal reoriënteert dan de moleculen in bulk water. Deze langzame watermoleculen interacteren met de micellen en de micro-emulsie druppels. Voor micellen observeren we een sublin-

eaire toename van het aantal langzame watermoleculen met toenemende DTAB concentratie. Dit geeft aan dat met toenemende DTAB concentratie de gemiddelde micelgrootte toeneemt en de micellen aggregeren. Door olie toe te voegen aan de micellen creëren we micro-emulsies. Voor deze emulsies meten we de fractie langzaam water als functie van de olie concentratie. We zien dat de fractie langzaam water niet verandert als functie van het oliegehalte. Dit resultaat laat zien dat de toegevoegde oliemoleculen in de kern van de druppels worden opgenomen en daardoor compleet afgeschermd zijn van het omringende water.

WATER REORIËNTATIE DYNAMICA IN NANO-EMULSIES

Het tweede type emulsies dat we onderzoeken zijn nano-emulsies. In tegenstelling tot wat de naam nano-emulsie suggereert zijn de druppels groter dan die van micro-emulsies. Nano-emulsies verschillen van micro-emulsies in druppelgrootte, surfactant gehalte en stabiliteit. Nano-emulsie olie-in-water druppels zijn niet thermodynamisch stabiel zoals micro-emulsie druppels, maar ze zijn wel kinetisch stabiel. Hierdoor kunnen we ze toch bestuderen met femtosecconde pomp-probe spectroscopie. Net als met de micro-emulsies, zien we dat een fractie van de watermoleculen reoriënteert op een veel langere tijdschaal dan de moleculen in bulk water. In tegenstelling tot de micro-emulsies, hangt de hoeveelheid langzaam roterend water voor nano-emulsies wel af van het oliegehalte. Dit wijst erop dat in nano-emulsies de watermoleculen interacteren met de oliemoleculen. Interessant is dat de fractie langzaam reoriënterend water niet afhankelijk is van de druppelgrootte wat impliceert dat de totale oppervlakte van de druppels onafhankelijk is van de druppelgrootte. Dit betekent dat de oppervlaktes van de oliedruppels sterk gerimpeld zijn, en dat de rimpeling toeneemt met de druppelgrootte.

HYALURONAN BIOPOLYMEREN LATEN WATER LOS TIJDENS GELERING

We hebben ook onderzoek gedaan naar de dynamica van watermoleculen in hyaluronan hydrogels. Hyaluronan is een biopolymeer dat prominent aanwezig is in biologische weefsels en vloeistoffen, en een belangrijke rol speelt in een verscheidenheid aan biologische functies. Waterige oplossingen van hyaluronanpolymeren met hoog molecuulgewicht hebben als bijzondere eigenschap dat ze een gel vormen in een nauw pH bereik rond pH 2.4. We nemen waar dat hyaluronan een fractie van de watermoleculen vertraagd. Bij pH 2.4 bereikt deze fractie echter een minimum, terwijl de viscositeit juist een maximum bereikt, wat betekent dat watermoleculen gemiddeld meer mobiel worden terwijl de oplossing meer stroperig en zelfs elastisch wordt. Dit contra-intuïtieve resultaat kan worden verklaard vanuit het geleringsmechanisme van het polymeer. De hyaluronan polymeerketens vormen bij pH 2.4 een sterk verbonden netwerk, wat leidt tot een verhoogde viscositeit en elasticiteit. Het vormen van verbindingen tussen de polymeren betekent dat het hydratatiewater van het oppervlak van de hyaluronan polymeren loskomt, wat leidt tot meer bulk watermoleculen met een hogere mobiliteit.

STRUCTUUR EN DYNAMICA VAN EEN TEMPERATUUR GEVOELIGE HYDROGEL

Naast hyaluronan, hebben we onderzoek gedaan aan polyisocyanotripeptides

(TriPIC) hydrogels. TriPIC is een biomimetische polymeer met een β-helisch skelet. Als de polyisocyanidepeptides worden voorzien van ethyleenglycol zijketens, hebben ze een thermoresponsief gedrag wat er voor zorgt dat het polymeer een gel vormt bij temperaturen boven 50°C. We hebben het geleringsproces bestudeerd met FTIR-spectroscopie en pomp-probe spectroscopie. Met isotoop uitwisselingsexperimenten vinden we dat het helische skelet dat de hydrofobe kern vormt, ontoegankelijk is voor water, zelfs bij temperaturen boven de geleringstemperatuur. In contrast met hyaluronan hydrogels, vinden we voor TriPIC een toename in fractie langzame watermoleculen bij gelering. We verklaren deze toenamen door de versterkte binding van watermoleculen aan de polyethyleenglycol zijketens. Wij stellen voor dat deze binding een rol speelt in het bundelen van de polymeren. Het gaat hier in het bijzonder om de donatie van twee sterke waterstofbruggen van een watermolecuul aan twee negatief geladen zuurstofatomen van polyethyleenglycol zijketens die tot verschillende polymeren behoren. De watermoleculen plakken als een soort lijm daarmee de polymeren aan elkaar, wat leidt tot de vorming van een uitgebreid polymeer netwerk, en uiteindelijk een hydrogel.

Acknowledgements

I would like to use this final chapter to express my gratitude to everyone who has been part of the 4 years and 8 months of my PhD. Thank you for all your help and support during this time. Ten eerste wil ik uiteraard mijn promotor Huib Bakker bedanken. Dankjewel voor de goede begeleiding afgelopen jaren. Tijdens onze werkbesprekingen liep ik meestal sceptisch over de data naar binnen, en na het bespreken liep ik altijd met een goed gevoel erover naar buiten. Dankjewel dat je ook midden in de nacht, in het weekend en zelfs op vakantie bereid was mijn proefschrift te corrigeren. Naast de begeleiding van mijn promotietraject, heb ik ook veel steun ervaren tijdens het vormgeven van de vervolgstap in mijn carrière. Jouw aanmoediging voor het doen van een PostDoc waardeer ik enorm.

My time at AMOLF is characterized by a fantastic time with my colleagues. On my first day, I was welcomed in the office by my first officemates Carien and Konrad. Carien, thank you for teaching me everything about Lucifer and being patient while I took my first steps in nonlinear spectroscopy. Konrad, we had such a good time designing and performing science workshops for kids. The trip to Brussels for giving a workshop on animals surviving ice-cold temperatures was a real highlight. After Carien left, my new officemate was Carolyn. Carolyn, thank you for always being there for me, through good and bad times. We always made jokes about dedicating at least 3 pages to you in the acknowledgements of our theses because you are such a good friend for everyone around you. Together we decided that Roberto should be our new officemate after Konrad left. We did not regret this decision for one second. Roberto, after a probation time – the amazing Gordon conference in the US, followed by a trip to New York – you were officially accepted in our office. Thank you for always being the happy positive person that you are. I am very happy that both of you became such good friends and I am excited to have you by my side in the special role of my paranymphs during my defense.

Giulia, thank you for giving me a nickname which I have to explain to everyone. It was so delightful to work with you! Our love for hyaluronan putty brought us together and this will probably follow us the rest of our life. Aleksandr and Alexander, thanks for the great parties! Although they were sometimes a bit hard to digest, I hope we can have such a nice event in the future again. Harmen, we have worked so much together on building the new Lucy setup together. Honestly, I could not have done it without you. You have helped me so much in becoming confident in building the setup from scratch, and I know I will keep using those skills in the future. It was really a joy to work together on that project. I would like to thank all the older and

newer group members of the ultrafast spectroscopy group: Aditi, Alexandra, Andrea, Balazs, Bart, Biplab, Johannes, Liyuan, Marloes, Oleg, Rahul, Simona, Stephan, Wilbert and Yves. I would also like to think all the other friends that I made at AMOLF, during the many activities that the PV organized.

Naast mijn groepsgenoten wil ik ook de technische ondersteuning op AMOLF bedanken, in het bijzonder Hinco, Jan en Ivo. Hinco, zonder jouw ondersteuning zou het lab ongetwijfeld een niet werkende puinhoop zijn. Naast deze technische skills kon je ook altijd iedereen geruststellen, en dat is denk ik net zo'n belangrijke vaardigheid. Jan, dankjewel voor je hulp en kritische houding tijdens het bouwen van de nieuwe Lucy opstelling. Ivo, ik heb een hoop van jou geleerd over de meetopstelling in z'n geheel. Naast het programmeren van de nieuwe software, hebben we ook samen gewerkt aan het beter begrijpen van de hardware en timing van Lucy. Dankjewel voor de prettige samenwerking!

In these past years I was very lucky to have nice collaborations, both within and outside AMOLF. I would like to thank Roland Gouzy, Krassimir Velikov and Eddie Pelan from Unilever for a very nice collaboration on the nano-emulsion project. Roland, thanks for always delivering the perfect nano-emulsion samples, either by mail, at conferences or at the other side of the road at the UvA. Federica and Gijsje, thank you for working together on the hyaluronan project and for being able to measure even the tiniest viscosity changes. Hongbo Yuan and Paul Kouwer from Radboud Universiteit, I am very happy that you came to our lab with this wonderful thermoresponsive polymer. This was such an intriguing material to work with.

Tot slot wil ik mijn vrienden en familie bedanken. Coco, de drie ingenieurs, de Vathorst groep, alle vrienden die ik via Shawano's Oegstgeest heb leren kennen, Bas en Nikki, bedankt voor jullie vriendschap. Mijn ouders Arie en Annemarie, schoonouders Nel en Fer, Alexander en Richard, bedankt voor jullie onverminderde aanmoediging en ondersteuning. Thomas, dankjewel dat je er altijd voor mij bent. Ik ben enorm dankbaar dat ik een partner heb waarmee ik op elk niveau alles kan bespreken. Zonder jou had ik het niet gekund.